

1

UNIVERSITY OF BRISTOL

2

DOCTORAL THESIS

3

4

Investigating, implementing, and creating methods for analysing large neuronal ensembles

5

6

Author:

Thomas J. DELANEY

Supervisors:

Dr. Cian O'DONNELL

Dr. Michael C. ASHBY

7

9 *A thesis submitted in fulfillment of the requirements*

10 *for the degree of Doctor of Philosophy*

11 *in the*

12 Biological Intelligence & Machine Learning Unit

13 Department of Computer Science

14 August 13, 2020

15 Word count: 39000

¹⁶ **Declaration of Authorship**

¹⁷ I declare that the work in this dissertation was carried out in accordance with the requirements of the University's Regulations and Code of Practice for Research Degree Programmes
¹⁸ and that it has not been submitted for any other academic award. Except where indicated by
¹⁹ specific reference in the text, the work is the candidate's own work. Work done in collabora-
²⁰ tion with, or with the assistance of, others, is indicated as such. Any views expressed in the
²¹ dissertation are those of the author.

²² Signed:

²³ _____

²⁴ Date:

²⁵ _____

Acknowledgements

28 I would like to thank my supervisors, Cian O'Donnell and Mike Ashby, for their help, en-
29 couragement, advice, and patience over the last four years. This includes not only helping
30 with research, but also enabling and encouraging me to make the most of my opportunities
31 during that time. Without their help, I would not have grown as much as I have done in those
32 years. I very grateful for their time and effort.

33 I would also like to thank the members of the Bristol Computational Neuroscience Unit
34 for introducing me to all the various aspects of computer science, neuroscience, and machine
35 learning, of which I otherwise would not have heard. As the first person to introduce me to
36 the concept of mathematical neuroscience during my undergraduate days, and a great source
37 of advice and guidance during my PhD, I would also like to thank Conor Houghton.

38 Personally, I would like to thank my girlfriend Ashley, who has been nothing but helpful since
39 I met her.

40 Finally, I would like to thank my father, mother, brother and sister. I am truly fortunate to
41 have such a good family. I thank them for their love, encouragement, and excellent example.

42 *Abstract*

43 Since the use of multi-electrode recording in neuroscience began, the number neurons
44 being recorded in parallel has been increasing. Recently developed methods using calcium
45 or voltage imaging have also contributed to the growth in neuronal datasets. As datasets grow,
46 the need for new analysis methods also grows. In this research we attempted to address some
47 of the problems associated with reading from large neuronal ensembles using fluorescent
48 calcium indicators, and some of the problems with analysing data read from large neuronal
49 ensembles.

50 We created a biophysical model for the fluorescence trace produced by a calcium indicator
51 responding to a given spike train. Our model reproduced the characteristics of a real
52 fluorescence trace recognised by spike inference algorithms. This model will be useful for
53 anyone using or considering calcium imaging.

54 To find order in the correlated behaviour of a large multi-region neuronal ensemble, we
55 applied a novel method from network science to detect structure and communities in corre-
56 lated behaviour. We investigated the similarities between these communities and their brain
57 anatomy. Our results indicate local correlated networks function at shorter timescales (<
58 50ms), while multi-region correlated networks function over longer timescales (> 100ms).
59 This result agrees with previous findings from EEG data, but has not been shown before using
60 spiking data.

61 We developed a statistical model for the number of neurons spiking in a neuronal ensem-
62 ble based on the Conway-Maxwell-binomial distribution. Our aim was to capture correlated
63 activity in a neuronal population without measuring correlation coefficients directly. The
64 model captured correlated activity at very short timescales better than measuring correlation
65 coefficients. We also replicated one of the findings of Churchland et al. (2010) relating to
66 the quenching of neural variability at stimulus onset. We propose a connection between this
67 result and the changes in association captured by our model.

68 **Contents**

69	Declaration of Authorship	iii
70	Acknowledgements	v
71	Abstract	vii
72	1 Introduction	1
73	1.1 Overview	1
74	1.2 Modelling the fluorescence of calcium indicators	2
75	1.3 Functional networks	4
76	1.4 A new statistical model for capturing correlated behaviour	6
77	2 Sensitivity of the spikes-to-fluorescence transform to calcium indicator and neu-	
78	ron properties	9
79	2.1 Introduction	10
80	2.2 Methods	12
81	2.2.1 Calcium dynamics model	12
82	Photon release & capture	14
83	2.2.2 Parameter optimisation	15
84	Fixed parameters	17
85	2.2.3 Julia	17
86	2.2.4 Spike inference	18
87	Comparing spike inference quality	20
88	2.2.5 Perturbation analysis	20
89	2.2.6 Signal-to-noise ratio	21
90	2.2.7 Data sources	21
91	2.3 Results	21
92	2.3.1 A biophysical computational model can generate accurate fluores-	
93	cence traces from spike trains	21

94	2.3.2	Spike inference algorithms perform similarly on real data compared with time series simulated from the model	23
95	2.3.3	Relative effects of various buffers to the fluorescence signal	23
96	2.3.4	Spike inference accuracy is sensitive to indicator properties, and likely varies within and between cells	26
97	2.3.5	Single spike inference accuracy drops for high firing rates, but firing rate itself can be estimated from mean fluorescence amplitude	30
98	2.4	Discussion	32
102	3	Functional networks expand across anatomical boundaries as correlation time- scale increases	37
103	3.1	Introduction	38
104	3.2	Data	39
105	3.2.1	Brain regions	39
106	3.2.2	Video recordings	40
107	3.3	Methods	40
108	3.3.1	Binning data	40
109	3.3.2	Correlation coefficients	41
110		Total correlations, r_{SC}	41
111		Shuffled total correlations	42
112		Separating Correlations & Anti-correlations	42
113	3.3.3	Conditioning on behavioural data	42
114		Linear regression	42
115		Elastic net regularisation	43
116		Conditional covariance	44
117		Measures of conditional correlation	44
118	3.3.4	Information Theory	45
119		Entropy $H(X)$	45
120		Maximum entropy limit	46
121		Mutual Information $I(X; Y)$	47
122		Variation of Information $VI(X, Y)$	49
123		Measuring entropies & mutual information	49
124	3.3.5	Network analysis	49
125		Correlation networks	49

127	Rectified correlations	50
128	Sparsifying data networks	50
129	Communities	50
130	Weighted configuration model	51
131	Sparse weighted configuration model	51
132	Spectral rejection	51
133	Node rejection	52
134	Community detection	53
135	3.3.6 Clustering Comparison	53
136	Adjusted Rand Index	53
137	Clusterings as random variables	54
138	Information based similarity measures	55
139	Information based metrics	56
140	Comparing detected communities and anatomical divisions	56
141	3.4 Results	57
142	3.4.1 Average correlation size increases with increasing time bin width	57
143	3.4.2 Goodness-of-fit for Poisson and Gaussian distributions across increasing time bin widths	58
144	3.4.3 Differences between and inter- and intra- regional correlations decrease with increasing bin width	60
145	3.4.4 Connected and divided structure in correlation based networks reduces in dimension with increasing bin width	61
146	3.4.5 Detecting communities in correlation based networks	65
147	3.4.6 Functional communities resemble anatomical division at short timescales	65
148	3.4.7 Conditional correlations & signal correlations	67
149	3.4.8 Absolute correlations and negative rectified correlations	72
150	3.5 Discussion	75
151	4 A simple two parameter distribution for modelling neuronal activity and capturing neuronal association	79
152	4.1 Introduction	80
153	4.2 Data	81
154	4.2.1 Experimental protocol	81
155	4.3 Methods	82

160	4.3.1	Binning data	82
161	4.3.2	Number of <i>active</i> neurons	82
162	4.3.3	Moving windows for measurements	82
163	4.3.4	Fano factor	84
164	4.3.5	Probability Distributions suitable for modelling ensemble activity	84
165		Association	84
166		Binomial distribution	85
167		Beta-binomial distribution	85
168		Conway-Maxwell-binomial distribution	86
169	4.3.6	Fitting	88
170	4.3.7	Goodness-of-fit	90
171	4.4	Results	90
172	4.4.1	Increases in mean number of active neurons and variance in number of active neurons at stimulus onset in some regions	90
173		Primary visual cortex	91
174		Hippocampus	91
175		Thalamus	91
176	4.4.2	Conway-Maxwell-binomial distribution is usually a better fit than binomial or beta-binomial	91
177	4.4.3	Conway-Maxwell-binomial distribution captures changes in association at stimulus onset	96
178	4.4.4	Replicating stimulus related quenching of neural variability	96
179	4.4.5	Effects of wider bin sizes	98
180	4.5	Discussion	99
181	5	Studies with practical limitations & negative results	103
182	5.1	Dynamic state space model of pairwise and higher order neuronal correlations	104
183	5.2	A multiscale model for hierarchical data applied to neuronal data	104
184	6	Discussion	107
185	Bibliography		115

190 **List of Figures**

191	2.1 A: Example spike train (blue) and the corresponding GCaMP6s fluorescence	
192	trace (green), data replotted from (Berens et al., 2018). Inset shows zoomed	
193	section of traces to highlight slow decay of GCaMP6s fluorescence relative	
194	to spike time intervals. B: Schematic diagram of the neuron calcium and	
195	GCaMP computational model. C: Good visual match of data fluorescence	
196	trace (green) and model simulated fluorescence (orange) in response to an	
197	identical spike train (blue).	11
198	2.2 A: Workflow to compare spike inference for real versus simulated fluores-	
199	cence data. B: True positive rates achieved by three different spike inference	
200	algorithms when applied to observed spike trains, and simulated spike trains.	
201	Data points overlaid as blue circles. The performance is similar from real	
202	and simulated data for each of the algorithms.	24
203	2.3 Calcium Buffering Dynamics (A) The proportions of bound and free cal-	
204	cium concentrations within a cell, with the associated spike train. (B)-(F)	
205	The dynamics of the concentration of (B) excited indicator bound calcium,	
206	(C) indicator bound calcium, (D) immobile endogenous buffer bound cal-	
207	cium, (E) mobile endogenous buffer bound calcium, and (F) free calcium in	
208	response to an action potential at $\sim 23.2\text{s}$	25

209	2.4 (A) An example trace for each of the five pairs of values used for the binding	
210	and unbinding rates of the fluorescent calcium indicator. (B) The signal-to-	
211	noise ratio of the modelled fluorescence traces using each of the four per-	
212	turbed value pairs, and the experimental value. The SNRs for the value pairs	
213	perturbed downward are lower than that for the unperturbed value pair or	
214	the higher value pairs. (C) The true-positive rates of the deconvolution al-	
215	gorithm's predictions when inferring from the observed data, and inferring	
216	from modelled traces using the perturbed and experimental values. We used	
217	the CNMF algorithm for spike inference here. The results from the other	
218	spike inference methods were similar, with their true positive rates scales	
219	similarly to figure 2.2 B.	28
220	2.5 (A) An example trace for each of the five perturbed values for the concen-	
221	tration of fluorescent calcium indicator. The top two traces are produced	
222	by the lower perturbed values, the middle trace is produced by the experi-	
223	mental value, and the lowest two traces are produced when using the higher	
224	perturbed values. (B) The signal-to-noise ratio of the modelled fluorescence	
225	traces using each of the four perturbed values, and the experimental value.	
226	Extreme perturbations of the concentration either above or below the experi-	
227	mental level lowered the SNR. (C) The true-positive rates of the deconvolu-	
228	tion algorithm's predictions when inferring from the observed data, and	
229	inferring from modelled traces using the perturbed and experimental values.	
230	We found that the algorithms performs equally badly on the two most ex-	
231	treme values, and performs equally well on the experimental value, and the	
232	next higher perturbed value. We used the CNMF algorithm for spike infer-	
233	ence here. The results from the other spike inference methods were similar,	
234	with their true positive rates scales similarly to figure 2.2 B.	29

235	2.6 (A) An example trace for each of the five perturbed values for the concentration of immobile endogenous buffer. (B) The signal-to-noise ratio of the modelled fluorescence traces using each of the four perturbed values, and the experimental value. The lower values for the immobile buffer produce the same SNR as the experimental value. But the higher perturbed values produce fluorescence traces with a lower SNR. (C) The true-positive rates of the deconvolution algorithm's predictions when inferring from the observed data, and inferring from modelled traces using the perturbed and experimental values. We used the CNMF algorithm for spike inference here. The results from the other spike inference methods were similar, with their true positive rates scales similarly to figure 2.2 B.	31
246	2.7 Simulating fluorescence traces at different firing rates Example modelled traces created using simulated spike trains with a mean firing rate of 1Hz (left column), 5Hz (middle column), and 10Hz (right column). Note the difference in amplitude with different mean firing rates.	32
250	2.8 Inference quality and $\Delta F / F_0$ vs Firing rate (left) The spike inference accuracy when applied to 30 traces created using simulated spike trains with mean firing rates of 1, 5, and 10 Hz. (right) The mean $\Delta F / F_0$ across those 30 traces for each frequency.	32
254	3.1 Probe Locations: The locations of the probes in each of the three mouse brains (Stringer et al., 2019).	40
256	3.2 Entropy Limit: The upper limit on entropy of binned spike count data as a function of the maximum observed spike count. The orange line is the analytical maximum. The blue line is the entropy of samples with $N = 1000$ data points taken from the discrete uniform distribution.	47
260	3.3 (A) An example of the correlation coefficients between two different pairs of cells, one where both cells are in the same brain region (intra-regional pair), and one where both cells are in different brain regions (inter-regional pair). The correlation coefficients have been measured using different time bin widths, ranging from 5ms to 3s. Note the increasing amplitude of the correlations with increasing bin width. (B) A raster plot showing the spike times of each pair of cells.	57

267	3.4 Mean correlation coefficients measured from pairs of 50 randomly chosen 268 neurons. (A) All possible pairs, (B) positively correlated pairs, and (C) neg- 269 atively correlated pairs. (D) Mean and standard error of χ^2 test statistics for 270 Poisson and Gaussian distributions fitted to neuron spike counts.	59
271	3.5 (Left)The mean intra-region and inter-region correlations using all possible 272 pairs of ~ 500 neurons, spread across 9 different brain regions. (Right) 273 Courtesy of Stringer et al. (2019), mean inter-regional (out-of-area) correla- 274 tion coefficients vs mean intra-regional (within-area) correlation coefficients 275 for a bin width of 1.2s. Note that the intra-regional coefficients are higher in 276 each case.	61
277	3.6 The mean intra-regional correlations (coloured dots) and mean inter-regional 278 correlations (black dots) for a given region, indicated on the x-axis, for dif- 279 ferent time bin widths. Each black dot represents the mean inter-regional 280 correlations between the region indicated on the x-axis and one other region. 281 (A) shows these measurements when we used a time bin width of 5ms. (B) 282 shows these measurements when we used a time bin width of 1s. Note that 283 the difference between the mean inter-regional correlations and mean intra- 284 regional correlations is smaller for 1s bins.	62
285	3.7 Mean inter-regional (main diagonal) and intra-regional (off diagonal) corre- 286 lation coefficients. (A) Shows these measurements when spike times were 287 binned using 5ms time bins. (B) Shows the same, using 1s time bins. Note 288 that the matrices are ordered according to the main diagonal values, therefore 289 the ordering is different in each subfigure.	63
290	3.8 The number of dimensions in the k -partite and connected structure in the cor- 291 relation based networks beyond the structure captured by a sparse weighted 292 configuration null network model (see section 3.3.5), shown for different time 293 bin widths. Note that the k -partite structure disappears for time bin width 294 greater than 200ms for all three subjects. The dimension of the connected 295 structure reduces with increasing bin width for 2 of the 3 subjects (top row). .	64

296	3.9 (A-B) Correlation matrices with detected communities indicated by white	
297	lines. Each off main diagonal entry in the matrix represents a pair of neu-	
298	rons. Those entries within a white square indicate that both of those neurons	
299	are in the same community as detected by our community detection proce-	
300	dure. Matrices shown are for 5ms and 1s time bin widths respectively. Main	
301	diagonal entries were set to 0. (C-D) Matrices showing the anatomical dis-	
302	tribution of pairs along with their community membership. Entries where	
303	both cells are in the same region are given a colour indicated by the colour	
304	bar. Entries where cells are in different regions are given the grey colour also	
305	indicated by the colour bar.	66
306	3.10 (A) The variation of information is a measure of distance between cluster-	
307	ings. The distance between the anatomical ‘clustering’ and community de-	
308	tection ‘clustering’ increases with increasing time bin width. (B) The ad-	
309	justed Rand index is a normalised similarity measure between clusterings.	
310	The anatomical and community detection clusterings become less similar as	
311	the time bin width increases.	67
312	3.11 Comparing the components of the total covariance across different values for	
313	the time bin width. We observed a consistent increase in $E[\text{cov}(X, Y Z)]$ as	
314	the time bin width increased. But we saw different trends for $\text{cov}(E[X Z], E[Y Z])$	
315	for each mouse.	68
316	3.12 Comparing the components of the total covariance across different values for	
317	the time bin width. We saw a consistent increase in $\rho_{X,Y Z}$ as the time bin	
318	width increased in all three subjects. But we saw different trends in ρ_{signal} for	
319	each of the subjects.	69
320	3.13 Matrices showing the regional membership of pairs by colour, and the com-	
321	munities in which those pairs lie. (A-B) Detected communities and regional	
322	membership matrix for network based on rectified spike count correlation	
323	$\rho_{X,Y Z}$, using time bin widths of 0.005s and 1s respectively. (C-D) Detected	
324	communities and regional membership matrix for network based on rectified	
325	signal correlation ρ_{signal} , using time bin widths of 0.005s and 1s respectively.	70

326	3.14 Distance and similarity measures between the anatomical division of the neu-	
327	rons, and the communities detected in the network based on the spike count	
328	correlations $\rho_{X,Y Z}$. (A) The variation of information is a ‘distance’ mea-	
329	sure between clusterings. The distance between the anatomical ‘clustering’	
330	and the community clustering increases as the time bin width increases. (B)	
331	The adjusted Rand index is a similarity measure between clusterings. The	
332	detected communities become less similar to the anatomical division of the	
333	cells as the time bin width increases.	71
334	3.15 Distance and similarity measures between the anatomical division of the neu-	
335	rons, and the communities detected in the network based on the signal cor-	
336	relations ρ_{signal} . (A) The variation of information is a ‘distance’ measure be-	
337	tween clusterings. The distance between the anatomical ‘clustering’ and the	
338	community clustering increases as the time bin width increases. (B) The ad-	
339	justed Rand index is a similarity measure between clusterings. The detected	
340	communities become less similar to the anatomical division of the cells as	
341	the time bin width increases.	72
342	3.16 (A-B) Absolute correlation matrices with detected communities indicated by	
343	white lines. These communities are based on the absolute value of the total	
344	correlation between each pair of cells. Those entries within a white square in-	
345	dicate that both of those neurons are in the same community. Matrices shown	
346	are for 5ms and 1s time bin widths respectively. Main diagonal entries were	
347	set to 0. (C-D) Matrices showing the anatomical distribution of pairs along	
348	with their community membership. Regional membership is indicated by the	
349	colour bar. (E) Variation of information between the anatomical division of	
350	the cells, and the detected communities. (F) Adjusted Rand index between	
351	the anatomical division, and the detected communities.	73

352	3.17 (A-B) Sign reversed rectified correlation matrices with detected communities indicated by white lines. Those entries within a white square indicate that both of those neurons are in the same community. Matrices shown are for 5ms and 1s time bin widths respectively. Main diagonal entries were set to 0. (C-D) Matrices showing the anatomical distribution of pairs along with their community membership. Regional membership is indicated by the colour bar. (E) Variation of information between the anatomical division of the cells, and the detected communities. (F) Adjusted Rand index between the anatomical division, and the detected communities.	74
361	4.1 Figures showing the over-dispersion possible for a beta-binomial distribution relative to a binomial distribution. Parameters are shown in the captions. . .	86
362		
363	4.2 Figures showing (A) the under-dispersion and (B) over-dispersion permitted by the COMb distribution relative to a binomial distribution. (C) illustrates that the p parameter of the COMb distribution does not correspond to the mean of the distribution, as it does for the binomial and beta-binomial distributions. (D) shows a heatmap for the value of the Kullback-Liebler divergence between the COMb distribution and the standard binomial distribution with same value for n , as a function of p and ν . The point of this figure is to give the reader a sense of how the values of p and ν influence the difference between the COMb distribution and the binomial distribution. The divergence is smallest when $\nu \approx 1$, or when $p \approx 0.5$. When $\nu = 1$, the PMF for the COMb distribution is the same as the PMF for the binomial distribution. When $p = 0.5$ the mass of the distribution is centred around $n/2$ for both the COMb and the binomial distribution. The difference between the two distributions is controlled by the ν parameter. The further the p and ν parameters are from 0.5 and 1 respectively, the greater the difference between the COMb distribution and the binomial distribution. Parameters for all figures are shown in the captions.	89
364		
365		
366		
367		
368		
369		
370		
371		
372		
373		
374		
375		
376		
377		
378		
379		

380	4.3 (A) Raster plot showing the spikes fired by 33 randomly chosen neurons in	
381	the primary visual cortex. (B-C) (B) average and (C) variance of the number	
382	of active neurons, measured using a sliding window 100ms wide, split into	
383	100 bins. The midpoint of the time interval for each window is used as the	
384	timepoint (x-axis point) for the measurements using that window. The grey	
385	shaded area indicates the presence of a visual stimulus. The opaque line is	
386	an average across the 160 trials that included a visual stimulus of any kind.	
387	We can see a transient increase in the average number of active neurons and	
388	the variance of this number, followed by a fluctuation and another increase.	92
389	4.4 (A) Raster plot showing the spikes fired by 33 randomly chosen neurons in	
390	the hippocampus. (B-C) (B) average and (C) variance of the number of active	
391	neurons, measured using a sliding window 100ms wide, split into 100 bins.	
392	The midpoint of the time interval for each window is used as the timepoint (x-	
393	axis point) for the measurements using that window. The grey shaded area	
394	indicates the presence of a visual stimulus. The opaque line is an average	
395	across the 160 trials that included a visual stimulus of any kind. We can see	
396	a transient increase in the average number of active neurons and the variance	
397	of this number at stimulus onset.	93
398	4.5 (A) Raster plot showing the spikes fired by 33 randomly chosen neurons in	
399	the thalamus. (B-C) (B) average and (C) variance of the number of active	
400	neurons, measured using a sliding window 100ms wide, split into 100 bins.	
401	The midpoint of the time interval for each window is used as the timepoint (x-	
402	axis point) for the measurements using that window. The grey shaded area	
403	indicates the presence of a visual stimulus. The opaque line is an average	
404	across the 160 trials that included a visual stimulus of any kind. We can	
405	see in immediate increase at stimulus onset, a subsequent fall, and another	
406	sustained increased until the stimulus presentation ends.	94

407	4.6 (A) An example of the binomial, beta-binomial, and Conway-Maxwell-binomial	
408	distributions fitted to a sample of neural activity. The Conway-Maxwell-	
409	binomial distribution is the best fit in this case. The histogram shows the	
410	empirical distribution of the sample. The probability mass function of each	
411	distribution is indicated by a different coloured line. (B) Across all samples	
412	in all trials, the proportion of samples for which each fitted distribution was	
413	the best fit. The Conway-Maxwell-binomial distribution was the best fit	
414	for 93% of the samples taken from V1 using a bin width of 1ms.	95
415	4.7 (A) We fit a Conway-Maxwell-binomial distribution to the number of active	
416	neurons in 1ms time bins of a 100ms sliding window. We did this for all	
417	trials with a visual stimulus and took the average across those trials. We see	
418	a transient drop in value for the distribution's ν parameter at stimulus onset.	
419	This shows an increase in positive association between the neurons. (B) We	
420	measured the correlation coefficient between the spike counts of all possible	
421	pairs of neurons in the same sliding window. The took the average of those	
422	coefficients. We also did this for every visually stimulated trial, and took the	
423	average across trials. The increase in positive association is not reflected with	
424	an increase in average correlation.	97
425	4.8 (A) The mean Fano factor of the spike counts of the cells in the primary visual	
426	cortex. Means were taken across cells first, then across trials. There was a	
427	significant decrease in the Fano factors immediately after stimulus onset. (B)	
428	The mean Fano factor of the spike counts of the cells in the motor cortex. No	
429	significant change in measurements at any point.	98
430	4.9 (A) The mean ν parameter of the COMb distribution fitted to activity in the	
431	primary visual cortex. Mean taken across all stimulated trials. A bin width of	
432	10ms was used to classify cells as active or inactive. The change in associa-	
433	tion at stimulus onset is still captured. Some high frequency fluctuations are	
434	filtered out by using the wider bins (compare to figure 4.7a) (B) The mean	
435	Fano factor of the cells in the primary visual cortex. The change in the mean	
436	Fano factor at stimulus onset is not significant when using a bin width of 10ms.	100

437 **List of Tables**

438 2.1 Fixed parameters A table of the parameters fixed before optimising the	
439 model. The values of these parameters could be changed to model differ-	
440 ent fluorescent calcium indicators.	17
441 4.1 Details of the different bin width and analysis window sizes used when bin-	
442 ning spike times, and analysing those data.	83
443 4.2 Relative dispersion of the COMb distribution, and association between Bernoulli	
444 variables as represented by the value of the ν parameter.	88
445 4.3 Proportion of samples for which each distribution was the best fit, grouped	
446 by bin width. The COMb distribution is the best fit most of the time.	96

List of Abbreviations

COMb	Conway-Maxwell-binomial (distribution)
OASIS	Online active set method to infer spikes
SNR	Signal to noise ratio
NMI	Normalised mutual information
AMI	Adjusted mutual information
VI	Variation of information

⁴⁴⁸ **List of Symbols**

$[Ca^{2+}]$	Free calcium concentration	mol
$[BCa]$	Fluorescent indicator bound calcium	mol
$[ECa]$	Endogenous mobile buffer bound calcium	mol
$[ImCa]$	Immobile mobile buffer bound calcium	mol
$[BCa^*]$	excited fluorescent indicator bound calcium	mol
k_{X_f}	binding (affinity) rate	$mol^{-1} s^{-1}$
k_{X_b}	unbinding (dissociation) rate	s^{-1}

449 **Chapter 1**

450 **Introduction**

451 **1.1 Overview**

452 Since Hodgkin and Huxley's squid experiments featuring a single axon (Hodgkin and Hux-
453 ley, 1939), to more recent research with spike sorted data from ~ 24000 neurons from 34
454 brain regions from 21 mice (Allen et al., 2019), the number of neurons contributing to elec-
455 trophysiological datasets has been growing. The number of simultaneously recorded neurons
456 has doubled approximately every seven years since the use of multi-electrode recording in
457 neuroscience began (Stevenson and Kording, 2011). Recording methods using two-photon
458 calcium imaging have also been used to extract data from populations containing over 10000
459 neurons (Peron et al., 2015). This dramatic growth in the number of neurons available for
460 analysis requires a dramatic change in analysis methods.

461 There are multiple methods for reading activity from neuronal ensembles: electrophysiolog-
462 ogy, calcium imaging, and voltage imaging. Electrophysiology involves inserting electrodes
463 into the brain of an animal. The electrodes read extra-cellular membrane potential, and using
464 these readings we observe activity in the ensemble. Calcium imaging and voltage imaging
465 use indicator dyes or fluorescent proteins that emit fluorescence traces that indicate either
466 the concentration of calcium in a neuron's cytoplasm, or the neuron's membrane potential.
467 In this project, we have attempted to address some of the difficulties in collecting data from
468 these large ensembles using fluorescent calcium indicators, and some of the difficulties in
469 analysing the collected data.

470 The rest of this introductory chapter will give some background about methods of record-
471 ing from the brain, and some background for the rest of the document. Chapter two describes
472 a biophysical model for the fluorescence trace induced by a given spike train in a cell con-
473 taining a fluorescent calcium indicator. Our third chapter describes our investigations into

the correlated activity across different regions of a mouse behaving spontaneously. We applied a novel community detection method (Humphries et al., 2019) from network science to correlation based networks of neurons, and observed differences in the structure of these correlations at different timescales. In our fourth chapter, we detail a new statistical model for the number of neurons spiking in a neuronal ensemble at any given moment. With this model, we attempted to capture correlated activity in a new way. The fifth chapter is a brief description of the work that yielded negative results or was abandoned. The final chapter is a discussion of our work and results from the previous chapters and their implications.

1.2 Modelling the fluorescence of calcium indicators

To focus on calcium imaging for a start, a neuron that contains a fluorescent calcium indicator in its cytoplasm will fluoresce when bombarded with photons. The amount that the cell will fluoresce is dependent on the concentration of fluorescent indicator within the cell, and the concentration of calcium within the cell. When a neuron fires an action potential, the influx of free calcium ions causes an increase in fluorescence when those ions bond with the fluorescent indicator and those bounded molecules are bombarded with photons. After the action potential, as calcium is extruded from the cell the fluorescence returns to a baseline level. This is the basic mechanism of fluorescent calcium indicator based imaging.

This method has some advantages over electrophysiology as measure of neuronal ensemble activity. Many of the problems with electrophysiology are within the processes used to isolate spikes in the extracellular voltage readings, and assign these spikes to individual cells. These processes are collectively called ‘spike sorting’. A comparison of many different spike sorting algorithms found that these algorithms only agreed on a fraction of cases (Buccino et al., 2019). Furthermore, because electrodes measure extracellular voltage, neurons that do not spike will not be detected. Isolating individual neurons is easier and more reliable when using calcium imaging data, because cells will emit a baseline level of fluorescence when not firing action potentials. Another advantage is that calcium imaging sites can be re-used for weeks for longitudinal studies (Chen et al., 2013). One of the methods of delivering the fluorescent indicator is by adeno-associated viruses, consequently there can be problems with indicator gradients around the infection site, and expression levels will change in individual cells over weeks (Tian et al., 2009; Chen et al., 2013). This delivery method can also cause cell pathology, and nuclear filling (Zariwala et al., 2012), but these problems can be solved by using lines of transgenic mice (Dana et al., 2014). The fluorescence signal itself can serve as a

506 good indicator of cell activity, but similarly to electrophysiology, the aim of calcium imaging
507 is often spike detection.

508 If the imaging data is collected at a high enough frequency, and the signal-to-noise ratio
509 of the fluorescence trace is high enough, it should be possible to infer the spike times to some
510 level of accuracy. For example, the calmodulin based indicator GCaMP6s has a sufficiently
511 high signal-to-noise ratio that isolated action potentials can be detected and inferred (Chen
512 et al., 2013). Many spike inference algorithms exist (Vogelstein et al., 2010; Pnevmatikakis
513 et al., 2016; Friedrich and Paninski, 2016; Pnevmatikakis et al., 2013; Pnevmatikakis et al.,
514 2014; Deneux et al., 2016; Greenberg et al., 2018), and some of these can perform both cell
515 isolation and spike detection simultaneously (Vogelstein et al., 2010; Pnevmatikakis et al.,
516 2016; Pnevmatikakis et al., 2014; Deneux et al., 2016). But the relationship between spik-
517 ing and fluorescence change is not fully understood. For example, the fluorescent indicator
518 will act like an additional calcium buffer within the cell cytoplasm and will compete with
519 the other endogenous buffers to bind with free calcium ions. Therefore, the concentration
520 of those endogenous buffers, and the binding dynamics of those buffers will have an effect
521 on the change in fluorescence in response to an action potential. Furthermore, the binding
522 dynamics of the fluorescent indicator itself will have an effect on the change in fluorescence.
523 For example, the GCaMP series of fluorescence indicators are based on the calcium buffer
524 protein calmodulin. This protein has four binding sites, whose affinities interact non-linearly.
525 But most of the spike inference algorithms model the fluorescence as a linear function of
526 a calcium trace, and they model this calcium trace as a first or second order autoregression
527 with a pulse input to represent action potentials. Deneux et al. (2016) developed two dif-
528 ferent calcium fluorescence models behind their spike inference algorithm (MLspike) with a
529 more biological inspiration. For their simpler model, they take a physiological approach and
530 account for baseline calcium indicator dynamics. They end up with a system of first order
531 differential equations defining the dynamics of calcium concentration, baseline fluorescence,
532 and fluorescence. For their more complicated model specifically for genetically encoded cal-
533 cium indicators, they also took into account indicator binding and unbinding rates, which
534 added another equation to their system of equations. The algorithms that use the autore-
535 gression model and the MLspike algorithm are outperformed by the most recently published
536 spike inference algorithm (Greenberg et al., 2018). This algorithm takes into account the
537 binding dynamics of both the endogenous buffers and fluorescent calcium indicator, and the
538 concentrations of free calcium, indicator, and endogenous buffer within the cell cytoplasm.
539 The performance of this algorithm shows that there is value in more biologically inspired

540 models of fluorescent calcium indicators.

541 In light of the growing popularity of two-photon calcium imaging, and the lack of bio-
542 logically inspired spike inference algorithms ((Greenberg et al., 2018) developed their spike
543 inference algorithm in parallel to our work), we decided to develop a biologically inspired
544 model for fluorescent calcium indicator fluorescence. The idea being that our model would
545 take a spike train, or simply spike times, provided by the user, and return the fluorescence
546 trace that would be induced by this spike train or spike times. The model contains parameters
547 for concentrations of indicator and endogenous buffers, as well as affinity and unbinding rates
548 for these buffers. There are also parameters for the baseline concentration of free calcium in
549 the cell cytoplasm, and the cell radius (as a means for calculating the cell volume). With this
550 model, we hoped that experimentalists would be able to test out different calcium indicators
551 on the types of spike trains that they expect to encounter. This way they could decide ahead
552 of time which indicator suited their situation best. Since the output of our model is a fluo-
553 rescence trace, the spike inference models mentioned above can be applied to the modelled
554 fluorescence. This means that the model could also be used to benchmark the performance
555 of these spike inference algorithms, and to investigate the impact of variations in the model
556 on spike inference accuracy.

557 1.3 Functional networks

558 We have outlined some of the advantages that calcium imaging has over electrophysiology.
559 But electrophysiology is more useful in some situations. One particular drawback for two-
560 photon calcium imaging is that usually it can only be used for imaging near to the surface
561 of the brain. This problem can be solved by removing the tissue around the area to be im-
562 aged, and custom building a two-photon microscope Dombeck et al., 2010. Imaging with
563 three (or presumably more) photons may solve this problem in the future (Ouzounov et al.,
564 2017). A better option for reading activity from neurons beyond the surface of the brain is to
565 use Neuropixels probes (Jun et al., 2017). These probes can be used to read from thousands
566 of neurons simultaneously in many different areas of the brain (Allen et al., 2019; Stringer
567 et al., 2019; Steinmetz, Carandini, and Harris, 2019; Steinmetz et al., 2019). This brings us
568 to another problem for which we require new innovations in our analysis methods. Specif-
569 ically, analysing correlated behaviour in neural ensembles consisting of neurons from many
570 different brain regions.

571 Until the invention of new technologies such as the Neuropixels probes, most elec-
572 trophysiology datasets read from neurons in only one or two regions. Therefore most of
573 the research on interactions between neurons in different regions is limited to two regions
574 (Wierzynski et al., 2009; Patterson et al., 2014; Girard, Hupé, and Bullier, 2001). In chapters
575 3 and 4 we used datasets with neurons from 9 and 5 different brain regions respectively. In
576 their review of the interaction between growing the number of neurons in datasets and the
577 analysis methods applied to those dataset, Stevenson and Kording (2011) assert that an im-
578 portant objective of computational neuroscience is to find order in these kinds multi-neuron
579 of datasets. This was our main aim for the research described in chapter 3.

580 In light of recent findings based on correlated behaviour showing that spontaneous be-
581 haviours explain activity in many different parts of the brain that would otherwise be regarded
582 as noise (Stringer et al., 2019), that satiety is represented brain wide (Allen et al., 2019), and
583 that exploratory and non-exploratory states are represented in the amygdala (Gründemann
584 et al., 2019), it was clear that state representation or motor control had an influence on cor-
585 related behaviour in areas of the brain not usually associated with these tasks. Also, given
586 differences in timescales of fluctuations in different brain regions (Murray et al., 2014), and
587 different timescales for event representation in different brain regions (Baldassano et al.,
588 2017), we decided to investigate brain wide correlated behaviour at timescales ranging from
589 5ms up to 3s.

590 We started off measuring the correlations in spike counts between individual neurons in
591 our ensemble. These measurements induced a weighted undirected graph where each node
592 represented a neuron, and the weight of each edge was the strength of the correlation be-
593 tween the neurons represented by the nodes at either end of that edge. In order to put the
594 neurons into groups with correlated behaviour, we applied a novel community detection al-
595 gorithm (Humphries et al., 2019) to this graph. We repeated this analysis for timescales
596 from milliseconds to seconds. Bear in mind that our correlation based graph was completely
597 agnostic of the anatomical regions in which our cells resided. We then compared our corre-
598 lated communities to their anatomy at each timescale. In this way, we used a novel method,
599 never applied neuronal data before, to analyse the makeup of correlated communities across
600 different regions at different timescales.

601 1.4 A new statistical model for capturing correlated behaviour

602 Many important findings have been made by measuring the correlations between binned
 603 spike counts, but there are some problems with this method of analysis. Firstly, the width
 604 of the bins used to bin spike times into spike counts has an effect on the magnitude of the
 605 correlations measured. Using a short bin width can cause your measurements to be artificially
 606 small (Cohen and Kohn, 2011). This may not be an issue if one is considering relative size of
 607 correlations when using the same bin width, but it is still not ideal. Secondly, while pairwise
 608 correlations can capture most of the information in a small network (up to 40 cells) of highly
 609 correlated cells (Schneidman et al., 2006), a model based on pairwise correlations alone will
 610 fail to capture the activity of larger (~ 100 cells) networks, higher order correlated activity
 611 is required (Ganmor, Segev, and Schneidman, 2011). One problem with these higher order
 612 correlations is that they may be defined in different ways (Staude, Grün, and Rotter, 2010).
 613 Furthermore if we want to include them in a model this usually involves greatly increasing the
 614 number of parameters to fit, which increases the dimension of the parameter space leading
 615 to the ‘curse of dimensionality’. Some models attempt to sidestep these problems while
 616 still capturing higher-order correlations. These models attempt to capture the relationship
 617 between each individual neuron in the ensemble, and the ensemble as a whole. Okun et al
 618 (2015) called the strength of this relationship the ‘population coupling’, and demonstrated
 619 that this quantity can predict an individual neuron’s response to optogenetic stimulation of
 620 the whole ensemble. They also showed that this quantity was an indicator of the neuron’s
 621 synaptic connectivity (Okun et al., 2015). With the ‘population tracking model’, O’Donnell
 622 et al. (2016) linked the probability of firing an action potential for each individual neuron
 623 with the distribution of the number of active neurons. This allowed model fitting for a large
 624 number of neurons, as well as calculation of full pattern probabilities, and population entropy
 625 (O’Donnell et al., 2017).

626 In this work, we also aimed to capture correlated behaviour between the neurons in a
 627 neuronal ensemble without measuring correlations directly. Correlation coefficients capture
 628 the linear component of the relationship between two random variables, but will not mea-
 629 sure any relationship beyond linearity. Also, measuring correlation coefficients using short
 630 timebins can be difficult for neuronal data (Cohen and Kohn, 2011). We decided to abandon
 631 correlation, and we aimed to quantify a more general concept of association by modelling
 632 the number of active neurons in the ensemble using a Conway-Maxwell-binomial (COMb)
 633 distribution (Kadane, 2016).

634 The COMb distribution is a probability distribution over the number of successes in a
635 sequence of Bernoulli trials, where these trials can be associated in some way. The COMb
636 distribution is an extension of the standard binomial distribution, with an additional parameter
637 to model association between the Bernoulli variables. Using this additional parameter the
638 distribution can capture positive association, where the Bernoulli variables tend to take the
639 same value, negative association, where the Bernoulli variables tend to take opposite values,
640 or no association i.e. the standard binomial distribution.

641 We fit a COMb distribution to spike sorted electrophysiological data taken from five
642 different regions in the brain of an awake mouse exposed to visual stimuli (Steinmetz et al.,
643 2019). We examined whether or not a model based on the COMb distribution was able to
644 capture changes in the number of active neurons in these neuronal ensembles in response to
645 the stimuli. We also investigated the relationship between the changes as captured by the
646 COMb model and the change in neural variability as measured by Churchland et al. in their
647 famous paper (Churchland et al., 2010).

648 Our overall aim was to investigate some of the challenges in analysing large ensembles
649 of neurons present today. That included collecting the data to analyse (via calcium imaging),
650 and subsequently analysing these data. We felt that this was a worthwhile project because
651 the size of datasets, in terms of numbers of neurons and data collected, is growing rapidly.
652 Consequently these challenges will only become greater unless they are addressed. This is
653 our attempt at addressing them.

654 **Chapter 2**

655 **Sensitivity of the**
656 **spikes-to-fluorescence transform to**
657 **calcium indicator and neuron**
658 **properties**

659 *Abstract*

660 Fluorescent calcium indicators such as GCaMP are widely used to monitor neuronal activity.
661 However the relationship between the fluorescence signal and the underlying action potential
662 firing is poorly understood. This lack of knowledge makes it difficult for experimenters
663 to decide between different indicator variants for a given application. We addressed this
664 problem by studying a basic biophysical model of calcium dynamics in neuronal soma. We
665 fit the model parameters to publicly available data where GCaMP6s fluorescence and whole-
666 cell electrophysiological recordings were made simultaneously in the same single neurons.
667 We systematically varied the model's parameters to characterise the sensitivity of spike train
668 inference algorithms to the calcium indicator's main biophysical properties: binding rate,
669 dissociation rate, and molecular concentration. This model should have two potential uses:
670 experimental researchers may use it to help them select the optimal indicator for their desired
671 experiment; and computational researchers may use it to generate simulated data to aid design
672 of spike inference algorithms.

673 **2.1 Introduction**

674 Although fluorescent calcium indicators such as GCaMP are widely used to monitor neuronal
675 activity, the relationship between the fluorescence signal and the underlying action potential
676 firing is imperfect. The fluorescence signal has a low signal-to-noise ratio, and most indica-
677 tors' kinetics are slow relative to the millisecond-timescale dynamics of the membrane volt-
678 age (example in figure 2.1A). This makes spike inference difficult. Furthermore, the effects
679 of the indicator and cell properties on the fluorescence signal are unknown. For example,
680 genetically encoded indicators can accumulate within neurons over weeks and months (Chen
681 et al., 2013). Studies using calcium-sensitive fluorescent dyes have shown that indicator con-
682 centration has substantial effects on the spike-to-fluorescence relationship (Maravall et al.,
683 2000). Therefore spike rates inferred from GCaMP fluorescence signals may give mislead-
684 ing results if comparing across imaging sessions. More generally, the poor understanding of
685 the spike-to-fluorescence transform means experimenters may not know whether to trust the
686 outputs of spike train inference methods in any given application.

687 Spike trains are usually inferred from the time series of intensity values of one pixel of the
688 fluorescence image, where the pixel is located at the cell's soma. The problems of identifying
689 these pixels, and inferring spikes from their time series can solved separately or together.
690 When attempting to infer spikes, the fluorescence trace is modelled as a linear combination of
691 calcium concentration dynamics, a baseline calcium concentration, and some Gaussian noise.
692 The calcium concentration dynamics are modelled as an autoregressive process of degree 1
693 or 2 with a pulse input corresponding to the spike train, or the number of spikes fired in a
694 time step. The model includes no dynamics for the fluorescent indicator itself. Furthermore,
695 in order to make this model into an easily solvable linear programming problem the number
696 of spikes fired in a timestep is not restricted to non-negative integers but to arbitrary non-
697 negative values (Vogelstein et al., 2010; Pnevmatikakis et al., 2016; Friedrich and Paninski,
698 2016; Pnevmatikakis et al., 2013; Pnevmatikakis et al., 2014). More biologically inspired
699 spike inference models do exist (Deneux et al., 2016), but their fundamentals are very similar.
700 In this work, we investigated the effect of changing dynamics and buffer concentrations on
701 the accuracy of the inference algorithms based on these models.

702 The aim of this project was to model the fluorescence traces produced by a fluorescent
703 calcium indicator in a neuron soma resulting from a specific spike train, given calcium indi-
704 cator parameters such as binding rate, dissociation rate, and molecular concentration. Such

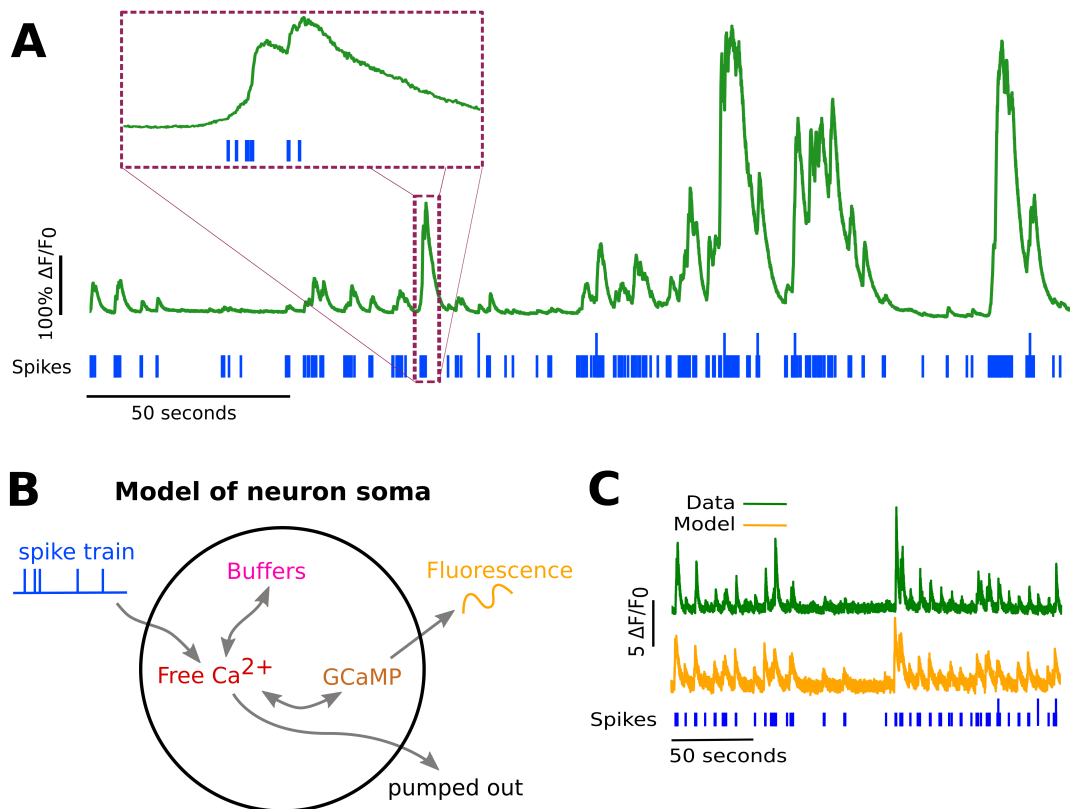


FIGURE 2.1:

- A: Example spike train (blue) and the corresponding GCaMP6s fluorescence trace (green), data replotted from (Berens et al., 2018). Inset shows zoomed section of traces to highlight slow decay of GCaMP6s fluorescence relative to spike time intervals.
- B: Schematic diagram of the neuron calcium and GCaMP computational model.
- C: Good visual match of data fluorescence trace (green) and model simulated fluorescence (orange) in response to an identical spike train (blue).

705 a model would allow benchmarking of various spike inference algorithms, and enable under-
706 standing of how indicator characteristics affect the quality of spike train inference.

707 The model we developed consisted of free calcium, fluorescent indicator molecules, and
708 mobile and immobile endogenous calcium buffers. The indicator molecules which were
709 bound to a calcium molecule could be either excited, i.e. able to release a photon, or relaxed.
710 In order to reproduce the noise inherent in the data collection, we modelled the release of
711 photons from the excited indicator bound calcium as a stochastic process.

712 The fluorescence traces produced by the simulation were calibrated to reproduce the
713 signal-to-noise ratio observed in experimental data. Previously published spike inference
714 algorithms were then used to infer spike trains from the experimental fluorescence traces and
715 the modelled fluorescence traces. The parameters of the model were then varied in order to
716 determine the effect on the system dynamics and the effects on spike inference.

717 2.2 Methods

718 2.2.1 Calcium dynamics model

719 We wrote a biophysical model of the calcium dynamics within a cell soma. When a neuron
720 fires an action potential, voltage-dependent calcium ion-channels open up that allow a current
721 of calcium ions (Ca^{2+}) to flow into the neuron (Koch, 1999). The increase in the free calcium
722 ion concentration inside of the cell, along with changes in the concentration of potassium
723 and sodium, causes the change in cell membrane potential, which must be repolarised. The
724 repolarising process consists of free calcium ions leaving the cell through open ion channels,
725 or binding to molecules within the cell called buffers, or calcium storage by organelles such
726 as the endoplasmic reticulum. A diagram illustrating the cell, its channels, and its buffers
727 can be seen in figure 2.1A. There are several different types of calcium buffer, each with
728 different dynamics and different concentrations within different types of excitable cell. The
729 fluorescent calcium indicator is another calcium buffer, with the useful property that when it
730 is bound to a calcium ion, the bound molecule may become excited by a photon and release
731 a photon in return. This is what creates the fluorescence. After the action potential has taken
732 place, the free calcium concentration within the cell will return to a baseline level (Maravall
733 et al., 2000).

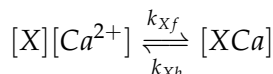
734 We modelled the the dynamics of five molecular concentrations,

- 735 • Free calcium ion concentration, $[\text{Ca}^{2+}]$

2.2. Methods

- 736 • Fluorescent indicator bound calcium, $[BCa]$
- 737 • Endogenous mobile buffer bound calcium, $[ECa]$
- 738 • Endogenous immobile buffer bound calcium, $[ImCa]$
- 739 • Excited buffered calcium, $[BCa^*]$

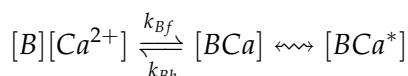
The term ‘buffering’ refers to free calcium ions coming into contact with buffer molecules followed by the binding of those molecules. Diagrammatically:



740 where $[X]$ represents any buffer molecule, and k_{X_f} and k_{X_b} represent the binding (association)
741 and unbinding (dissociation) rates in units of per molar concentration per second (M^{-1}
742 s^{-1}) and per second (s^{-1}) respectively. The speed of this chemical reaction is determined by
743 the binding and unbinding rates.

744 There are a number different endogenous buffers in any neuron. Which buffers are
745 present, and the buffers’ concentrations vary from cell to cell. In order to capture the ef-
746 fects of different kinds of buffers without modelling dozens of different individual buffers,
747 we modelled two different kinds of buffer only. These ‘mobile’ and ‘immobile’ buffers were
748 designed to be aggregations of the effects of multiple different buffers into two effective
749 buffers with different concentrations and binding rates. (Bartol et al., 2015) also divide cal-
750 cium buffers into mobile and immobile varieties. Note that since the model has no spatial
751 component, the mobile and immobile buffers only differ in their binding and unbinding rates.

The fluorescent calcium indicator behaves similarly to the other calcium buffers. The cal-
cium is buffered by the indicator in the same way. But an indicator bound calcium molecule
can become excited by absorbing the energy from a photon. An excited indicator bound
calcium molecule can then release a photon to go back to its ‘relaxed’ state.



752 The released photons are captured by a photon collector. This gives us the fluorescence trace.

753 The system of equations we used to model all of these interactions is as follows:

$$\begin{aligned} \frac{d[Ca^{2+}]}{dt} = & k_{Bb}[BCa] + k_{Eb}[ECa] + k_{Imb}[ImCa] \\ & - k_{Bf}[B][Ca^{2+}] - k_{Ef}[E][Ca^{2+}] - k_{Imf}[Im][Ca^{2+}] \\ & + \beta([Ca_0^{2+}] - [Ca^{2+}]) \end{aligned} \quad (2.1)$$

$$\frac{d[BCa]}{dt} = k_{Bf}[B][Ca^{2+}] - k_{Bb}[BCa] + r[BCa^*] - \eta[BCa] \quad (2.2)$$

$$\frac{d[ECa]}{dt} = k_{Ef}[E][Ca^{2+}] - k_{Eb}[ECa] \quad (2.3)$$

$$\frac{d[ImCa]}{dt} = k_{Imf}[Im][Ca^{2+}] - k_{Imb}[ImCa] \quad (2.4)$$

$$\frac{d[BCa^*]}{dt} = \eta[BCa] - r[BCa^*] \quad (2.5)$$

754 where $[Ca_0^{2+}]$ is the baseline calcium concentration within the cell soma, β is a rate defining
755 how quickly free calcium enters or leaves the cell in the absence of an action potential, η is
756 the excitation rate for indicator bound calcium, r is the photon release rate for the excited
757 indicator bound calcium, and f and b are used to indicate the forward and backward rates
758 for chemical reactions respectively. The excitation rate defines the proportion of indicator
759 bound calcium that becomes excited at each time step. The photon release rate defines the
760 proportion of excited indicator bound calcium that releases a photon and returns to its relaxed
761 state at each time step. An action potential is modelled as a discontinuous increase in the free
762 calcium concentration to an appropriate value (Maravall et al., 2000).

763 Note that each of the three pairs of binding and unbinding terms in the first equation has a
764 corresponding pair in one of the subsequent three equations. Binding removes a free calcium
765 molecule and adds a bound calcium molecule, and unbinding does the opposite.

766 When using this model to simulate a fluorescence trace, the system of equations above are
767 first solved over a period of 25s without action potentials. This lets each of the five tracked
768 chemical concentrations reach their steady state. Then we use the given spike train and the
769 parameters to model the fluorescence trace.

770 Photon release & capture

771 We used a simple model for the photon release. The number of photons released at each time
772 step was controlled by the number of excited indicator bound calcium molecules in the cell

2.2. Methods

773 and a parameter called the ‘release rate’. The release rate is an optimised free parameter of
774 the model.

775 As for the photon capture, in two-photon excitation microscopy the photons scattered
776 by the fluorescent indicator get scattered in all directions. Therefore the number of photons
777 detected is stochastic. This made the process for capturing photons the natural source of
778 noise in the system. The number of photons captured, and therefore the intensity of the
779 fluorescence, is modelled using a binomial distribution. The number of photons released was
780 used as the number of trials. The probability of success, or ‘capture rate’ was a free parameter
781 of the model that we optimised.

782 2.2.2 Parameter optimisation

783 The free parameters of the model are as follows:

784 **Calcium rate, β** Controls how quickly the concentration of free calcium will be driven to
785 the baseline concentration.

786 **Capture rate, p** The average proportion of photons captured by the photon detector.

787 **Excitation rate, η** The number of indicator bound calcium molecules that become excited
788 by photon bombardment at each time step.

789 **Release rate, r** The number of excited indicator bound calcium molecules that release a
790 photon at each time step.

791 To optimise the free parameters given a fluorescence trace, we applied the following proce-
792 dure:

793 1. The frequency power spectrum of the trace was measured.

794 2. The power spectrum was smoothed using a boxcar smoother (aka. sliding average, box
795 smoother).

796 3. The log of the smoothed power spectrum was measured.

797 4. Use the model to create a modelled fluorescence trace.

798 5. Apply steps 1, 2, and 3 to the modelled fluorescence trace.

799 6. Calculate the root mean squared difference between the log power of the actual fluo-
800 rescence trace, and the log power of the modelled fluorescence trace.

801 7. Calculate the root mean squared difference between the actual fluorescence trace and
802 the modelled fluorescence trace.

803 8. Use an optimisation algorithm to reapply this process, attempting to minimize the sum
804 of the two root mean squared differences at each iteration.

805 Using the root mean squared difference of the log power spectra as part of the objective
806 function forces the model to match the noise frequency of the actual fluorescence. Using
807 the root mean squared difference of the traces themselves forces the model to match the
808 amplitude of the fluorescence trace more accurately. Using both of these terms as part of our
809 objective function was designed to make our model match the change in $\Delta F / F_0$ in response
810 to an action potential as well as the signal-to-noise ratio of the the actual fluorescence trace.
811 We weighted both of these terms equally.

812 In order to minimise the objective function, a suite of meta-heuristic optimisation (aka.
813 black-box optimisation) algorithms were implemented on each of the traces in the dataset.
814 These methods were chosen because they don't require a gradient for the objective function
815 (gradient-free) and they are particularly useful for minimising stochastic objective functions
816 like the one we used here. The free parameters were optimised for each individual fluores-
817 cence trace. The most successful method for each trace was recorded. The method that was
818 most often successful was probabilistic descent, and the second most successful method was
819 generating set search. Both of these methods are examples of pattern search. These two
820 methods were the best optimisers on about 75% of the traces in the dataset. The other meth-
821 ods were differential evolution (with and without radius limited sampling, adaptive and not
822 adaptive), natural evolution strategy, and random search for comparison.

823 Although this optimisation procedure minimises the value of the optimisation function,
824 the value never reaches zero for a number of reasons. Firstly, the fluorescence traces carry
825 low frequency fluctuations that cannot be captured by the model. Secondly, the model as-
826 sumes that the process of calcium binding to the fluorescent indicator is linear in time (see
827 equation 1), but there are more complicated dynamics involved here. Fluorescent calcium
828 indicators, the GCaMP series for example, are often built upon the calcium binding protein
829 called 'calmodulin'. This protein has four calcium binding sites. These sites are locally split
830 into two pairs. Each pair has a different affinity for calcium, and the affinity of the binding
831 sites is affected by the occupancy of the other binding sites (Kilhoffer et al., 1992). So the
832 calcium to calcium indicator binding process is non-linear, but the model does not take this
833 into account.

2.2. Methods

Parameter	Description	Value	Source
baseline	The baseline concentration of free calcium within the cell soma	$4.5 \times 10^{-8} \text{M}$	(Maravall et al., 2000)
cell radius	The radius of the soma (assumed to be spherical)	10^{-5}M	(Fiala and Harris, 1999)
endogenous	The concentration of endogenous mobile buffer within the cell soma	10^{-4}M	(Faas et al., 2011)
frequency	The frequency at which the spike trains are sampled.	100Hz	
immobile	The concentration of endogenous immobile buffer within the cell soma	$7.87 \times 10^{-5} \text{M}$	(Bartol et al., 2015)
indicator	The concentration of fluorescent indicator within the cell soma	10^{-4}M	(Maravall et al., 2000)
k_{Bb}	The unbinding rate of the fluorescent calcium indicator	160s^{-1}	(Bartol et al., 2015)
k_{Bf}	The binding rate of the fluorescent calcium indicator	$7.77 \times 10^8 \text{s}^{-1} \text{M}^{-1}$	(Bartol et al., 2015)
k_{Eb}	The unbinding rate of the endogenous mobile buffer	10^4s^{-1}	(Bartol et al., 2015)
k_{ef}	The binding rate of the endogenous mobile buffer	$10^8 \text{s}^{-1} \text{M}^{-1}$	(Bartol et al., 2015)
k_{Imb}	The unbinding rate of the endogenous immobile buffer	524s^{-1}	(Bartol et al., 2015)
k_{Imf}	The binding rate of the endogenous immobile buffer	$2.47 \times 10^8 \text{s}^{-1} \text{M}^{-1}$	(Bartol et al., 2015)
peak	The increase in free calcium concentration within the cell induced by an action potential	$2.9 \times 10^{-7} \text{M}$	(Maravall et al., 2000)

TABLE 2.1: **Fixed parameters** A table of the parameters fixed before optimising the model. The values of these parameters could be changed to model different fluorescent calcium indicators.

834 **Fixed parameters**

835 As well as the optimised parameters mentioned in section 2.2.2, the model also has thirteen
 836 fixed parameters. Please see table 2.1 for details of these parameters and their values. In
 837 an application of the model, these parameters can be changed in order to model any given
 838 fluorescent calcium indicator, or even prospective indicators that only exist in theory.

839 **2.2.3 Julia**

840 The programming language used to write and execute the model was ‘Julia’. Julia is a dy-
 841 namic programming language designed for technical computing. Julia was designed specif-
 842 ically to provide a convenient high-level dynamic language similar to MATLAB, or Python,
 843 with improved performance. Julia’s type system and Julia’s direct interfaces with C and

844 Fortran allow this aim to be achieved (Bezanson et al., 2012). The Julia version of the
845 ‘Sundials’ package for ODE solving was used to solve the system of equations above. The
846 BlackBoxOptim.jl package for Julia was used to perform the optimisation.

847 **2.2.4 Spike inference**

848 We used spike inference algorithms to compare the quality of spike inference using the mod-
849 elled traces to the quality of spike inference using the observed traces. We also used the
850 spike inference algorithms to assess the effect of parameter perturbation on the spike infer-
851 ence. Three algorithms were used:

852 **Constrained non-negative matrix deconvolution algorithm (aka CNMD algorithm)** The
853 underlying model models the fluorescence as a linear function of a calcium trace with
854 additional noise. This calcium trace is a first order autoregression with a pulse input to
855 represent action potentials. This algorithm uses a constrained version of non-negative
856 Weiner deconvolution to infer a calcium signal and a ‘spiking activity signal’ from the
857 fluorescence trace (Vogelstein et al., 2010; Pnevmatikakis et al., 2016). The spiking ac-
858 tivity signal is a non-negative vector of real numbers reflecting the cell’s activity rather
859 than an actual spike train. We inferred a spike train by choosing an optimised thresh-
860 old for the spiking activity signal. Whenever the spiking activity signal exceeded that
861 threshold, an action potential was inferred. The threshold was optimised by minimis-
862 ing the difference between the number of spikes observed and the number of spikes
863 predicted.

864 **MLSpike algorithm** Deneux et al. (2016) developed two different calcium fluorescence
865 models behind their spike inference algorithm (MLspike) with a more biological in-
866 spiration. For their simpler model, they take a physiological approach and account for
867 baseline calcium indicator dynamics. They end up with a system of first order differen-
868 tial equations defining the dynamics of calcium concentration, baseline fluorescence,
869 and fluorescence. For their more complicated model specifically for genetically en-
870 coded calcium indicators, they also took into account indicator binding and unbinding
871 rates, which added another equation to their system of equations. This algorithm uses a
872 generalised version of the Viterbi algorithm to return the spike train that maximises the
873 likelihood of producing the given fluorescence trace. The Viterbi algorithm is an algo-
874 rithm for estimating the most likely sequence of hidden states resulting in a sequence
875 of observed states in a discrete-time finite-state Markov process (Forney, 1973). In this

2.2. Methods

876 case, each hidden state is defined by the presence or absence of an action potential, and
877 each observed state is the value of the fluorescence trace at each time step. (Deneux
878 et al., 2016).

879 **Online Active Set method to Infer Spikes (OASIS)** This algorithm is once again based on
880 an auto-regressive model of the fluorescence trace, but can be generalised to any or-
881 der. Both the first and second order versions can be fit to a spike train in a reasonable
882 time. The algorithm itself is a generalisation of the pool adjacent violators algorithm
883 (PAVA) that is used in isotonic regression. The OASIS algorithm works through the
884 fluorescence trace from beginning to end, this combined with the speed of the algo-
885 rithm means that it could be used for real-time online spike inference (Friedrich and
886 Paninski, 2016). Given a fluorescence trace, the algorithm will return the most likely
887 spike train and an inferred denoised fluorescence signal.

888 In order to quantify the quality of spike inference for a given algorithm, we ran that algorithm
889 on all of the fluorescence traces in dataset number eight of the spike finder datasets. These
890 datasets contained fluorescence traces from neurons containing a fluorescent calcium indicator
891 (either OGB-1 or GCaMP6s) and spike trains from those cells simultaneously recorded using
892 loose-patch electrophysiological recordings. This provided us with a *ground-truth* for spike
893 inference from the fluorescence traces. Then we measured some binary classification measures
894 on the results. These measures included

- 895 ● Accuracy
- 896 ● True positive rate (aka recall, sensitivity, hit rate)
- 897 ● True negative rate (aka specificity)
- 898 ● Precision
- 899 ● Negative predicted value
- 900 ● False negative rate (aka miss rate)
- 901 ● False positive rate (aka fall-out)
- 902 ● False discovery rate
- 903 ● False omission rate

904 In making these measurements, we allowed a tolerance of two subsequent time bins for spike
905 prediction. For example, the spike train data is a vector of 0s and 1s, with one element
906 for each time bin, and time bin being 10ms. A ‘0’ denotes inactivity, a ‘1’ denotes the
907 presence of at least one action potential. The inferred spike trains produced by the spike
908 inference algorithms take the same form. In our analysis, if a spike appeared in the inferred
909 spike train up to two time frames after a spike in the observed spike train, that spike was
910 considered correctly inferred i.e. a true positive. However, once a spike in the inferred
911 spike train was matched to a spike from the observed spike train, the inferred spike could
912 not be matched to another observed spike. To illustrate, if two spikes were inferred in the
913 two time bins following an isolated observed spike, the first inferred spike was considered
914 correctly inferred, but the second inferred spike was considered incorrectly inferred, i.e. a
915 false positive.

916 The most useful measure was the true positive rate. This is because the spiking is sparse
917 and this measurement is sensitive to the number of spikes observed and inferred, but is not
918 affected by the true negative or false negative rates. After optimising the parameters for each
919 fluorescence trace we measured the spike inference quality for the observed fluorescence
920 traces, and compared this to the spike inference quality for the modelled traces.

921 When measuring the spike inference quality for higher frequency spike train (1 – 10Hz),
922 we used the accuracy as our binary classification measure. At these frequencies the variance
923 of the fluorescence trace was much higher than for sparser spiking regimes, therefore we
924 wanted to take into account the number of false negatives inferred by the algorithm.

925 Comparing spike inference quality

926 In order to compare spike inference quality we had to use methods for comparing samples.
927 When comparing the true positive rate distributions arising from two different datasets, or
928 two different algorithms on the same dataset, we compared the distributions using a paired
929 t-test.

930 2.2.5 Perturbation analysis

931 In order to measure the sensitivity of spike inference to changes in a given model parameter,
932 we perturbed the parameter and compared the quality of spike inference with the perturbed
933 parameters to the quality of spike inference with the experimental or optimised parameters.
934 In order to maximise the possibility of observing a difference due to the perturbation, we

2.3. Results

935 perturbed the chosen parameter by a relatively large amount. For example, the experimen-
936 tal value for the molar concentration of the fluorescent indicator within the cell was 10^{-4}M
937 (Maravall et al., 2000). The perturbed values used for this parameter were 10^{-2}M , 10^{-3}M ,
938 10^{-5}M , and 10^{-6}M . The quality of the inference was compared by measuring the true posi-
939 tive rate for each perturbed value and using a t-test to compare the distributions of the results.

940 **2.2.6 Signal-to-noise ratio**

941 To assess the effect of perturbation on the modelled traces, we measured and compared the
942 signal to noise ratio (SNR) on each of the modelled traces. We calculated the SNR as the
943 peak change in fluorescence divided by the standard deviation of the baseline fluctuation of
944 the fluorescence trace (Tada et al., 2014). We measured these values by running the model
945 on a spike train consisting a long period of inactivity followed by one action potential. We
946 ran the model on this spike train one hundred times. We then measured the mean change
947 in fluorescence and standard deviation of baseline activity across the one hundred modelled
948 fluorescence traces, and calculated the SNR.

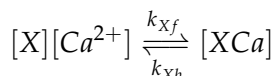
949 **2.2.7 Data sources**

950 All of the data used in this project was sourced from the ‘Spike Finder’ project
951 (spikefinder.codeneuro.org). The data consisted of a collection of datasets with simultane-
952 ously measured fluorescence traces and action potentials (Berens et al., 2018).

953 **2.3 Results**

954 **2.3.1 A biophysical computational model can generate accurate fluorescence
955 traces from spike trains**

To study the relationship between action potential firing and calcium fluorescence, we built a computational model of calcium dynamics in a neuronal soma. The model consisted of four dynamic variables: the concentration of free calcium, two types of endogenous buffer, and the calcium-sensitive fluorescent indicator. Each of the buffers and the indicator could independently bind and unbind with calcium. These reactions were modelled as



where X is the buffer concentration and Ca^{2+} is the calcium concentration. Each species could therefore exist in two states: either bound with calcium or unbound. To model the imaging process, we also added a third, excited state to the indicator. When in the calcium-bound state, the indicator could be converted to an excited state, corresponding to the absorption of a photon. The rate of this excitation process could be interpreted as the intensity of the light illuminating the sample. Once excited, the species decayed back to the unexcited state at a fixed rate, corresponding to the spontaneous emission of photons. The total emitted fluorescence signal was interpreted as proportional to this de-excitation flux. To represent experimental noise in the photon capture process, we drew a random number of captured photons at each time step from a binomial distribution, parameterised by a number p that corresponds to the mean fraction of released photons that are captured.

The model had 17 parameters in total describing the molecules' concentrations and reaction rates (Methods). We set 13 of these parameters to values from the literature. The remaining 4 parameter values we fit to publicly-available data (Berens et al., 2018), briefly explained as follows (see Methods for full details). Single neurons from acute rat cortical slices expressing GCaMP6s were imaged with two-photon microscopy while the membrane potentials of the somata of the same neurons were simultaneously recorded via whole-cell patch clamp electrophysiology. In this dataset, the electrical recordings give unambiguous information about neurons' spike times. To do the parameter fitting, we feed these spike trains as inputs to the computational model. After running, the model returns a simulated fluorescence trace. We aimed to find the model parameter values that give the best match between this simulated fluorescence trace and the real fluorescence time series recorded in the corresponding neuron. To do this we used a suite of optimisation procedures to jointly fit both the real neuron's fluorescence time series and power spectrum, which capture complementary information about the spikes-to-fluorescence mapping (Methods). We performed the fitting procedure independently for each of the 20 neurons in the spikefinder dataset (<http://spikefinder.org>). After fitting, the model produced realistic-looking fluorescence time series (Figure 2.1).

Given that fluorescence traces are often modelled using a linear combination of a first degree autoregressive process and white noise, it could be argued that a four parameter model contains some redundancy in the parameter space. But, our aim was to create a biophysical model that could be useful for interpreting the role of cell dynamics behind the production of the fluorescence trace. Because of that we felt that our redundancy was justified.

2.3. Results

2.3.2 Spike inference algorithms perform similarly on real data compared with time series simulated from the model

Researchers often pass the fluorescence time series through a spike inference tool before performing further statistical analyses. These spike inference algorithms take the fluorescence trace as input and attempt to estimate the neuronal spike train that triggered them (Vogelstein et al., 2010; Pnevmatikakis et al., 2016; Friedrich and Paninski, 2016; Pnevmatikakis et al., 2013; Pnevmatikakis et al., 2014; Deneux et al., 2016). Part of our motivation for building this model was to allow us to investigate which properties of the cell and the calcium indicator affect the quality of spike inference? In order to trust the conclusions from our model, we should first be confident that spike inference from our simulated fluorescence traces is similar to that from the real data. To test this we passed each of the simulated fluorescence traces through three previously published spike inference algorithms, quantified their performance against the ground-truth electrophysiology data, repeated the procedure for the real calcium fluorescence time series, and compared the accuracy of the inference processes in all cases. The *true positive rate*, also known as the *recall*, the *sensitivity*, or the *probability of detection* of spike inference varied across the three inference algorithms we tried (p value and statistical test here). The constrained non-negative matrix deconvolution algorithm (Pnevmatikakis et al., 2016) (CNMD algorithm) correctly detected approximately 45% of the true spikes, the OASIS algorithm (Friedrich and Paninski, 2016) correctly detected approximately 35% of the true spikes, and the ML spike algorithm (Deneux et al., 2016) correctly detected approximately 15% of the true spikes (see figure 2.2). Notably, for two of the three inference algorithms, the quality of inference was also fairly consistent for individual spike trains, not just the group means ($p > 0.05$, paired t-test). This demonstrates that the models were generating fluorescence time series that were similarly difficult to decode as the real data, in ways that were not specific to any one inference algorithm. This is evidence that the models captured real aspects of the spikes-to-fluorescence transform.

2.3.3 Relative effects of various buffers to the fluorescence signal

One of the benefits of computational models over laboratory experiments is that we can observe all the variables in the simulation to gain insight into the system's dynamics, which can be difficult to do in the lab. We plotted the concentrations of the various species over time for a version of the model fit to one data set, in response to the same train of spikes used for fitting (figure 2.3). Figure 2.3a shows the absolute values of the species concentrations,

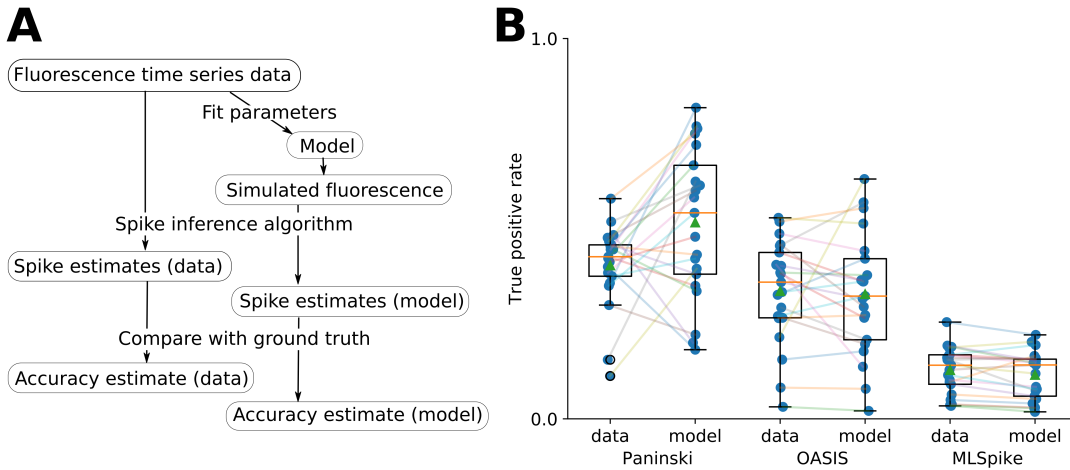


FIGURE 2.2:
A: Workflow to compare spike inference for real versus simulated fluorescence data.

B: True positive rates achieved by three different spike inference algorithms when applied to observed spike trains, and simulated spike trains. Data points overlaid as blue circles. The performance is similar from real and simulated data for each of the algorithms.

quantities

1021 summed. Consistent with experimental estimates (Maravall et al., 2000), only a small fraction
 1022 ($\sim 0.1\%$) of calcium is free and unbound to any buffer. Of the bound calcium, the vast
 1023 majority, ($\sim 96\%$) is bound to the GCaMP indicator. The two types of endogenous buffer
 1024 are bound to the remaining calcium ($\sim 4\%$). An influx of calcium from a single spike adds
 1025 very little to the total calcium, in relative terms (red line in Figure 3a).

1026 When calcium entered the model neuron it was rapidly buffered (Bartol et al., 2015).
 1027 However the relative fractions of which buffer molecules bound to the influxed calcium was
 1028 dynamic, and changed over time. Figure 2.3 (b-f) shows the time course of the various species
 1029 over time in response to a calcium influx event from a single action potential. Crucially,
 1030 the indicator $[BCa]$ competed with the endogenous buffers $[ImCa]$ and $[ECa]$ – all three
 1031 bind calcium on similar timescales. This implies that the timecourse and amplitude of the
 1032 $[BCa]$ variable will also depend on the binding rates and availabilities of the endogenous
 1033 buffers. For example if we decreased the concentration of an endogenous buffer, we might
 1034 expect both a faster rise time and greater peak amplitude of the $[BCa]$ signal in response to
 1035 a calcium influx event. The slowest component of the decay had a similar time constant for
 1036 $[BCa]$, $[ImCa]$ and $[ECa]$, which in turn matched the $[Ca]$ extrusion time constant in our
 1037 model ($\sim 6.29 \times 10^{-22} \text{Ms}^{-1}$). This implies that the buffers and the indicator had reached
 1038 a dynamic equilibrium and were jointly tracking the free calcium concentration as calcium
 1039 was slowly extruded from the cell.

2.3. Results

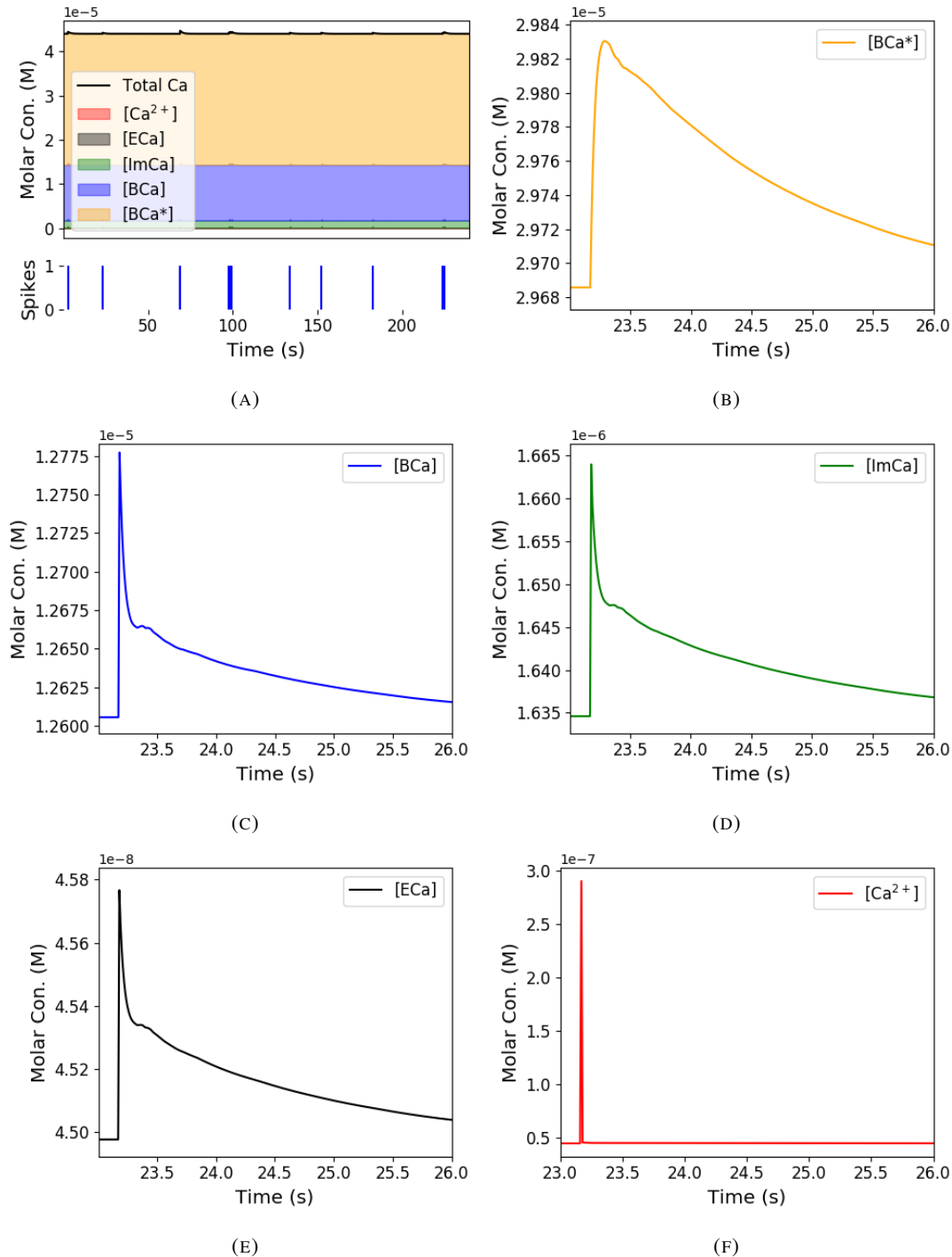


FIGURE 2.3: Calcium Buffering Dynamics (A) The proportions of bound and free calcium concentrations within a cell, with the associated spike train. (B)-(F) The dynamics of the concentration of (B) excited indicator bound calcium, (C) indicator bound calcium, (D) immobile endogenous buffer bound calcium, (E) mobile endogenous buffer bound calcium, and (F) free calcium in response to an action potential at ~ 23.2 s.

1040 Interestingly the excited bound calcium species ($[BCa^*]$) showed a qualitatively different
1041 timecourse in response to a calcium influx event. This concentration is subject to the added
1042 ‘excitation and release’ dynamic, where a certain proportion of the concentration absorbs the
1043 energy from an incoming photon and goes into an ‘excited state’ at each time step. A certain
1044 proportion of the concentration releases a photon and reverts to a ‘relaxed state’ at each
1045 timestep also. This means that the excited bound calcium lags behind the bound calcium
1046 trace. We could think of the excited bound calcium trace as a low pass filtered version of the
1047 bound calcium trace.

1048 **2.3.4 Spike inference accuracy is sensitive to indicator properties, and likely
1049 varies within and between cells**

1050 The above results imply that the fluorescence signal depends on the relative properties of
1051 both GCaMP and the endogenous buffers. We next used the model to directly ask how
1052 sensitive spike inference was to these components. We focused on three key parameters that
1053 likely vary from cell to cell and experiment to experiment: GCaMP binding kinetics, GCaMP
1054 concentration, and endogenous buffer concentration.

1055 Several variants of GCaMP itself have been made that differ in calcium binding kinetics,
1056 baseline fluorescence, fluorescence efficiency, and other factors. For example, GCaMP6f has
1057 a decay time constant of $\sim 1\text{s}$, while GCaMP6s has a decay time constant of $\sim 2\text{s}$ (Chen
1058 et al., 2013). Here we asked how these differences in binding kinetics affect spike inference.
1059 We jointly varied the calcium binding and unbinding rates of the indicator by the same factor
1060 over a range from 100-fold slower to 100-fold faster from the fitted values, and simulated the
1061 fluorescence response for each of the parameter settings in response to the same spike trains
1062 as before (figure 2.4). Notably this manipulation does not affect the indicators affinity, and
1063 therefore would not affect steady-state responses to prolonged changes in calcium. Instead
1064 it is likely to affect its sensitivity to the spike train dynamics. We computed two summary
1065 measures from the simulated fluorescence traces: the signal-to-noise ratio for a single spike
1066 (Methods, section 2.2.6), and the accuracy of spike inference for each of the spike trains. We
1067 observed a reduction in the signal-to-noise ratio and the spike inference quality when we set
1068 the binding and unbinding rates were set to one hundredth of their fitted values, and to one
1069 tenth of their fitted values. When we increased the value of both binding rates, we observed
1070 no change in these measurements. The reduction in both rates lead to smaller increases in
1071 fluorescence in response to an action potential and a longer decay time (figure 2.4a), this
1072 caused the reduction in signal-to-noise ratio. As both rates were increased, the change in

2.3. Results

1073 $\Delta F/F_0$ in response to an action potential increased and the decay time decreased slightly,
1074 but the fluorescence trace created by these values was very similar to the trace created by the
1075 fitted values.

1076 Second, the overall concentrations of GCaMP often varies from cell to cell. For exam-
1077 ple different cells, even of the same type in the same tissue, can express different levels of
1078 GCaMP, due to proximity to the infection site, or the cell becoming ‘nuclear-filled’ (Tian et
1079 al., 2009; Chen et al., 2013). Also, GCaMP is often used for longitudinal experiments where
1080 the same cells are re-imaged across multiple days or weeks. However since GCaMP expres-
1081 sion typically ramps up over time (Chen et al., 2013), the accuracy of spike inference may
1082 differ across multiple longitudinal recordings in the same cell. We addressed this by varying
1083 the concentration of calcium indicator in the model, simulating spike trains and measuring
1084 signal-to-noise ratio and spike inference accuracy on the resulting fluorescence traces. Both
1085 increasing and decreasing the concentration of the indicator had effects on the fluorescence
1086 trace, signal-to-noise ratio, and spike inference. The signal-to-noise ratio and spike inference
1087 quality decreased with decreased indicator concentration, and both showed a decrease when
1088 the indicator concentration was increased to 100 times its fitted value (figure 2.5). The signal-
1089 to-noise ratio showed an increase when the indicator concentration was increased to 10 times
1090 its fitted value, but there was no corresponding change in the spike inference quality. The
1091 decrease in indicator concentration caused a reduction in the increase in $\Delta F/F_0$ in response
1092 to an action potential, and an increase in the decay time of this increase (figure 2.5a). The
1093 increase in indicator concentration had the opposite effect, it caused an increase in the change
1094 in $\Delta F/F_0$ in response to an action potential, and a decrease in the decay time.

1095 Third, the concentration and types of endogenous calcium buffers also vary from neuron
1096 to neuron, both within and between cell types (Bartol et al., 2015; Maravall et al., 2000;
1097 Neher and Augustine, 1992). Since the calcium buffer capacity of neurons is high, around
1098 50-70 (Lee et al., 2000) in excitatory hippocampal pyramidal cells, around 100-250 (Lee et
1099 al., 2000) in inhibitory hippocampal pyramidal cells, and 900-200 in Purkinje cells (depend-
1100 ing on the age of the subject), these endogenous buffers compete with GCaMP for binding
1101 to calcium, and variations in endogenous buffer concentration may affect GCaMP signal and
1102 therefore spike inference. To address this we varied the concentration of the endogenous
1103 buffer in the model neuron over five orders of magnitude from 0.8 to 8000 μM , simulated
1104 calcium fluorescence traces in response to the same set of spike trains, and performed spike
1105 inference on the resulting fluorescence time series. Increasing the endogenous buffer con-
1106 centration had a substantial effect on the GCaMP fluorescence signal, both decreasing its

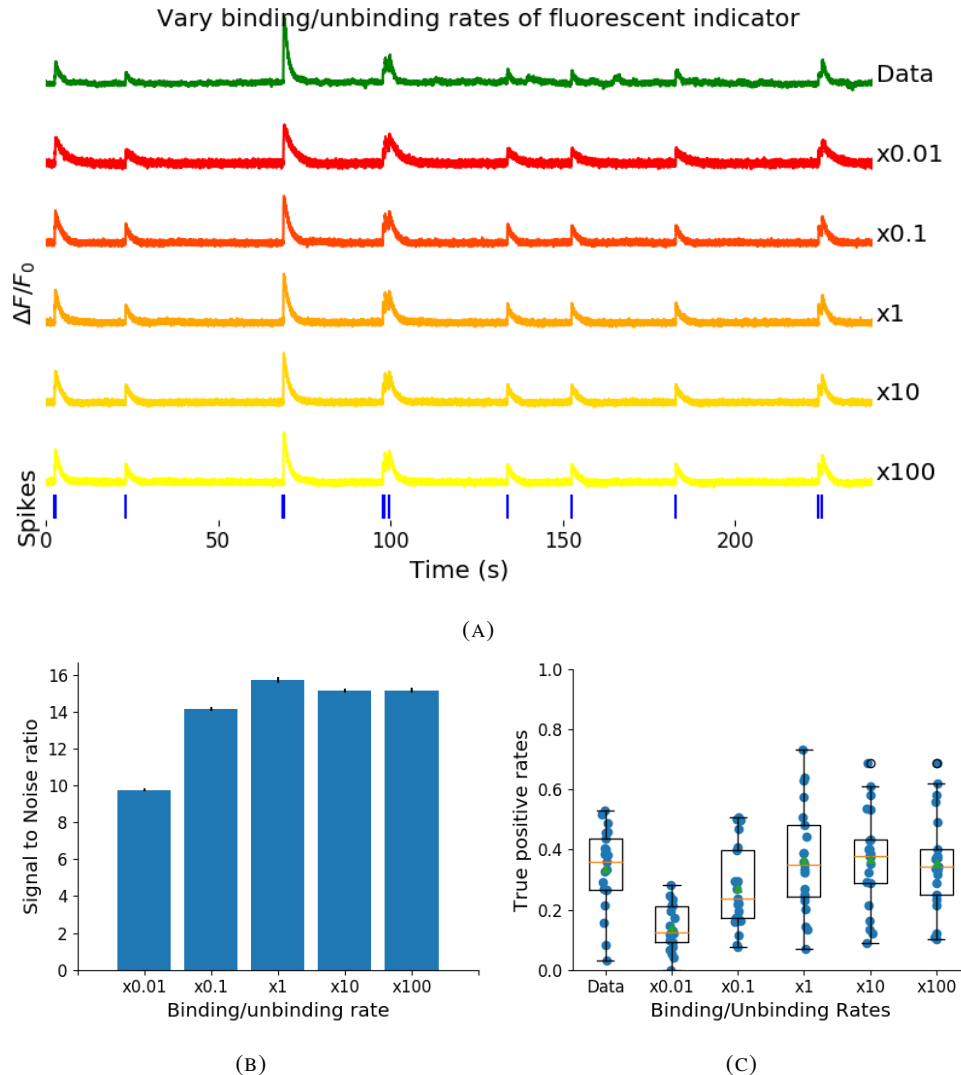


FIGURE 2.4: (A) An example trace for each of the five pairs of values used for the binding and unbinding rates of the fluorescent calcium indicator. (B) The signal-to-noise ratio of the modelled fluorescence traces using each of the four perturbed value pairs, and the experimental value. The SNRs for the value pairs perturbed downward are lower than that for the unperturbed value pair or the higher value pairs. (C) The true-positive rates of the deconvolution algorithm's predictions when inferring from the observed data, and inferring from modelled traces using the perturbed and experimental values. We used the CNMF algorithm for spike inference here. The results from the other spike inference methods were similar, with their true positive rates scales similarly to figure 2.2 B.

2.3. Results

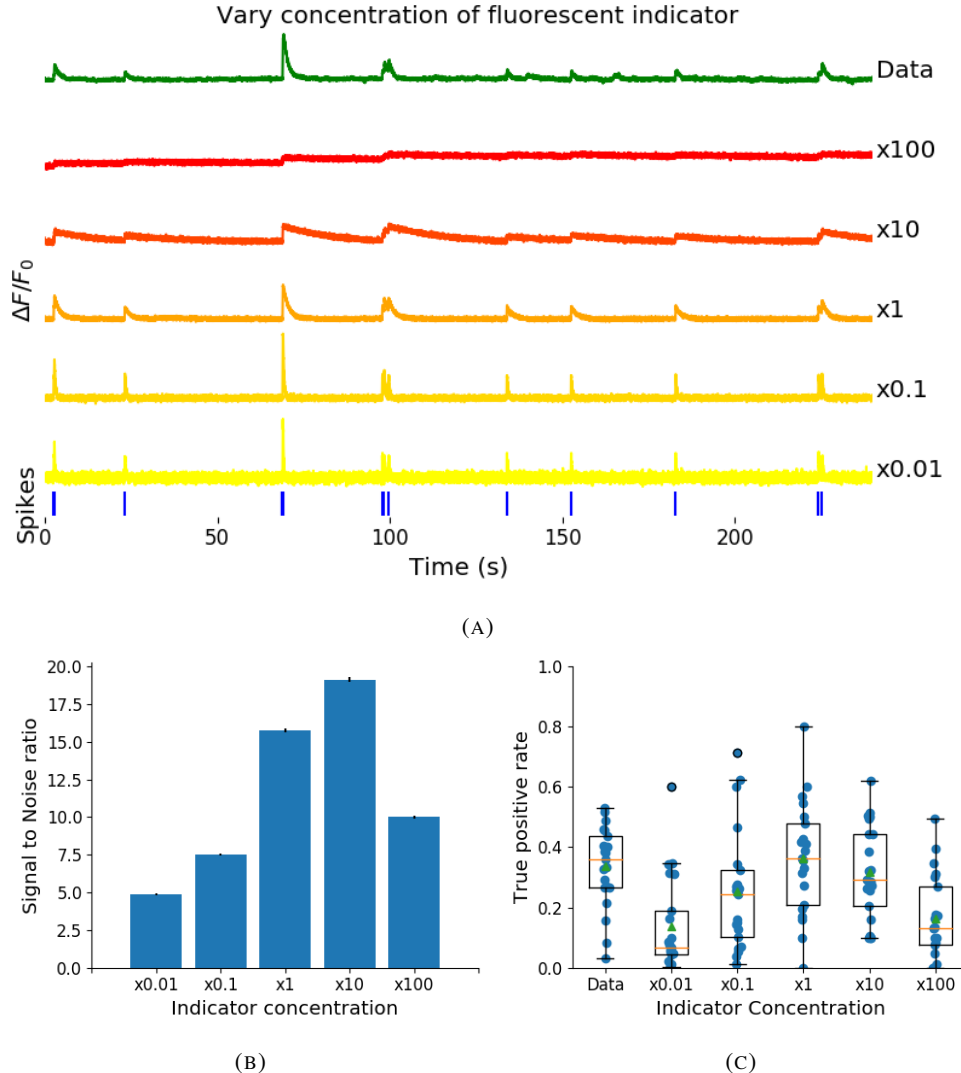


FIGURE 2.5: (A) An example trace for each of the five perturbed values for the concentration of fluorescent calcium indicator. The top two traces are produced by the lower perturbed values, the middle trace is produced by the experimental value, and the lowest two traces are produced when using the higher perturbed values. (B) The signal-to-noise ratio of the modelled fluorescence traces using each of the four perturbed values, and the experimental value. Extreme perturbations of the concentration either above or below the experimental level lowered the SNR. (C) The true-positive rates of the deconvolution algorithm's predictions when inferring from the observed data, and inferring from modelled traces using the perturbed and experimental values. We found that the algorithms performs equally badly on the two most extreme values, and performs equally well on the experimental value, and the next higher perturbed value. We used the CNMF algorithm for spike inference here. The results from the other spike inference methods were similar, with their true positive rates scales similarly to figure 2.2 B.

1107 amplitude and slowing its kinetics (figure 2.6(a)). This corresponded with a decrease in both
1108 single-spike signal-to-noise ratio (figure 2.6(b)) and spike inference accuracy (figure 2.6(c)).
1109 In contrast, decreasing endogenous buffer capacity from the fitted value had little effect on
1110 either the GCaMP signal or spike inference (figure 2.6).

1111 **2.3.5 Single spike inference accuracy drops for high firing rates, but firing rate
1112 itself can be estimated from mean fluorescence amplitude**

1113 The fluorescence signal recorded from neurons using calcium indicators is typically much
1114 slower than changes in membrane potential for two reasons: first, because the calcium and
1115 the indicator have slow binding and unbinding kinetics, the signal is a low-pass filtered ver-
1116 sion of the membrane potential. Second, neuronal two-photon imaging experiments are often
1117 performed in scanning mode, which limits their frame rate to $\sim 10\text{Hz}$ or slower. This im-
1118 plies that multiple spike events that occur close in time might be difficult to resolve from a
1119 calcium indicator time series. Many cells, especially several types of inhibitory interneurons,
1120 fire tonically at rates higher than 10Hz. We used the model to test whether spike inference
1121 accuracy depended on the neuron's firing frequency by driving the cell with spike trains sam-
1122 pled from a Poisson processes of varying frequency. We simulated a variable firing rate using
1123 an Ornstein-Uhlenbeck process, and simulated the spike trains using a Poisson distribution
1124 with its rate taken from this process. Because of the high frequency firing rate of these spike
1125 trains, we using the accuracy as the measure of spike inference quality. We simulated 30
1126 spike trains at average firing rate of 1, 5, and 10Hz, and measured the spike inference quality
1127 of all these traces. Spike inference accuracy decreased with increasing firing rate, for up to
1128 10Hz Poisson spike trains (figure 2.8(left)). Although the accuracy remained above 90% for
1129 each of the three frequencies. We also plotted the average $\Delta F / F_0$ as a function of stimula-
1130 tion firing rate. We found that it increased monotonically as a function of firing rate (figure
1131 2.8(right)).

1132 We expected lower spike inference quality as the average spiking frequency increased.
1133 Since the fluorescence trace, in some sense, is a low pass filtered version of the spike train, a
1134 tightly packed groups of spikes will be more difficult to infer than isolated spikes. However,
1135 the increasing amplitude of the fluorescence trace with increasing frequency suggests that
1136 some spike inference algorithm could be developed based on this amplitude.

2.3. Results

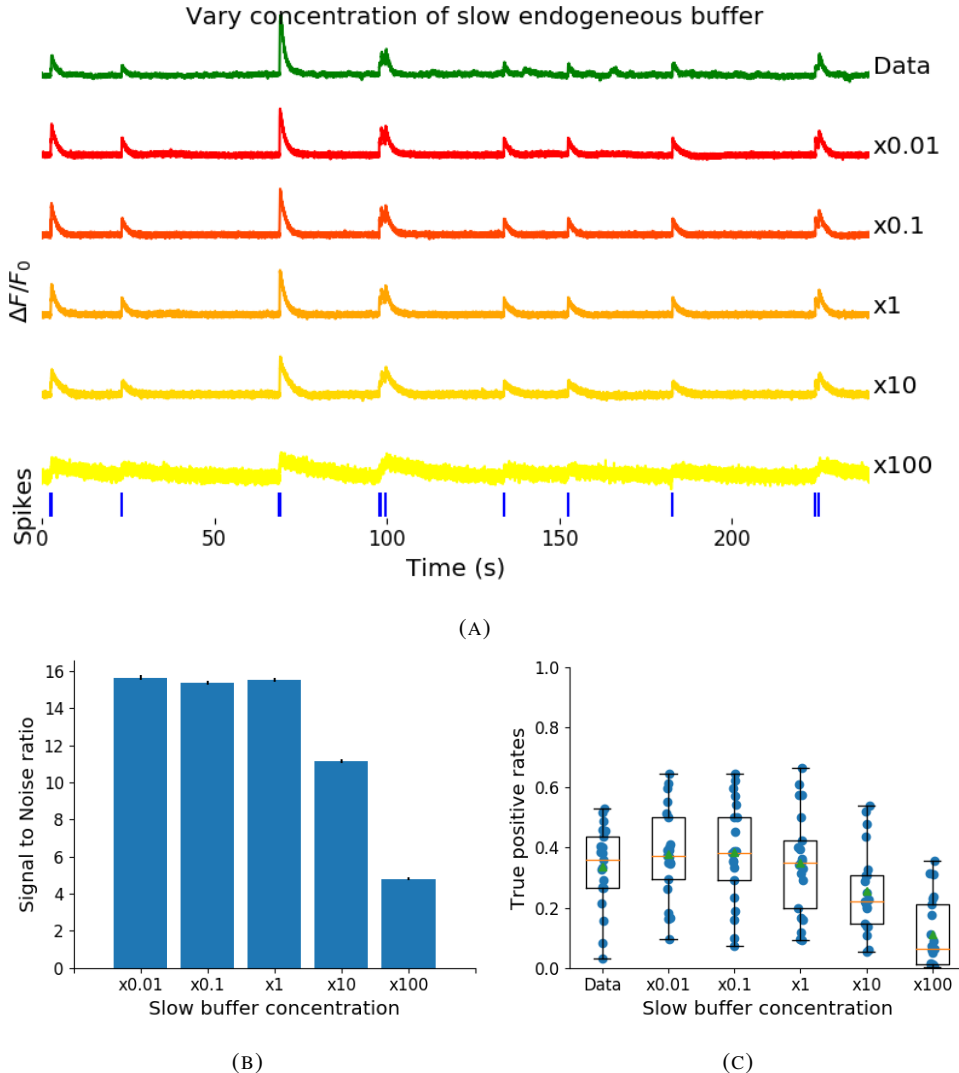


FIGURE 2.6: (A) An example trace for each of the five perturbed values for the concentration of immobile endogenous buffer. (B) The signal-to-noise ratio of the modelled fluorescence traces using each of the four perturbed values, and the experimental value. The lower values for the immobile buffer produce the same SNR as the experimental value. But the higher perturbed values produce fluorescence traces with a lower SNR. (C) The true-positive rates of the deconvolution algorithm's predictions when inferring from the observed data, and inferring from modelled traces using the perturbed and experimental values. We used the CNMF algorithm for spike inference here. The results from the other spike inference methods were similar, with their true positive rates scales similarly to figure 2.2 B.

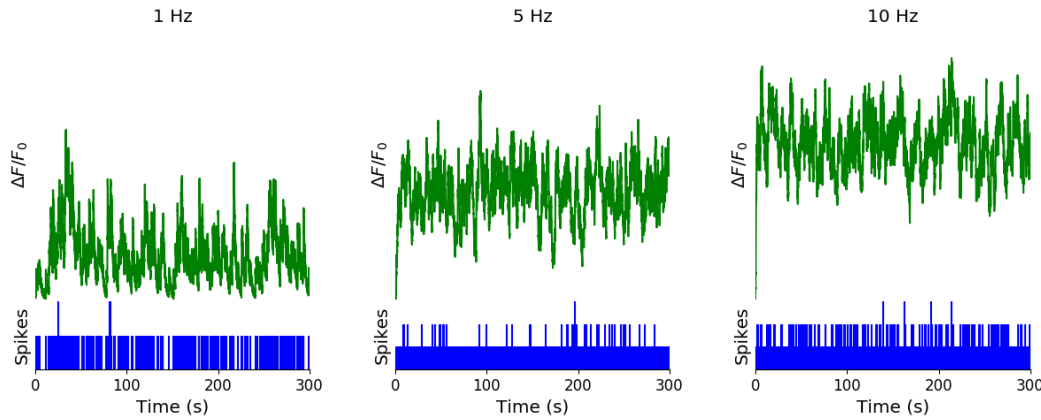


FIGURE 2.7: Simulating fluorescence traces at different firing rates Example modelled traces created using simulated spike trains with a mean firing rate of 1Hz (left column), 5Hz (middle column), and 10Hz (right column). Note the difference in amplitude with different mean firing rates.

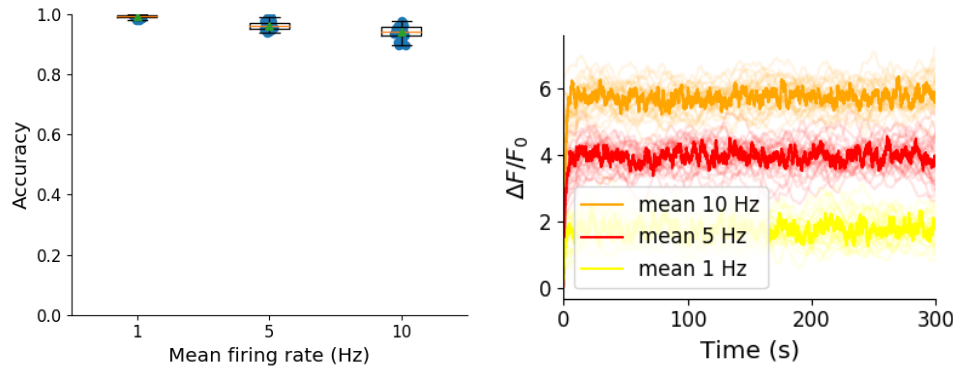


FIGURE 2.8: Inference quality and $\Delta F/F_0$ vs Firing rate (left) The spike inference accuracy when applied to 30 traces created using simulated spike trains with mean firing rates of 1, 5, and 10 Hz. (right) The mean $\Delta F/F_0$ across those 30 traces for each frequency.

1137 2.4 Discussion

1138 We designed a biophysical model for the changes in free calcium and bound calcium con-
 1139 centrations within a cell soma with a fluorescent calcium indicator. We used this model to
 1140 model the fluorescence trace resulting from a spike train in this cell. We fit the free parame-
 1141 ters of the model by matching the power spectrum and amplitude of fluorescence traces with
 1142 simultaneously measured spike trains. We inferred spikes from real fluorescence traces and
 1143 modelled fluorescence traces, and measured the quality of the spike inference in both cases.
 1144 We found that the spike inference quality was similar in both cases. We perturbed the concen-
 1145 tration of the calcium buffers in the model, and the binding/unbinding rates of those buffers
 1146 in the model, and measured the effect on the signal-to-noise ratio (SNR) of the modelled
 1147 fluorescence traces and the spike inference quality.

2.4. Discussion

1148 For the fluorescent calcium indicator, we found that any large perturbation away from the
1149 value taken from the literature led to a reduction in SNR, and spike inference quality. For
1150 the binding/unbinding rates, we kept the ratio of these rates constant, but altered their values
1151 in parallel. The lower values caused a reduction in SNR, and a reduction in spike inference
1152 quality. For the endogenous buffer concentration, an increase above the experimental value
1153 caused a reduction in SNR and spike inference quality.

1154 We perturbed the concentration of the indicator, the binding/unbinding rates, and the en-
1155 dogenous buffer concentration to values 100 times smaller and 100 times larger than than
1156 the value taken from the literature. Given that the indicator concentration can be controlled,
1157 at least to some extent, we thought it was worthwhile to simulate these extreme perturba-
1158 tions. For the binding/unbinding rates, such extreme values in these rates are unlikely for
1159 fluorescent calcium indicators or endogenous buffers. But these extreme perturbations are
1160 still useful for studying what kind of fluorescence trace an indicator with such extreme bind-
1161 ing/unbinding rates produce. Similarly, these extreme values in endogenous buffer are also
1162 unlikely to occur in neurons. But, using these values in our model allows us to analyse the
1163 interplay between the endogeneous buffer concentration and the fluorescence trace produced.

1164 Although the model produced visually similar time series to the real data, there were a
1165 few aspects it did not capture. First, the real data featured some low-frequency components
1166 that did not appear related to the spike events. These were not captured by the models we
1167 used in this study, but could be added in future by adding a suitable low-frequency term to
1168 the resulting time series. Second, the real data seemed to have some non-linearities not cap-
1169 tured in the model, for example the response to two nearby spikes was greater than expected
1170 from the linear sum of two single spikes. This may be due to the co-operative binding of
1171 calmodulin to calcium, which gives calmodulin a supra-linear sensitivity to calcium concen-
1172 tration (Faas et al., 2011). The non-linear dynamics of this binding have been included in a
1173 recently developed spike inference model (Greenberg et al., 2018). Our model, in contrast,
1174 behaved much more linearly but could be extended in future to include such non-linearities.
1175 Third, in the real data the fluorescence peak amplitude seemed to vary from spike to spike,
1176 even for well-isolated spike events. Recent research has shown that calcium influx due to a
1177 single action potential was quite variable in pyramidal cells, and that this variability had a
1178 effect on spike inference (Éltes et al., 2019). However in our model we assumed each spike
1179 leads to the same fixed-amplitude injection of calcium to the cell, leading to much greater
1180 regularity in fluorescence peak amplitudes. This variability could be added in future versions
1181 of the model by making the injected calcium peak a random variable. Fourth, we modelled

1182 the soma as a single compartment, but in reality there is likely a non-uniform spatial profile
1183 of calcium concentration. This may matter because some endogenous buffers might access
1184 calcium right as it influxes from the extracellular space, whereas the majority of the fluo-
1185 rescence signal is more likely coming from the bulk of the cytoplasm. Future models could
1186 attempt to model these spatial dependencies to assess whether they affect the overall spike
1187 inference procedure.

1188 The concentration of free calcium ions in the neuron cytoplasm enables calcium sig-
1189 nalling, which has a vital role in neuronal energy metabolism, and neurotransmission in
1190 neurons (Brini et al., 2014). Our model allowed us to examine to which calcium buffer the
1191 incoming free calcium ions, due to an action potential, bound. We found that around 95% of
1192 the calcium ions bound to the fluorescent calcium indicator. This suggests that the introduc-
1193 tion of the fluorescent calcium indicator has a dramatic effect on the free calcium concentra-
1194 tion within the cell cytoplasm. This could have a downstream effect on the functionality of
1195 the cell.

1196 As well as the optimised parameters, the model has 13 fixed parameters than can be
1197 changed to simulate different types of calcium indicators. This model could be used to test
1198 the theoretical performance of proposed new types of calcium indicator. The model could
1199 also be used by developers of spike inference algorithms to test the effects of changing cal-
1200 cium indicator parameters on spike inference, or to test the affects of changing spiking char-
1201 acteristics on spike inference. For example, high firing rate vs low firing rate, or bursting vs
1202 no bursting. Given the increasing amplitude of the fluorescence trace with increasing mean
1203 firing rate, it would be possible to build a spike inference algorithm on this principle at least
1204 in part.

1205 Our model has already been used as a tool by our colleagues, for simulating fluorescence
1206 traces in response to cells that can fire with a continuous rate between 10 and 20Hz, but do
1207 not always do so. Our colleagues found that a combination of the amplitude and the variance
1208 of the simulated fluorescence trace was the best indicator of firing rate. For example, when
1209 a cell was not firing, the amplitude and variance of the fluorescence trace was relatively
1210 low. When the cell fired with a low firing rate $\sim 1\text{Hz}$, the mean amplitude was still low
1211 but the variance of the fluorescence trace was high, and for high firing rate $10 - 20\text{Hz}$, the
1212 fluorescence amplitude was high, and the variance was low. In this way, our model may be
1213 useful for investigating firing rates underlying real fluorescence traces in response to cells
1214 which can fire in these rage ranges.

1215 A recent paper by Greenberg et al (2018) described a biophysical model for spike train

2.4. Discussion

1216 inference called the ‘Sequential binding model’. Their model for spike inference was sim-
1217 ilar to our model for fluorescence traces in that their model included parameters for two
1218 types of endogenous buffer. But this model also included dynamics for calcium binding to
1219 and unbinding from these endogenous buffers. Furthermore, this model included dynamics
1220 for calcium binding to and unbinding from the four binding sites present on a GCaMPs6
1221 molecule. In the accuracy measurements specified in that paper, this model performed better
1222 than the MLspike algorithm, which is also partially a biophysically model, and it performed
1223 better than the constrained non-negative deconvolution algorithm. The sequential binding
1224 model also has biophysically interpretable parameters, and its fitted parameters for quantities
1225 such as buffering capacity and calcium influx upon action potential firing fall in line with
1226 experimental values (Greenberg et al., 2018). Biophysical models like this appear to be the
1227 way forward for spike inference algorithms, and would make a good complimentary tool to
1228 our fluorescence model.

1229 **Chapter 3**

1230 **Functional networks expand across
1231 anatomical boundaries as correlation
1232 time-scale increases**

1233 *Abstract*

1234 Decades of research has established that correlated spiking plays a crucial role in represent-
1235 ing sensory information. One drawback associated with the recent improvement in recording
1236 technology and consequent large datasets is the difficulty in analysing higher order correla-
1237 tions in large neuronal ensembles. One benefit of these datasets that has not yet been explored
1238 is the opportunity to compare correlations within anatomical regions to correlations across
1239 anatomical regions. In this work, we measured correlations between neurons residing in
1240 nine different brains regions in three awake and behaving mice. Using the these correlation
1241 measurements, we created weighted undirected graph networks and applied network science
1242 methods to detect functional communities in our neural ensembles. We compared these func-
1243 tional communities to their anatomical distribution. We repeated the analysis, using different
1244 timescales for our correlation measurements, and found that functional communities were
1245 more likely to be dominated by neurons from a single brain region at shorter timescales
1246 (< 100ms).

1247 3.1 Introduction

1248 Decades of research has established that correlations play a crucial role in representing sen-
1249 sory information. For example, the onset of visual attention has been shown to have a greater
1250 affect on the correlations in the macaque V4 region than on the firing rates in that region
1251 (Cohen and Maunsell, 2009). Recent findings show that spontaneous behaviours explain cor-
1252 relations in parts of the brain not associated with motor control (Stringer et al., 2019), that
1253 satiety state appears to have a brain wide representation (Allen et al., 2019), and that subject
1254 exploratory and non-exploratory states are represented in the amygdala (Gründemann et al.,
1255 2019). So, behavioural states are likely represented across many regions of the brain, not just
1256 motor related areas. In order to understand the brain, we must understand the interactions
1257 between neurons and regions.

1258 Because of limitations in recording technology almost all research has explored corre-
1259 lations between neurons within a given brain region, or within only two regions at most
1260 (Wierzynski et al., 2009; Patterson et al., 2014; Girard, Hupé, and Bullier, 2001). Rela-
1261 tively little is known about correlations between neurons in many different brain regions.
1262 However, the recent development of ‘Neuropixels’ probes (Jun et al., 2017) has allowed
1263 extracellular voltage measurements to be collected from multiple brain regions simultane-
1264 ously routinely, and in much larger numbers than traditional methods. In this project we
1265 used a publicly-available Neuropixels dataset to analyse correlations between different brain
1266 regions (Stringer et al., 2019).

1267 A drawback associated with the improvement in recording technology is an increase in
1268 the difficulty in analysing these data. For example, analysing the i th order interactions of
1269 N neurons generally requires estimation of N^i parameters. A number that becomes astro-
1270 nomical for large N . New methods are required for analysing these new large datasets. We
1271 attempted to address this requirement in this piece of research by applying a cutting-edge
1272 network science community detection method to neural data.

1273 Another unexplored area of research is the changes in cell interactions at different timescales.
1274 Studies have shown different timescales for fluctuations in spiking activity (Murray et al.,
1275 2014), and different time scales for event representation (Baldassano et al., 2017) across dif-
1276 ferent brain regions. Still most studies focus on quantifying interactions at a given timescale.
1277 But neurons may interact differently, or may interact with different neurons at different
1278 timescales. Here we explore correlated communities of neurons at different timescales.

1279 In this work, we measured correlations between binned spike counts from neurons from

3.2. Data

1280 nine different regions of the mouse brain. These measurements induced a weighted undi-
1281 rected graph or network where each neuron is represented by a node, and the strength of
1282 the connection between these nodes/neurons is the strength of the correlation between their
1283 spike counts. We then applied newly invented network methods (Humphries et al., 2019)
1284 to this network to find any community structure, and place the neurons in these correlation
1285 based communities. Finally, we compared these functional communities to the anatomical
1286 membership of the neurons.

1287 To investigate the functional communities and their relationship with anatomy at different
1288 time scales, we repeated these analyses using different length bin widths when binning spike
1289 times.

1290 To find and analyse functional networks while controlling for the subject’s behaviour, we
1291 conditioned the binned spike counts on data from a video of the subject’s face, and repeated
1292 our analysis for spike count correlations (or noise correlations) and signal correlations.

1293 3.2 Data

1294 The data that we used in this project were collected by Nick Steinmetz and his lab members
1295 (Stringer et al., 2019; Steinmetz et al., 2019).

1296 3.2.1 Brain regions

1297 Neuropixels probes were used to collect extracellular recordings (Jun et al., 2017) from three
1298 different mice. The mice were awake, headfixed, and engaging in spontaneous behaviour.
1299 The mice were of different sexes and different ages. One mouse was ‘wild-type’, the others
1300 were mutants. Details as follows:

- 1301 1. male, wild type, P73.
- 1302 2. female, TetO-GCaMP6s, Camk2a-tTa, P113
- 1303 3. male, Ai32, Pvalb-Cre, P99

1304 Eight probes were used to collect readings from 2296, 2668, and 1462 cells respectively.
1305 Data were collected from nine brain regions in each mouse:

- 1306 • Caudate Putamen (CP)
- 1307 • Frontal Motor Cortex (Frmocxt)
- 1308 • Hippocampal formation (Hpf)

- 1309 ● Lateral Septum (Ls)
- 1310 ● Midbrain (Mb)
- 1311 ● Superior Colliculus (Sc)
- 1312 ● Somatomotor cortex (Sommotcx)
- 1313 ● Thalamus (Th)
- 1314 ● Primary visual cortex (V1)

1315 Readings were continuous and lasted for about 1 hour (Stringer et al., 2019; Steinmetz et al.,
1316 2019). Locations of each of the probes can be seen in figure 3.1.

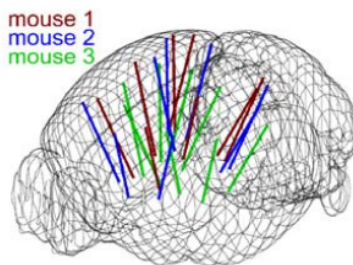


FIGURE 3.1: **Probe Locations:** The locations of the probes in each of the three mouse brains (Stringer et al., 2019).

1317 **3.2.2 Video recordings**

1318 Video recordings of the mouse's face were taken during the spontaneous behaviour. We
1319 had access to the top 500 principal components and top 500 eigenvectors of the processed
1320 videos. The frequency of recording was slightly less than 40Hz. Each frame contained
1321 327×561 pixels (Stringer et al., 2019; Steinmetz, Carandini, and Harris, 2019). These
1322 principal components were used as behavioural data. We controlled for these components
1323 when taking measurements conditioned on behaviour.

1324 **3.3 Methods**

1325 **3.3.1 Binning data**

1326 We transformed the spike timing data into binned spike count data by dividing the experi-
1327 mental period into time bins and counting the spikes fired by each cell within the time period
1328 covered by each of those bins. The data were divided into time bins of various widths ranging
1329 from 0.005s to 4s.

3.3. Methods

If the total length of the recording period was not an integer multiple of the time bin width, we cut off the remaining time at the end of the recording period. This period was at most 3.99s. This is far less than the total recording time of around 1 hour. So, this detail would not affect our results.

3.3.2 Correlation coefficients

We calculated Pearson's correlation coefficient for pairs of spike counts from pairs of neurons. For jointly distributed random variables X and Y , Pearson's correlation coefficient is defined as:

$$\rho_{XY} = \frac{\text{cov}(X, Y)}{\sigma_X \sigma_Y} \quad (3.1)$$

$$= \frac{E[(X - \mu_X)(Y - \mu_Y)]}{\sigma_X \sigma_Y} \quad (3.2)$$

where E denotes the expected value, μ denotes the mean, and σ denotes the standard deviation. The correlation coefficient is a normalised measure of the covariance. It can take values between 1 (completely correlated) and -1 (completely anti-correlated). Two independent variables will have a correlation coefficient of 0, but having 0 correlation does not imply independence.

If we do not know the means and standard deviations required for equation 3.1, but we have samples from X and Y , Pearson's sample correlation coefficient is defined as:

$$r_{XY} = \frac{\sum_{i=1}^n (x_i - \bar{x})(y_i - \bar{y})}{\sqrt{\sum_{i=1}^n (x_i - \bar{x})^2} \sqrt{\sum_{i=1}^n (y_i - \bar{y})^2}} \quad (3.3)$$

where $\{(x_i, y_i)\}$ for $i \in \{1, \dots, n\}$ are the paired samples from X and Y , and $\bar{x} = \frac{1}{n} \sum_{i=1}^n x_i$, and $\bar{y} = \frac{1}{n} \sum_{i=1}^n y_i$ are the sample means.

In practice we used the Python function `scipy.stats.pearsonr` to calculate the correlation coefficients.

1344 Total correlations, r_{SC}

In this context, we defined the total correlation (r_{SC}) of two cells to be the correlation between the spike counts of those cells across the entire period of spontaneous behaviour.

1347 **Shuffled total correlations**

1348 We measured the shuffled total correlations between two neurons by randomly permuting one
 1349 of the neuron's spike counts and measuring the total correlations. These shuffled correlations
 1350 were useful when measuring the effect of time bin width on correlations, and when decid-
 1351 ing which correlations should be preserved when creating correlation networks (see section
 1352 [3.3.5](#)).

1353 **Separating Correlations & Anti-correlations**

1354 In order to compare the effect of bin width on measures of negative r_{SC} (anti-correlation) and
 1355 positive r_{SC} separately, we had to separate correlated and anti-correlated pairs. To do this, we
 1356 simply measured the mean r_{SC} , taking the mean across all the bin widths. If this quantity was
 1357 positive or zero we regarded the pair as positively correlated. If this quantity was negative
 1358 we regarded the pair as anti-correlated.

1359 **3.3.3 Conditioning on behavioural data**

Our behavioural data consisted of the top 500 principal components (PCs) of a processed video recording of the mouse's face (see section [3.2.2](#)). Denoting the spike count of a given cell by X , and the PCs by Z_1, \dots, Z_{500} , we wanted to model X as a function of Z_1, \dots, Z_{500} in order to estimate

$$E[X|Z_1, \dots, Z_{500}] = \int_{x \in X} x P(X = x|Z_1, \dots, Z_{500}) dx \quad (3.4)$$

$$= \int_{x \in X} x \frac{P(X = x, Z_1, \dots, Z_{500})}{P(Z_1, \dots, Z_{500})} dx \quad (3.5)$$

1360 Given the 500 components, a naïve estimation of $P(Z_1, \dots, Z_{500})$ or $P(X, Z_1, \dots, Z_{500})$ by
 1361 histogramming was impossible. Therefore we modelled X as a linear combination of the
 1362 PCs.

1363 **Linear regression**

1364 We modelled the spike count of a given cell, X , as a linear combination of the PCs of the
 1365 video of the mouse's face, $\mathbf{Z} = Z_1, \dots, Z_{500}$. We tried three different types of regularization

1366 • $L1$ or 'Lasso'

1367 • $L2$ or 'Ridge regression'

3.3. Methods

- 1368 • ‘Elastic net’ regularisation (a linear combination of both $L1$ and $L2$ regularisation
1369 penalties)

1370 The elastic net regularisation performed the best, so we stuck with that.

1371 **Elastic net regularisation**

Suppose we wish to model n observations of a random variable X , $\mathbf{x} = (x_1, \dots, x_n)$ using n instances of m predictors $\mathbf{Z} = (Z_1, \dots, Z_m)$. The naïve elastic net criterion is

$$L(\lambda_1, \lambda_2, \boldsymbol{\beta}) = |\mathbf{x} - \mathbf{Z}\boldsymbol{\beta}|^2 + \lambda_2|\boldsymbol{\beta}|_2 + \lambda_1|\boldsymbol{\beta}|_1 \quad (3.6)$$

where

$$|\boldsymbol{\beta}|_2 = \sum_{j=1}^m \beta_j^2 \quad (3.7)$$

$$|\boldsymbol{\beta}|_1 = \sum_{j=1}^m |\beta_j| \quad (3.8)$$

The naïve elastic net estimator $\hat{\boldsymbol{\beta}}$ is the minimiser of the system of equations 3.6 (Zou and Hastie, 2005)

$$\hat{\boldsymbol{\beta}} = \arg \min_{\boldsymbol{\beta}} L(\lambda_1, \lambda_2, \boldsymbol{\beta}) \quad (3.9)$$

1372 We implemented the model using the `ElasticNetCV` method of Python’s
1373 `sklearn.linear_models` package. We chose to put equal weighting on the $L1$ and $L2$
1374 regression parts of equation 3.6. We used 10-fold cross validation to set an optimised value
1375 for $\lambda_1 = \lambda_2$.

1376 As well as using the PCs, we also tried fitting the models using the raw video data recon-
1377 structed from the PCs and eigenvectors. These models performed worse than those using the
1378 PCs. We expected this because each representation contains the same amount of information,
1379 but the raw video representation spreads this information across many more components.
1380 This requires more parameter fitting, but given the same information.

1381 **Conditional covariance**

We calculated the expected value of the conditional covariance using the law of total covariance.

$$\text{cov}(X, Y) = E[\text{cov}(X, Y|Z)] + \text{cov}(E[X|Z], E[Y|Z]) \quad (3.10)$$

1382 where these expected values are calculated with respect to the distribution of Z as a random
1383 variable.

1384 The law of total covariance breaks the covariance into two components. The first com-
1385 ponent $E[\text{cov}(X, Y|Z)]$ is the expected value, under the distribution of Z , of the conditional
1386 covariance $\text{cov}(X, Y|Z)$. This covariance could be interpreted as the unnormalised version
1387 of what Cohen et al. (2011) call the spike count correlation (Cohen and Kohn, 2011), aka.
1388 the noise correlation. In particular, this is the covariance of the spike counts in response to
1389 repeated presentation of identical stimuli.

1390 The second component is analogous to what Cohn et al. (2011) call the *signal correlation*
1391 (Cohen and Kohn, 2011). In particular, $\text{cov}(E[X|Z], E[Y|Z])$ is the covariance between
1392 spike counts in response to different stimuli.

1393 Our linear model gave us 500 coefficients, one for each of Z_1, \dots, Z_{500} . By summing
1394 the linear combination of these coefficients and a set containing one value for each Z_i , we
1395 obtained our model's estimate for the spike count of the cell represented by X . We interpreted
1396 our model as a function that takes a set of values $\{Z_1 = z_1, \dots, Z_{500} = z_{500}\}$ as input and
1397 returns $E[X|Z_1 = z_1, \dots, Z_{500} = z_{500}]$.

1398 Using our linear model, we calculated $E[X|Z_1, \dots, Z_{500}]$ for each cell X and for all sets
1399 of values for $\{Z_1, \dots, Z_{500}\}$ available to us. We used those values to calculate $\text{cov}(E[X|Z_1, \dots, Z_{500}], E[Y|Z_1, \dots, Z_{500}])$
1400 for each pair of cells (X, Y). Then we proceeded to calculate

$$\begin{aligned} E[\text{cov}(X, Y|Z_1, \dots, Z_{500})] &= \text{cov}(X, Y) - \\ &\quad \text{cov}(E[X|Z_1, \dots, Z_{500}], E[Y|Z_1, \dots, Z_{500}]) \end{aligned} \quad (3.11)$$

1401 **Measures of conditional correlation**

As a measure of expected correlation, we measured the ‘event conditional correlation’ (Maugis,
2014)

$$\rho_{XY|Z} = \frac{E[\text{cov}(X, Y|Z)]}{\sqrt{E[\text{var}(X|Z)]E[\text{var}(Y|Z)]}} \quad (3.12)$$

3.3. Methods

1402 Although this is not an actual correlation, it is an intuitive analogue to the correlation as a
1403 normalised version of the covariance.

For comparison, we also measured the ‘signal correlation’

$$\rho_{\text{signal}} = \frac{\text{cov}(E[X|Z], E[Y|Z])}{\sqrt{\text{var}(E[X|Z])\text{var}(E[Y|Z])}} \quad (3.13)$$

1404 this is an actual correlation.

1405 3.3.4 Information Theory

1406 We used an information theory based measure to measure the difference between the com-
1407 munities that we detected in the correlation based functional networks that we constructed
1408 and the anatomical division of the cells in our data. We treated these as clusterings, and mea-
1409 sured the distance between them. We also were planning on using the mutual information
1410 between the spike counts of cells as measure upon which to build functional networks. But
1411 our measurements turned out to be heavily biased. So we abandoned that approach.

1412 As a result, we have here a lot of background on information theory. This information
1413 is still useful for understanding our measure of distance between between clusterings. So I
1414 think it is worth keeping.

1415 Entropy $H(X)$

The entropy of a random variable X , with outcomes x_1, \dots, x_N , and corresponding probabilities p_1, \dots, p_N is defined as

$$H(X) = - \sum_{n=1}^N p_n \log_2 p_n \quad (3.14)$$

1416 This quantity is also known as the information entropy or the ‘surprise’. It measures the
1417 amount of uncertainty in a random variable. For example, a variable with a probability of 1
1418 for one outcome, and 0 for all other outcomes will have 0 bits entropy, because it contains no
1419 uncertainty. But a variable with a uniform distribution will have maximal entropy as it is the
1420 least predictable. This quantity is analogous to the entropy of a physical system (Shannon,
1421 1948). Note that any base may be used for the logarithm in equation 3.14, but using base 2
1422 means that the quantity will be measured in ‘bits’.

The joint entropy of two jointly distributed random variables X and Y , where Y has outcomes y_1, \dots, y_M , is defined as

$$H(X, Y) = - \sum_{n=1}^N \sum_{m=1}^M P(X = x_n, Y = y_m) \log_2 P(X = x_n, Y = y_m) \quad (3.15)$$

- 1423 If X and Y are independent then $H(X, Y) = H(X) + H(Y)$. Otherwise $H(X, Y) <$
 1424 $H(X) + H(Y)$. When X and Y are completely dependent and the mapping from X to Y
 1425 is one-to-one, $H(X, Y) = H(X) = H(Y)$.

The conditional entropy of Y conditioned on X is defined as

$$H(Y|X) = - \sum_{n=1}^N \sum_{m=1}^M P(X = x_n, Y = y_m) \log_2 \frac{P(X = x_n, Y = y_m)}{P(X = x_n)} \quad (3.16)$$

- 1426 When X and Y are independent $H(Y|X) = H(Y)$. Intuitively, we learn nothing of Y by
 1427 knowing X , so Y is equally uncertain whether we know X or not. If Y is totally dependent
 1428 on X , then the fraction in the logarithm is 1, which gives $H(Y|X) = 0$.

1429 These entropy measures are the basis of the mutual information measure.

1430 Maximum entropy limit

- 1431 Originally, we intended to measure the mutual information between the spike counts of cells.
 1432 We included this section to explain why using larger bin widths resulted in potentially larger
 1433 spike counts, containing potentially more information, corresponding with higher mutual
 1434 information values. The idea of measuring the mutual information between spike counts was
 1435 abandoned. But this section was kept as an illustration of how the number of values a random
 1436 variable can take affects the information conveyed by that variable.

When spiking data is binned into spike counts there is an upper limit on the entropy of these data. The maximum entropy discrete distribution is the discrete uniform distribution. A random variable with this distribution will take values from some finite set with equal probabilities. Binned spike count data will take values between 0 and some maximum observed spike count n_{\max} . A neuron with responses that maximises entropy will take these values with equal probability, i.e. if $i \in \{0, \dots, n_{\max}\}$ then $P(X = i) = \frac{1}{n_{\max}+1}$. The entropy of

3.3. Methods

this neuron will be

$$\begin{aligned}
 H(X) &= - \sum_{i=0}^{n_{\max}} P(X = i) \log_2 P(X = i) \\
 &= - \sum_{i=0}^{n_{\max}} \frac{1}{n_{\max} + 1} \log_2 \left(\frac{1}{n_{\max} + 1} \right) \\
 &= - \log_2 \left(\frac{1}{n_{\max} + 1} \right) \\
 &= \log_2 (n_{\max} + 1)
 \end{aligned}$$

1437 Therefore, the maximum entropy of the binned spike counts of a neuron is $\log_2 (n_{\max} + 1)$.
 1438 Of course, it would be very unusual for a neuron to fire in accordance with the discrete
 1439 uniform distribution. Most measurements of entropy taken on binned spiking data will be
 1440 much lower than the maximum. See figure 3.2 to see the maximum entropy as a function of
 1441 the maximum observed spike count.

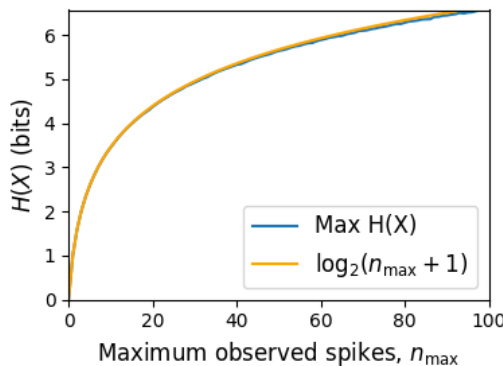


FIGURE 3.2: **Entropy Limit:** The upper limit on entropy of binned spike count data as a function of the maximum observed spike count. The orange line is the analytical maximum. The blue line is the entropy of samples with $N = 1000$ data points taken from the discrete uniform distribution.

1442 **Mutual Information** $I(X; Y)$

1443 The mutual information can be defined mathematically in a number of ways, all of which are
 1444 equivalent. These definitions illustrate the different ways of interpreting the mutual informa-
 1445 tion.

For two jointly distributed random variables X and Y , the mutual information $I(X; Y)$ is defined as

$$I(X; Y) = H(Y) - H(Y|X) \quad (3.17)$$

$$= H(X) - H(X|Y) \quad (3.18)$$

1446 Equation 3.17 fits with the following intuition: The mutual information between X and Y is
1447 the reduction in uncertainty about X gained by knowing Y , or vice versa. We could also say
1448 the mutual information is the amount of information gained about X by knowing Y , or vice
1449 versa.

Another useful entropy based definition for the mutual information is

$$I(X; Y) = H(X) + H(Y) - H(X, Y) \quad (3.19)$$

1450 This definition is useful because it does not require the calculation of conditional probabili-
1451 ties.

The mutual information can also be defined in terms of marginal, joint, and conditional distributions. For example,

$$I(X; Y) = - \sum_{n=1}^N \sum_{m=1}^M P(X = x_n, Y = y_m) \log_2 \frac{P(X = x_n, Y = y_m)}{P(X = x_n)P(Y = y_m)} \quad (3.20)$$

Notice that this can be rewritten as a Kullback–Leibler divergence.

$$I(X; Y) = D_{KL}(P(X, Y) || P(X)P(Y)) \quad (3.21)$$

1452 So, we can also think of the mutual information as a measure of the difference between
1453 the joint distribution of X and Y , and the product of their marginal distributions. Since the
1454 product of the marginal distributions is the joint distribution for independent variables, we
1455 can think of the mutual information as a measure of the variables' dependence on one another.

1456 The minimum value that $I(X; Y)$ can take is 0. This occurs when the random variables
1457 X and Y are independent. Then we have $H(X|Y) = H(X)$, and $H(Y|X) = H(Y)$, which
1458 according to equation 3.17, gives $I(X; Y) = 0$. We also have that $H(X, Y) = H(X) +$
1459 $H(Y)$ in this case, which according equation 3.19, gives $I(X; Y) = 0$. Finally, we also have
1460 $P(X, Y) = P(X)P(Y)$, which leaves us with 1 in the argument for the logarithm in equation
1461 3.20, which again gives $I(X; Y) = 0$.

3.3. Methods

1462 The mutual information reaches its maximum value when one of the variables X and
1463 Y is completely determined by knowing the value of the other. In that case $I(X;Y) =$
1464 $\min\{H(X), H(Y)\}$.

1465 **Variation of Information** $VI(X, Y)$

The variation of information is another information theoretical quantity based on the mutual information. It is defined as

$$VI(X;Y) = H(X) + H(Y) - 2I(X;Y) \quad (3.22)$$

We can rewrite this as the summation of two positive quantities

$$VI(X;Y) = [H(X) - I(X;Y)] + [H(Y) - I(X;Y)] \quad (3.23)$$

1466 In English, the variation of information is the summation of the uncertainty in the random
1467 variables X and Y excluding the uncertainty shared by those variables.

1468 This measure will become more relevant when we go on to talk about clusterings because
1469 $VI(X;Y)$ forms a metric on the space of clusterings.

1470 **Measuring entropies & mutual information**

1471 In practice, we measured the mutual information between spike counts using Python and the
1472 python package `pyitlib`. We used the PT-bias correction technique to estimate the bias of
1473 our measurements when measuring the mutual information between the spike counts of two
1474 cells (Treves and Panzeri, 1995).

1475 When measuring the mutual information between clusterings we used Python, but we
1476 used the `mutual_info_score`, `adjusted_mutual_info_score`, and
1477 `normalized_mutual_info_score` functions from the `sklearn.metrics` part of
1478 the `sklearn` package.

1479 **3.3.5 Network analysis**

1480 **Correlation networks**

1481 In order to analyse functional networks created by the neurons in our ensemble, we mea-
1482 sured the total correlation between each pair of neurons. These measurements induced an

1483 undirected weighted graph/network between the neurons. The weight of each connection
1484 was equal to the total correlation between each pair of neurons.

1485 We followed the same procedure for total correlations 3.3.2, spike count correlations, and
1486 signal correlations 3.3.3.

1487 **Rectified correlations**

1488 At the time of writing, the community detection method outlined in (Humphries et al., 2019)
1489 could only be applied to networks with positively weighted connections. But many neuron
1490 pairs were negatively correlated. To apply the community detection method, we *rectified* the
1491 network, by setting all the negative weights to zero.

1492 We also looked for structure in the network created by negative correlations by reversing
1493 the signs of the correlations, and rectifying these correlations before applying our network
1494 analysis.

1495 Finally, we used the absolute value of the correlations as the weights for the graph/network.
1496 By doing this, we hoped to identify both correlated and anti-correlated functional communi-
1497 ties of neurons.

1498 **Sparsifying data networks**

1499 When creating our correlation networks, we wanted to exclude any correlations that could
1500 be judged to exist ‘by chance’. To do this, we measured the 5th and 95th percentile of
1501 the shuffled correlations (see section 3.3.2) for the given mouse and time bin width. We
1502 then set all the data correlations between these two values to 0. This excluded any ‘chance’
1503 correlations from our network, and created a sparser network. This allowed us to make use
1504 of the ‘sparse weighted configuration model’ as described in section 3.3.5.

1505 **Communities**

1506 Given some network represented by an adjacency matrix \mathbf{A} , a community within that net-
1507 work is defined as a collection of nodes where the number of connections within these nodes
1508 is higher than the expected number of connections between these nodes. In order to quan-
1509 tify the ‘expected’ number of connections, we need a model of expected networks. This is
1510 analogous to a ‘null model’ in traditional hypothesis testing. We test the hypothesis that our
1511 data network departs from the null network model to a statistically significant degree. For
1512 undirected unweighted networks, the canonical model of a null network is the configuration

3.3. Methods

model (Fosdick et al., 2016). Since we are working with weighted sparse networks, we used more suitable null models, described below.

1515 **Weighted configuration model**

1516 The *weighted configuration model* is a canonical null network model for weighted networks.
1517 Given some data network, the weighted configuration model null network will preserve the
1518 degree sequence and weight sequence of each node in the data network. But the edges will
1519 be distributed randomly (Fosdick et al., 2016). Any structure in the data network beyond
1520 its degree sequence and weight sequence will not be captured in the weighted configuration
1521 model. So, this model can be used in testing the hypothesis that this extra structure exists.

1522 **Sparse weighted configuration model**

1523 The *sparse weighted configuration model* is another null network model. Similar in nature to
1524 the weighted configuration model (see section 3.3.5), but the sparsity of the data network is
1525 preserved in the null network. This is achieved by sampling from a probability distribution
1526 for the creation or non-creation of each possible connection, then distributing the weight of
1527 the data network randomly in this sparse network (Humphries et al., 2019). This is the null
1528 network that we used when searching for additional structure in our data networks.

1529 **Spectral rejection**

1530 We made use of the spectral rejection algorithm as outlined in (Humphries et al., 2019). The
1531 spectral rejection algorithm is a method for finding structure in a network not captured by a
1532 supposed null model, if such structure exists.

To describe the method, we denote our data network matrix \mathbf{W} , we denote the expected network of our null network model as $\langle \mathbf{P} \rangle$. Then the departure of our data network from the null network can be described by the matrix

$$\mathbf{B} = \mathbf{W} - \langle \mathbf{P} \rangle \quad (3.24)$$

1533 a common choice for $\langle \mathbf{P} \rangle$ in community detection is the ‘configuration model’ (Fosdick et
1534 al., 2016; Humphries, 2011). The matrix \mathbf{B} is often called the configuration matrix, in this
1535 context we will use the term ‘deviation matrix’ as it captures the deviation of \mathbf{W} from the
1536 null model.

1537 To test for structure in the network represented by \mathbf{W} , we examine the eigenspectrum of \mathbf{B}
1538 and compare it to the eigenspectrum of our null model. Firstly, note that since our data model
1539 doesn't allow self loops, and is not directed, the matrix representing the network will be
1540 symmetric and positive semi-definite, and will therefore be invertible with real eigenvalues.
1541 We selected a null model with the same characteristics.

1542 To find the eigenspectrum of the null model, we generated N samples from our null
1543 model P_1, \dots, P_N , and we measured their deviation matrices B_1, \dots, B_N . We then calculated
1544 the eigenspectrum of each of those samples. We calculated the upper bound of the null model
1545 eigenspectrum by taking the mean of the largest eigenvalues of B_1, \dots, B_N . We calculated a
1546 lower bound on the null model eigenspectrum by taking the mean of the smallest eigenvalues
1547 of B_1, \dots, B_N .

1548 We then calculated the eigenspectrum of \mathbf{B} , our data network deviation matrix. If any of
1549 those eigenvalues lay outside of the upper or lower bounds of the null model eigenspectrum,
1550 this is evidence of additional structure not captured by the null model. If we chose the sparse
1551 weighted configuration model (see section 3.3.5) as our null network model, then eigenvalues
1552 lying below the lower bound indicate k -partite structure in the network. For example, if one
1553 eigenvalue lay below the lower bound, this would indicate some bipartite structure in the data
1554 network. If any eigenvalues lay above the upper bound of the null model eigenspectrum, this
1555 is evidence of community structure in the data network. For example, one eigenvalue of \mathbf{B}
1556 lying above the upper bound of the null model eigenspectrum indicates the presence of two
1557 communities in the network (Humphries, 2011).

1558 **Node rejection**

1559 If there are d data eigenvalues lying outside of the null network eigenspectrum, the d eigen-
1560 vectors corresponding to these eigenvalues will form a vector space. If we project the nodes
1561 of our network into this vector space, by projecting either rows or columns of the data ma-
1562 trix, we can see how strongly each node contributes to the vector space. Nodes that contribute
1563 strongly to the additional structure will project far away from the origin, nodes that do not
1564 contribute to the additional structure will project close to the origin. We want to use this
1565 information to discard those nodes that do not contribute.

1566 We can test whether a node projects *far* away from the origin or *close* to the origin
1567 using the eigenvalues and eigenvectors of B_1, \dots, B_N . The j th eigenvector and eigenvalue
1568 of B_i gives a value for a null network's projection into the j th dimension of the additional
1569 structure vector space. The matrices B_1, \dots, B_N give N projections into that dimension.

3.3. Methods

1570 These projections are a distribution of the null networks' projections. If the data node's
1571 projection exceeds that of the null network projections this node is judged to project *far* from
1572 the origin, and therefore contribute to the additional structure. Otherwise, the node is judged
1573 to project *close* to the origin, and is therefore rejected (Humphries et al., 2019).

1574 **Community detection**

1575 Another application for this d dimensional space is community detection. We first project
1576 all of the nodes into this d -dimensional space, then perform the clustering in this space. The
1577 clustering and community detection procedure is described in (Humphries, 2011).

1578 In practice, the procedure is carried out n times (we chose $n = 100$ times), this returns n
1579 clusterings. We resolve these n clusterings to one final clustering using *consensus clustering*.
1580 We used the consensus clustering method that uses an explicit null model for the consensus
1581 matrix, as outlined in (Humphries et al., 2019).

1582 **3.3.6 Clustering Comparison**

A clustering \mathcal{C} is a partition of a set D into sets C_1, C_2, \dots, C_K , called clusters, that satisfy the following for all $k, l \in \{1, \dots, K\}$:

$$C_k \cap C_l = \emptyset \quad (3.25)$$

$$\bigcup_{k=1}^K C_k = D \quad (3.26)$$

1583 If we consider two clusterings, \mathcal{C} with clusters C_1, C_2, \dots, C_K and \mathcal{C}' with clusters
1584 C'_1, C'_2, \dots, C'_K . There are a number of measurements we can use to compare \mathcal{C} and \mathcal{C}' . In
1585 the following, the number of elements in D is denoted by n , and the number of elements in
1586 cluster C_k is n_k .

1587 **Adjusted Rand Index**

1588 The *adjusted Rand Index* is a normalised similarity measure for clusterings based on pair
1589 counting.

1590 If we consider the clusterings \mathcal{C} and \mathcal{C}' , and denote

1591 • the number of pairs in the same cluster in \mathcal{C} and \mathcal{C}' by N_{11}

1592 • the number of pairs in different clusters in \mathcal{C} and \mathcal{C}' by N_{00}

- 1593 • the number of pairs in the same cluster in \mathcal{C} and different clusters in \mathcal{C}' by N_{10}
- 1594 • the number of pairs in different clusters in \mathcal{C} and the same cluster in \mathcal{C}' by N_{01}

then the *Rand Index* is defined as

$$RI = \frac{N_{11} + N_{00}}{N_{11} + N_{00} + N_{10} + N_{01}} = \frac{N_{11} + N_{00}}{\binom{n}{2}} \quad (3.27)$$

- 1595 The Rand Index is 1 when the clusterings are identical, and 0 when the clusterings are com-
1596 pletely different.

The *adjusted Rand Index* intends on correcting the Rand Index for chance matching pairs.

This is defined as

$$ARI = \frac{2(N_{00}N_{11} - N_{01}N_{10})}{(N_{00} + N_{01})(N_{01} + N_{11}) + (N_{00} + N_{10})(N_{10} + N_{11})} \quad (3.28)$$

- 1597 The adjusted Rand Index is 1 when the clusterings are identical, and 0 when the Rand Index
1598 is equal to its expected value.

1599 When the number of clusters in each clustering is different, the concept of a pair of
1600 being in the same cluster in both clusterings becomes difficult to define. To address this, two
1601 clusterings are drawn randomly with $N_{\mathcal{C}}$ and $N_{\mathcal{C}'}$ number of clusters respectively, and a fixed
1602 number of elements in each cluster corresponding to the number of elements in each cluster
1603 in \mathcal{C} and \mathcal{C}' . Then the adjusted Rand Index is the normalised difference between the Rand
1604 Index of \mathcal{C} and \mathcal{C}' and the mean value of the Rand Index measured using many pairs of these
1605 ‘random’ clusterings.

1606 Clustering as random variables

If we take any random element of D , the probability that this element is in cluster C_k of
clustering \mathcal{C} is

$$P(K = k) = \frac{n_k}{n} \quad (3.29)$$

- 1607 this defines a probability distribution, which makes the clustering a random variable. Any
1608 clustering can be considered as a random variable this way.

3.3. Methods

This means that we can measure any of the information theoretic quantities defined in section 3.3.4 with respect to clusterings. For example, the entropy of a clustering is

$$H(\mathcal{C}) = - \sum_{k=1}^K \frac{n_k}{n} \log \frac{n_k}{n} \quad (3.30)$$

If we have two clusterings, the joint probability distribution of these clusterings is defined as

$$P(K = k, K' = k') = \frac{|C_k \cap C'_{k'}|}{n} \quad (3.31)$$

- ¹⁶⁰⁹ The joint distribution allows us to define the mutual information between two clusterings,
- ¹⁶¹⁰ $I(\mathcal{C}; \mathcal{C}')$ (Meilă, 2007).

¹⁶¹¹ Information based similarity measures

The mutual information between two clusterings is a similarity measure, with $I(\mathcal{C}; \mathcal{C}') = 0$ if \mathcal{C} and \mathcal{C}' are completely different, and $I(\mathcal{C}; \mathcal{C}') = H(\mathcal{C}) = H(\mathcal{C}')$ if \mathcal{C} and \mathcal{C}' are identical. This can be normalised in a number of different ways to make more similarity measures (Vinh, Epps, and Bailey, 2010)

$$NMI_{joint} = \frac{I(\mathcal{C}; \mathcal{C}')}{H(\mathcal{C}, \mathcal{C}')} \quad (3.32)$$

$$NMI_{max} = \frac{I(\mathcal{C}; \mathcal{C}')}{\max\{H(\mathcal{C}), H(\mathcal{C}')\}} \quad (3.33)$$

$$NMI_{sum} = \frac{2I(\mathcal{C}; \mathcal{C}')}{H(\mathcal{C}) + H(\mathcal{C}')} \quad (3.34)$$

$$NMI_{sqrt} = \frac{I(\mathcal{C}; \mathcal{C}')}{\sqrt{H(\mathcal{C})H(\mathcal{C}')}} \quad (3.35)$$

$$NMI_{min} = \frac{I(\mathcal{C}; \mathcal{C}')}{\min\{H(\mathcal{C}), H(\mathcal{C}')\}} \quad (3.36)$$

We can control for chance similarities between the two clusterings by measuring the *adjusted mutual information* between the clusterings. This is defined as

$$AMI_{sum} = \frac{I(\mathcal{C}; \mathcal{C}') - E\{I(\mathcal{C}; \mathcal{C}')\}}{\frac{1}{2}[H(\mathcal{C}) + H(\mathcal{C}')] - E\{I(\mathcal{C}; \mathcal{C}')\}} \quad (3.37)$$

- ¹⁶¹² The first term in the denominator, taking the average of the marginal entropies, can be replaced by taking the maximum, minimum, or the geometric mean (Vinh, Epps, and Bailey, 2010).

1615 **Information based metrics**

The variation of information between two clusterings $VI(\mathcal{C}; \mathcal{C}')$ (see section 3.3.4) is a metric on the space of clusterings (Meilă, 2007). That is,

$$VI(\mathcal{C}; \mathcal{C}') \geq 0 \quad (3.38)$$

$$VI(\mathcal{C}; \mathcal{C}') = 0 \iff \mathcal{C} = \mathcal{C}' \quad (3.39)$$

$$VI(\mathcal{C}; \mathcal{C}') = VI(\mathcal{C}'; \mathcal{C}) \quad (3.40)$$

$$VI(\mathcal{C}; \mathcal{C}'') \leq VI(\mathcal{C}; \mathcal{C}') + VI(\mathcal{C}'; \mathcal{C}'') \quad (3.41)$$

Another metric is the *information distance* (Vinh, Epps, and Bailey, 2010)

$$D_{max} = \max\{H(\mathcal{C}), H(\mathcal{C}')\} - I(\mathcal{C}; \mathcal{C}') \quad (3.42)$$

Both of these can be normalised

$$NVI(\mathcal{C}; \mathcal{C}') = 1 - \frac{I(\mathcal{C}; \mathcal{C}')}{H(\mathcal{C}, \mathcal{C}')} \quad (3.43)$$

$$d_{max} = 1 - \frac{I(\mathcal{C}; \mathcal{C}')}{\max\{H(\mathcal{C}), H(\mathcal{C}')\}} \quad (3.44)$$

1616 **Comparing detected communities and anatomical divisions**

1617 In order to quantify the difference or similarity between the communities detected in our cor-
 1618 relation network and the anatomical classification of the cells in that network, we considered
 1619 the communities and the anatomical regions as clusters in two different clusterings, \mathcal{C}_{comm}
 1620 and \mathcal{C}_{anat} , respectively. We then measured the similarity between the clusterings using the
 1621 mutual information, the adjusted mutual information, and the normalised mutual informa-
 1622 tion. We measured the difference between, or the distance between, the clusterings using the
 1623 variation of information, the normalised variation of information, and the normalised infor-
 1624 mation distance. We also measured the difference between the clusterings using the adjusted
 1625 Rand Index, just to use a non-information based measure.

1626 We took all of these measures for communities detected using different time bin widths.
 1627 This gave us an idea of the effect of time bin width on correlation networks in neural ensem-
 1628 bles relative to anatomical regions within those ensembles.

3.4. Results

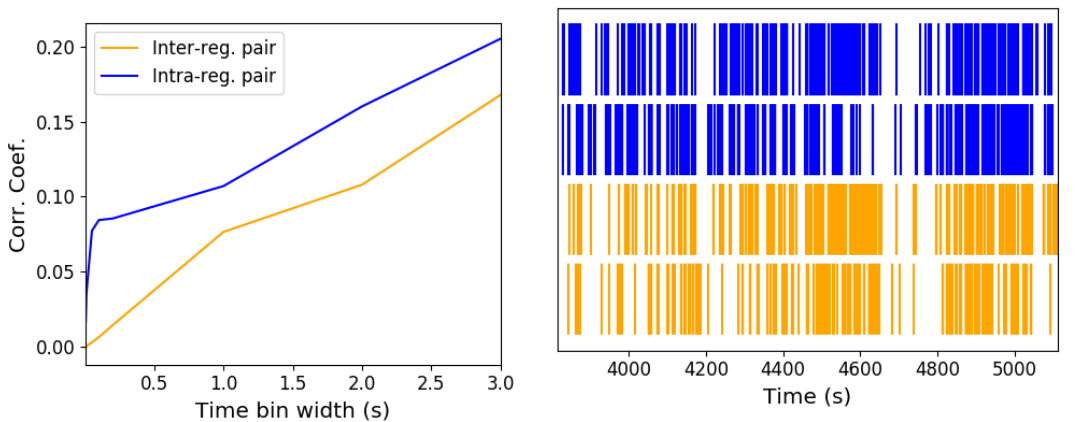
3.4 Results

Note that in the following text, we refer to the correlation coefficient between two sequences of spike counts from two different cells as the *total correlation*. We refer to the correlation between spike counts in response to a certain stimulus as the *spike count correlation* aka *noise correlation*, and we refer to the correlation between mean or expected responses to different stimuli as the *signal correlation* (Cohen and Kohn, 2011).

The nine different brain regions from which we had data were the caudate putamen (CP), frontal motor cortex (FrMoCtx), hippocampus (HPF), lateral septum (LS), midbrain (MB), primary visual cortex (V1), superior colliculus (SC), somatomotor cortex (SomMoCtx), and thalamus (TH).

3.4.1 Average correlation size increases with increasing time bin width

First we inspected the affect of time bin width on total correlations. We know that using short time bins results in artificially small correlation measurements (Cohen and Kohn, 2011), so we expected to see an increase in correlation amplitude with increasing time bin width. That is exactly what we observed. Taking 50 cells at random, we calculated the total correlation between every possible pair of these cells, using different time bin widths ranging from 0.005s to 3s. We found that the longer the time bin width, the greater the correlations (see figure 3.4a).



(A) Correlation coefficient as a function of bin width. (B) Raster plots for the four cells making up our example pairs.

FIGURE 3.3: (A) An example of the correlation coefficients between two different pairs of cells, one where both cells are in the same brain region (intra-regional pair), and one where both cells are in different brain regions (inter-regional pair). The correlation coefficients have been measured using different time bin widths, ranging from 5ms to 3s. Note the increasing amplitude of the correlations with increasing bin width. (B) A raster plot showing the spike times of each pair of cells.

1647 We also separated the positively correlated pairs from the negatively correlated pairs
1648 using the mean correlation of each pair across all bin widths (see section 3.3.2). We found
1649 that the positively correlated pairs become more positively correlated with increasing time bin
1650 width, and the negatively correlated pairs become more negatively correlated with increasing
1651 time bin width (see figures 3.4b and 3.4c).

1652 In figure 3.3a we plot correlations from two example pairs, one pair from within a region,
1653 and one pair between regions. It can be seen that the correlation coefficient increases with
1654 bin width. The correlations can be observed by eye in the raster plot for these cells in figure
1655 3.3b.

1656 When taking the mean across all pairs, the positively correlated pairs dominate in terms
1657 of both number of pairs, and amplitude of correlations. Therefore the mean across all pairs
1658 is positive.

1659 These results were observed in each of the three mouse subjects from which we had data.

1660 3.4.2 Goodness-of-fit for Poisson and Gaussian distributions across increasing 1661 time bin widths

1662 We wanted to investigate if the width of the time bin used to bin spike times into spike counts
1663 had an effect on the distribution of spike counts. We used the χ^2 statistic as a goodness-of-fit
1664 measure for Poisson and Gaussian (normal) distributions to the spike count of 100 randomly
1665 chosen neurons for a number of bin widths ranging from 0.01s to 4s. For the χ^2 statistic, the
1666 higher the value, the worse the fit.

1667 We expected a Poisson distribution to be a better fit for shorter time bin widths because
1668 spike counts must be non-negative, therefore any distribution of spike counts with mass dis-
1669 tributed at or close to 0 will be skewed. The distribution of spike counts is more likely to be
1670 distributed close to 0 when the time bin widths used to bin spike times into spike counts are
1671 small relative to the amount of time it takes for a neuron to fire an action potential ($\sim 1\text{ms}$ in
1672 the case of non-burst firing neurons).

1673 We expected a Gaussian distribution to be a better fit for longer time bin widths, because
1674 a Poisson distribution with a large rate is well approximated by a Gaussian distribution with
1675 mean and variance equal to the Poisson rate. Therefore, a Gaussian distribution would ap-
1676 proximate the mean of a collection of large spike counts, and have more flexibility than a
1677 Poisson distribution to fit the variance.

3.4. Results

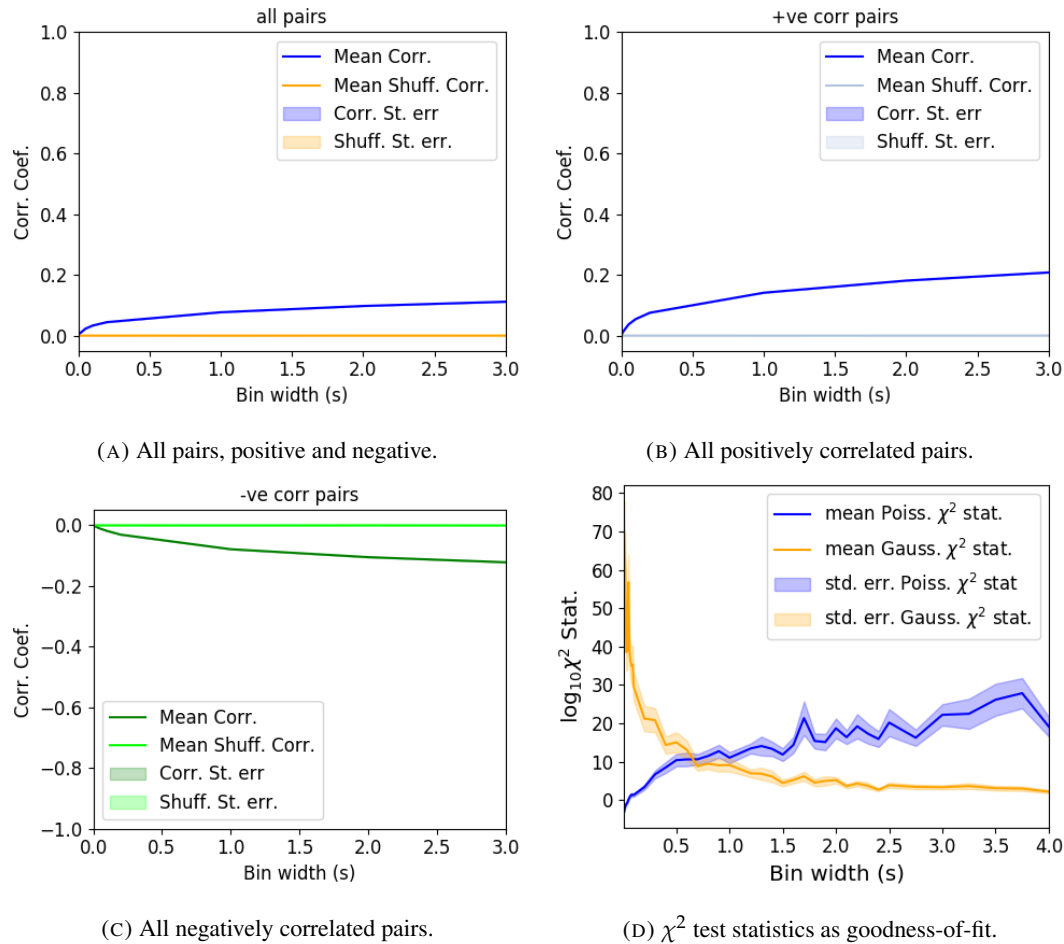


FIGURE 3.4: Mean correlation coefficients measured from pairs of 50 randomly chosen neurons. (A) All possible pairs, (B) positively correlated pairs, and (C) negatively correlated pairs. (D) Mean and standard error of χ^2 test statistics for Poisson and Gaussian distributions fitted to neuron spike counts.

1678 We found that that a Poisson distribution is the best fit for shorter time bins less than 0.7s
1679 in length. Then a Gaussian distribution is a better fit for time bins greater than 0.7s in length
1680 (see figure 3.4d).

1681 **3.4.3 Differences between and inter- and intra- regional correlations decrease
1682 with increasing bin width**

1683 We investigated the differences in distribution between inter-regional correlations, i.e. corre-
1684 lations between neurons in different brain regions, and intra-regional correlations, i.e. corre-
1685 lations between neurons in the same brain region.

1686 Firstly, we investigated these quantities for all possible pairs of ~ 500 neurons taken
1687 from across all the 9 brain regions from which we had data. We distributed these neurons as
1688 evenly as possible across all of the regions, so that cells from one region would not dominate
1689 our data. We observed that the mean intra-regional correlations were always higher than the
1690 mean inter-regional correlations for every value of time bin width used. We also observed
1691 that as the time bin width increased these mean correlations increased and the difference
1692 between the mean inter-regional and intra-regional correlations grew (see figure 3.5 (Left)).

1693 Stringer et al. (2019) had a similar finding using the same data. They used only one value
1694 for the time bin width, 1.2s. Using this time bin width to bin spike times and measure total
1695 correlations, they found that the mean ‘within-region’ correlations were always greater than
1696 the ‘out-of-region’ correlations (Stringer et al., 2019). The figure from their paper showing
1697 this result can be seen in figure 3.5 (Right).

1698 Examples of the correlations of one intra-regional pair and one inter-regional pair can be
1699 seen in figure 3.3.

1700 Secondly, we separated those pairs into intra-regional and inter-regional groups. We
1701 noted that the mean intra-regional correlations (coloured dots in figures 3.6a and 3.6b) for
1702 a given region tended to be higher than the mean inter-regional correlations (black dots in
1703 figures 3.6a and 3.6b) involving cells from that region. However, in contrast with our previous
1704 result, we noted that the difference between the mean intra-regional correlations and most
1705 highly correlated inter-regional correlations reduced as we increased the time bin width (see
1706 figures 3.6a and 3.6b). This shows that the mean correlations showin in figure 3.5 are not
1707 distributed evenly across all region pair combinations.

1708 Finally, to see these regional mean correlations in a bit more detail, to examine the indi-
1709 vidual pair combinations in particular, we displayed these data in a matrix of mean corre-
1710 lations (see figure 3.7), showing the mean intra-regional correlations on the main diagonal, and

3.4. Results

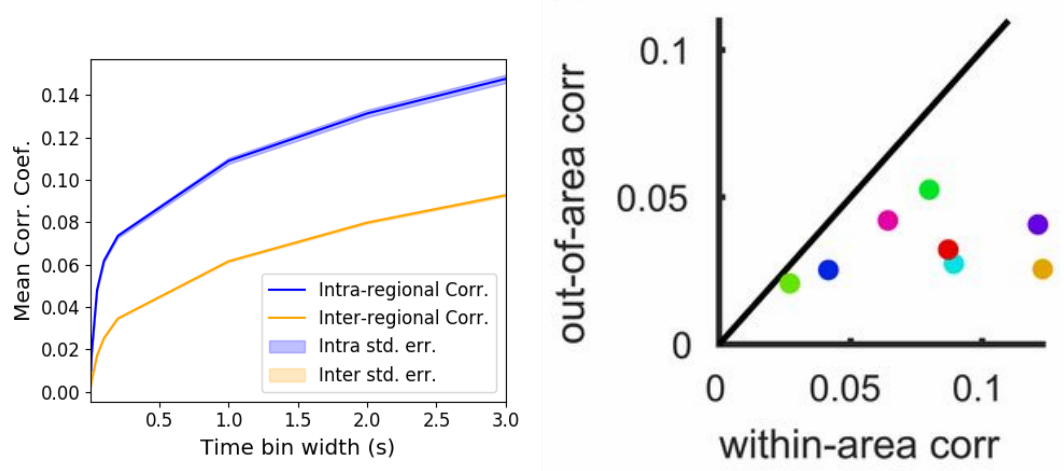


FIGURE 3.5: (Left) The mean intra-region and inter-region correlations using all possible pairs of ~ 500 neurons, spread across 9 different brain regions. (Right) Courtesy of Stringer et al. (2019), mean inter-regional (out-of-area) correlation coefficients vs mean intra-regional (within-area) correlation coefficients for a bin width of 1.2s. Note that the intra-regional coefficients are higher in each case.

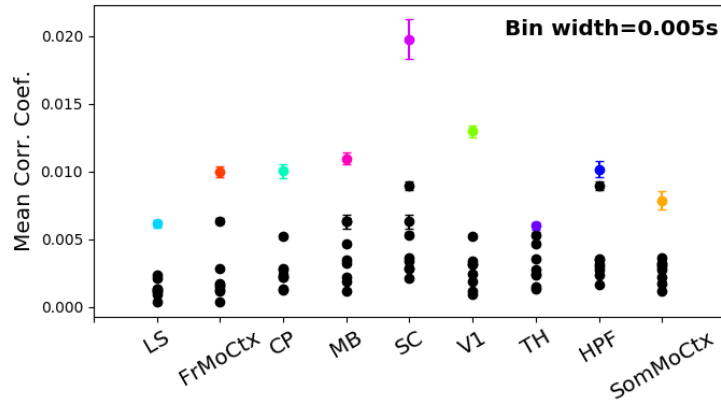
1711 the mean inter-regional correlations off diagonal. Comparing a version of this figure created
 1712 using a short time bin width of 5ms (figure 3.7a) and a version using a longer time bin width
 1713 of 1s (figure 3.7b) we observed that the mean intra-regional correlations are always relatively
 1714 high in comparison to the mean inter-regional correlations, but the mean correlations in some
 1715 inter-regional pairs are relatively much higher when using the longer time bin width.

1716 This could indicate information being processed quickly at a local or within-region level,
 1717 and the local representations of this information spreading between regions at longer timescales.

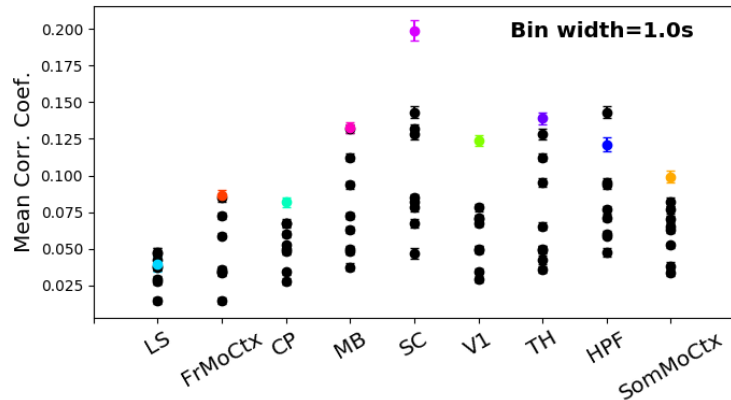
1718 These results were consistent across the three mouse subjects. But, the relative magni-
 1719 tudes of the mean intra-regional and inter-regional correlations were not consistent. For ex-
 1720 ample, the region with the highest mean intra-regional correlations when using 1s bin widths
 1721 for subject one is the superior colliculus (SC), but for subject two it is the midbrain (MB).

1722 **3.4.4 Connected and divided structure in correlation based networks reduces
 1723 in dimension with increasing bin width**

1724 We used the correlation measurements to create weighted undirected graphs/networks where
 1725 each node represents a neuron, and the weight of each edge is the pairwise correlation be-
 1726 tween those neurons represented by the nodes at either end of that edge. We aimed to find
 1727 communities of neurons within these networks, and compare the structure of these commu-
 1728 nities to the anatomical division of those neurons. The first step of this process involved
 1729 applying the ‘spectral rejection’ technique developed by Humphries et al (2019) (Humphries



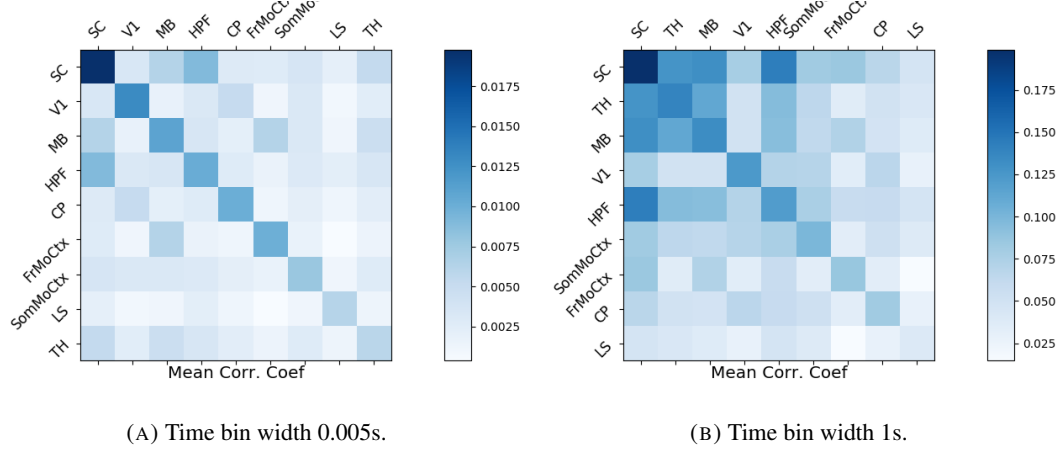
(A) Mean inter-regional and intra-regional correlations using a time bin width of 5ms.



(B) Mean inter-regional and intra-regional correlations using a time bin width of 1s.

FIGURE 3.6: The mean intra-regional correlations (coloured dots) and mean inter-regional correlations (black dots) for a given region, indicated on the x-axis, for different time bin widths. Each black dot represents the mean inter-regional correlations between the region indicated on the x-axis and one other region. (A) shows these measurements when we used a time bin width of 5ms. (B) shows these measurements when we used a time bin width of 1s. Note that the difference between the mean inter-regional correlations and mean intra-regional correlations is smaller for 1s bins.

3.4. Results



(A) Time bin width 0.005s. (B) Time bin width 1s.

FIGURE 3.7: Mean inter-regional (main diagonal) and intra-regional (off diagonal) correlation coefficients. (A) Shows these measurements when spike times were binned using 5ms time bins. (B) Shows the same, using 1s time bins. Note that the matrices are ordered according to the main diagonal values, therefore the ordering is different in each subfigure.

et al., 2019). This technique compares our data network to a chosen null network model, and finds any additional structure in the data network beyond that which is captured in the null network model (if there is any such structure).

By comparing the eigenspectrum of the data network to the eigenspectrum of many samples from the null network model, this technique allows us to estimate the dimensionality of the additional structure in the data network, and gives us a basis for that vector space. It also divides the additional structure into connected structure, and k -partite (or divided) structure. For example, if our algorithm found two dimensions of additional connected structure, and one dimension of additional divided structure. We might expect to find three communities, that is groups more strongly connected within group than without, and we might expect to find bi-partite structure, that is two sets that are more strongly connected between groups than within groups.

The technique also finds which nodes contribute to this additional structure, and divides our data network into signal and noise networks. The details of spectral rejection and node rejection can be found in sections 3.3.5 and 3.3.5 respectively, and a full overview can be found in (Humphries et al., 2019).

We chose the sparse weighted configuration model (see section 3.3.5) as our null network model. This model matches the sparsity and the total weight of the original network but distributes the weight at random across the sparse network.

We applied the spectral rejection method to our networks based on total correlations using different values for the time bin width. We observed that for smaller time bin widths, our data

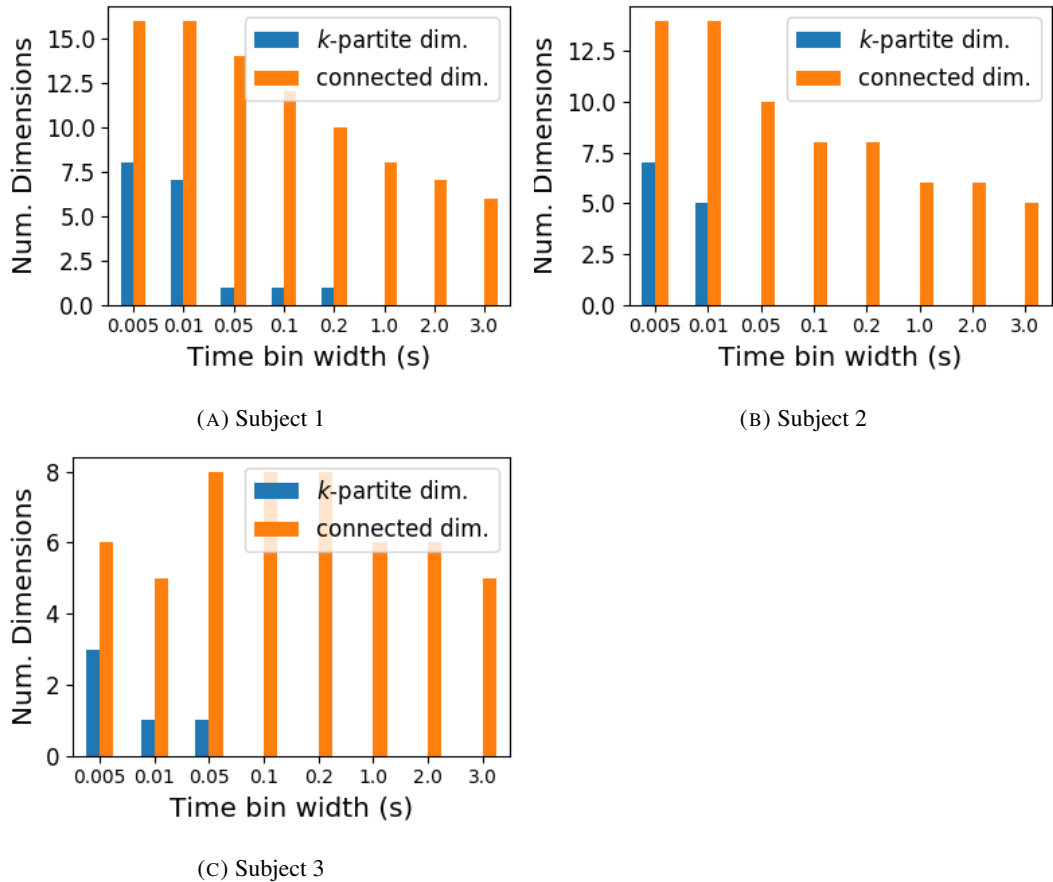


FIGURE 3.8: The number of dimensions in the k -partite and connected structure in the correlation based networks beyond the structure captured by a sparse weighted configuration null network model (see section 3.3.5), shown for different time bin widths. Note that the k -partite structure disappears for time bin width greater than 200ms for all three subjects. The dimension of the connected structure reduces with increasing bin width for 2 of the 3 subjects (top row).

3.4. Results

networks had both k -partite structure, and community structure. As the width of the time bin increased, we found that the k -partite structure disappeared from our data networks, and the dimension of the community structure reduced in two of the three mice from which we had data (see figure 3.8).

The reduction in dimensionality of the connected structure with larger bin widths could indicate information or activity being integrated through the merging of smaller functionaly communities over longer timescales.

The k -partite structure that we found when using small bin widths could be an indication of physical connections between neurons. This is supported by the fact that these k -partite communities are not found over longer timescales. The effect of physical connections through axodendritic or dendrodendritic synapses would only be noticeable at short timescales.

3.4.5 Detecting communities in correlation based networks

We applied the community detection procedure described in section 3.3.5 to our signal networks for our various time bin widths. We detected a greater number of smaller communities at shorter time bin widths, and a smaller number of larger communities for longer time bin widths (see figure 3.9). This was expected after the results found in section 3.4.4. We found more dimensions of additional structure at shorter time bin widths, therefore we found more communities at shorter time bin widths.

The number of communities that we detected was always greater than the dimensionality of the additional structure that we found by applying spectral rejection.

We also noticed that at short time bin widths the communities detected tended to be dominated by cells from one region. Whereas communities existing in networks created using wider time bin widths tended to contain cells from many different brain regions. More on this in the next section.

3.4.6 Functional communities resemble anatomical division at short timescales

In order to quantify the similarity of the communities detected to the anatomical division of the cells. We treated both the anatomical division and the communities as clusterings of these cells. We then used measures for quantifying the difference or similarity between clusterings to quantify the difference or similarity between the detected communities and the anatomical division. Details of these measures can be found in section 3.3.6 or in (Vinh, Epps, and Bailey, 2010).

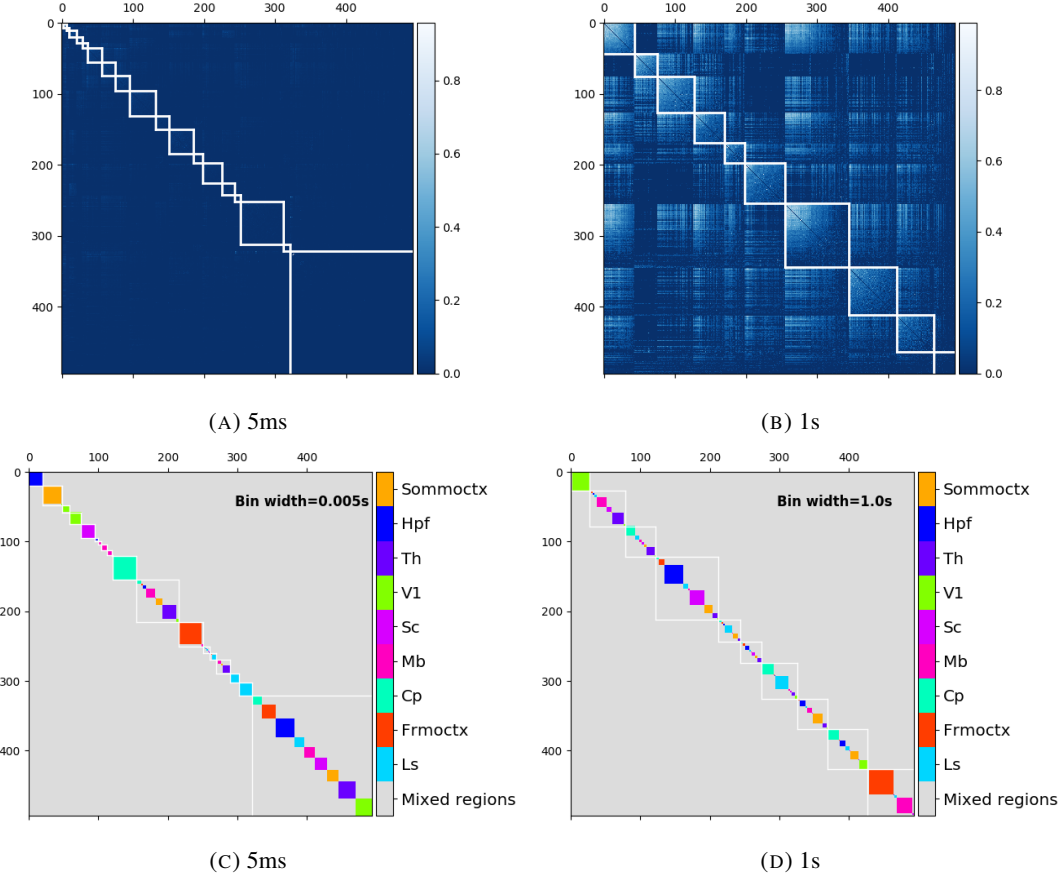


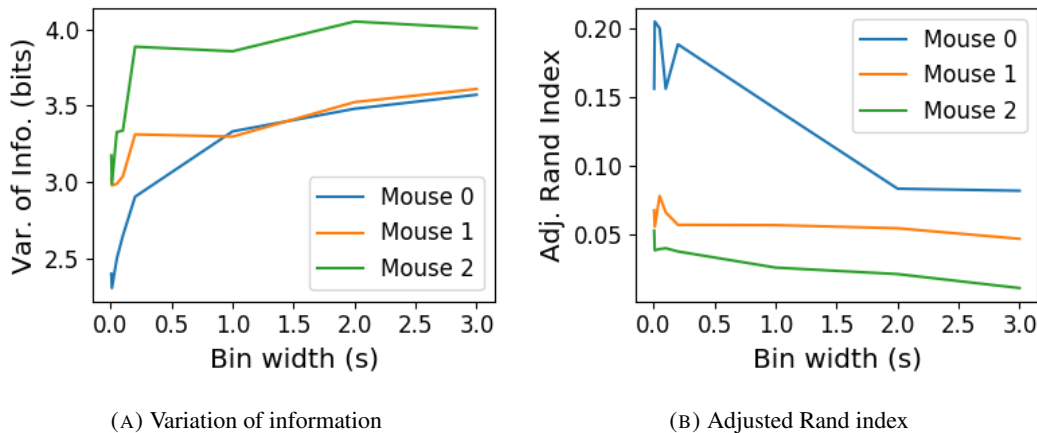
FIGURE 3.9: (A-B) Correlation matrices with detected communities indicated by white lines. Each off main diagonal entry in the matrix represents a pair of neurons. Those entries within a white square indicate that both of those neurons are in the same community as detected by our community detection procedure. Matrices shown are for 5ms and 1s time bin widths respectively. Main diagonal entries were set to 0. (C-D) Matrices showing the anatomical distribution of pairs along with their community membership. Entries where both cells are in the same region are given a colour indicated by the colour bar. Entries where cells are in different regions are given the grey colour also indicated by the colour bar.

3.4. Results

We used two different types of measures for clustering comparison; information based measures (see section 3.3.6) and pair counting based measures (see section 3.3.6). We include one example of each in figure 3.10.

The variation of information is the information based measure included in figure 3.10a. This measure forms a metric on the space of clusterings. The larger the value for the variation of information, the more different the clusterings.

The adjusted Rand index is the pair counting based measure included in figure 3.10b. In contrast with the variation of information, the adjusted Rand index is a normalised similarity measure. The adjusted Rand index takes value 1 when the clusterings are identical, and takes value 0 when the clusterings are no more similar than chance.



(A) Variation of information

(B) Adjusted Rand index

FIGURE 3.10: (A) The variation of information is a measure of distance between clusterings. The distance between the anatomical ‘clustering’ and community detection ‘clustering’ increases with increasing time bin width. (B) The adjusted Rand index is a normalised similarity measure between clusterings. The anatomical and community detection clusterings become less similar as the time bin width increases.

Both measures indicated that the detected communities and the anatomical division of the cells were more similar when we used shorter time bins widths (see figure 3.10). This indicates that correlated behaviour in neuronal ensembles is more restricted to individual brain regions at short timescales (< 250ms), and the correlated activity spreads out across brain regions over longer time scales.

3.4.7 Conditional correlations & signal correlations

In light of the excellent research of Stringer et al (2019) showing that spontaneous behaviours can drive activity in neuronal ensembles across the visual cortex and midbrain (Stringer et al., 2019), we decided to control for the mouse’s behaviour when performing our analyses. It is possible that our community detection process may be detecting communities across

multiple brain regions at longer time scales due to aggregating neuronal activity driven by several spontaneous behaviours occurring during the time interval covered by a given time bin. A time bin of 1s, for example, could contain a spike count where those spikes were driven by different spontaneous behaviours. We aimed to investigate this possibility by applying our community detection analysis to conditional correlation measures.

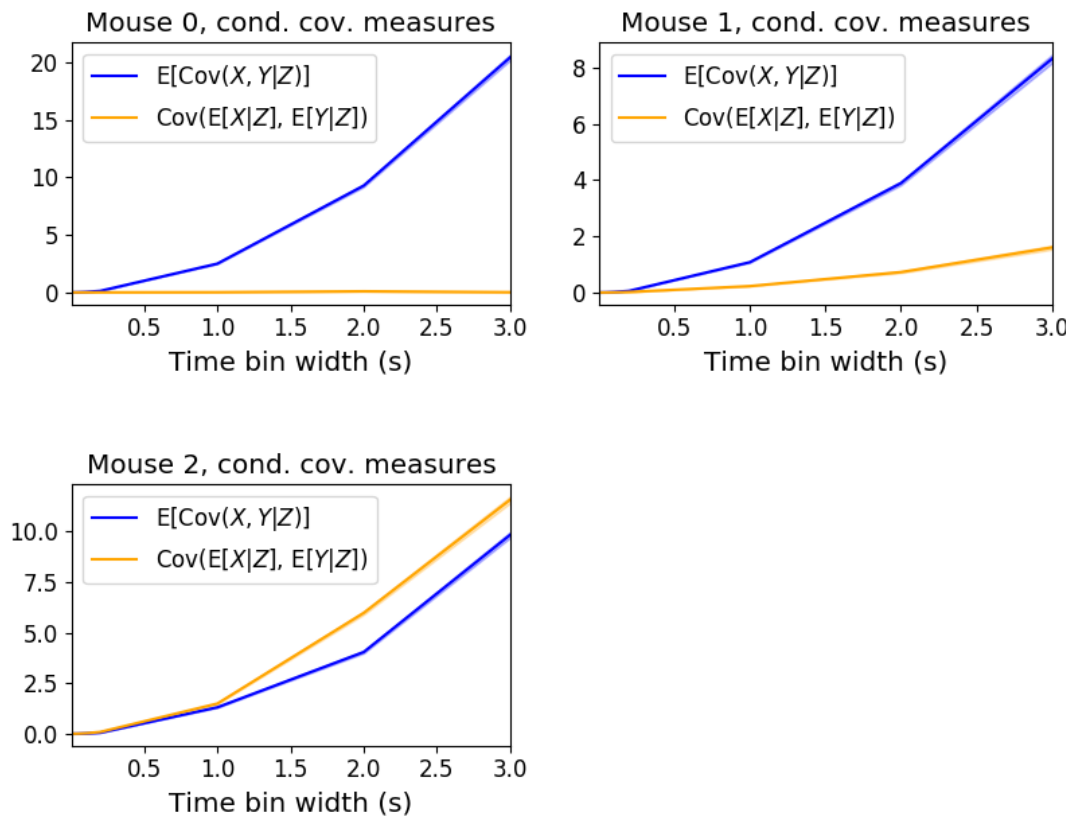


FIGURE 3.11: Comparing the components of the total covariance across different values for the time bin width. We observed a consistent increase in $E[\text{cov}(X, Y|Z)]$ as the time bin width increased. But we saw different trends for $\text{cov}(E[X|Z], E[Y|Z])$ for each mouse.

We used the top 500 principal components of a video of the mouse's face as a measure of the mouse's behaviour (see section 3.2.2). We modelled the spike counts as a linear combination of the principal components using linear regression with ElasticNet regularisation (see section 3.3.3). Using this model, we quantified the expected spike count given the mouse's behaviour $E[X|Z_1, \dots, Z_{500}]$.

We used these expected values to measure $\text{cov}(E[X|Z], E[Y|Z])$, and we used that value, the covariance $\text{cov}(X, Y)$, and the *law of total covariance* (see section 3.3.3) to measure

3.4. Results

1815 $E[\text{cov}(X, Y|Z)]$. Here X and Y represent spike counts from individual cells, and Z is short-
 1816 hand for the 500 principal components mentioned above. The two components of the co-
 1817 variance, $\text{cov}(E[X|Z], E[Y|Z])$ and $E[\text{cov}(X, Y|Z)]$, represent a ‘signal covariance’ and ex-
 1818 pected value of a ‘spike count covariance’ respectively, analogous to the signal correlation
 1819 and spike count correlation (Cohen and Kohn, 2011).



FIGURE 3.12: Comparing the components of the total covariance across different values for the time bin width. We saw a consistent increase in $\rho_{X,Y|Z}$ as the time bin width increased in all three subjects. But we saw different trends in ρ_{signal} for each of the subjects.

1820 We examined the means of these components for different values of the time bin width
 1821 (see figure 3.11). We observed a consistent increase in $E[\text{cov}(X, Y|Z)]$ as the time bin width
 1822 increased. But we saw different trends for $\text{cov}(E[X|Z], E[Y|Z])$ for each mouse.

1823 Using $\text{cov}(E[X|Z], E[Y|Z])$ we measured the signal correlation, ρ_{signal} , and using $E[\text{cov}(X, Y|Z)]$
 1824 we measured the event conditional correlation, $\rho_{X,Y|Z}$ (see section 3.3.3 for more details).
 1825 We saw a consistent increase in $\rho_{X,Y|Z}$ as the time bin width increased, this corresponds to
 1826 the result for $E[\text{cov}(X, Y|Z)]$. We observed different trends for ρ_{signal} for each mouse, this
 1827 corresponds to the result for $\text{cov}(E[X|Z], E[Y|Z])$.

1828 We applied our network noise rejection and community detection process to networks

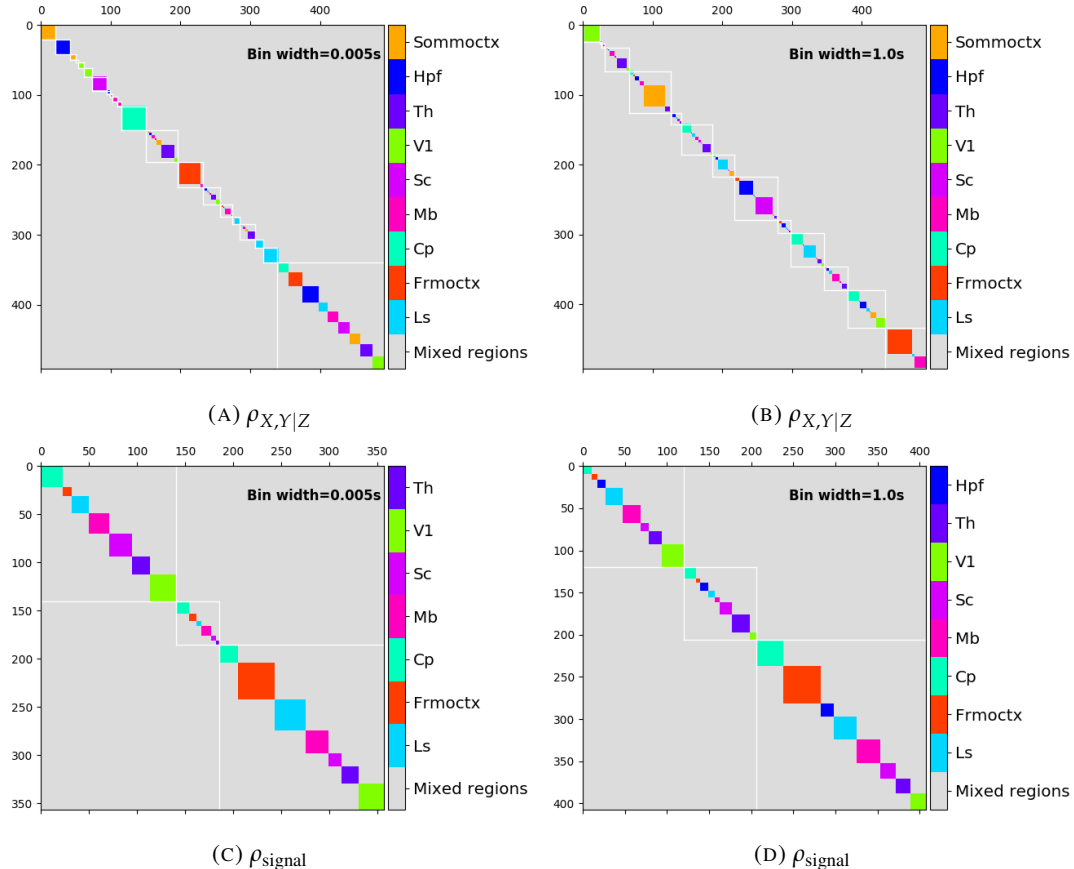


FIGURE 3.13: Matrices showing the regional membership of pairs by colour, and the communities in which those pairs lie. (A-B) Detected communities and regional membership matrix for network based on rectified spike count correlation $\rho_{X,Y|Z}$, using time bin widths of 0.005s and 1s respectively. (C-D) Detected communities and regional membership matrix for network based on rectified signal correlation ρ_{signal} , using time bin widths of 0.005s and 1s respectively.

3.4. Results

1829 based on the spike count correlations $\rho_{X,Y|Z}$ and the signal correlations ρ_{signal} . We noted that
 1830 the community detection on $\rho_{X,Y|Z}$ behaved similarly to the community detection on the total
 1831 correlation. We can see this in figures 3.13a and 3.13b. At very short time bin widths, we
 1832 detect more communities, and those communities often contain cells from one brain region
 1833 only. At longer time bin widths, we detect fewer communities, and those communities tend
 1834 to contain cells from multiple brain regions. When we examine the distance between (or
 1835 similarity between) the anatomical division of the cells, and the detected communities we
 1836 notice that the two clusterings are more similar at shorter time bin widths (see figure 3.14).

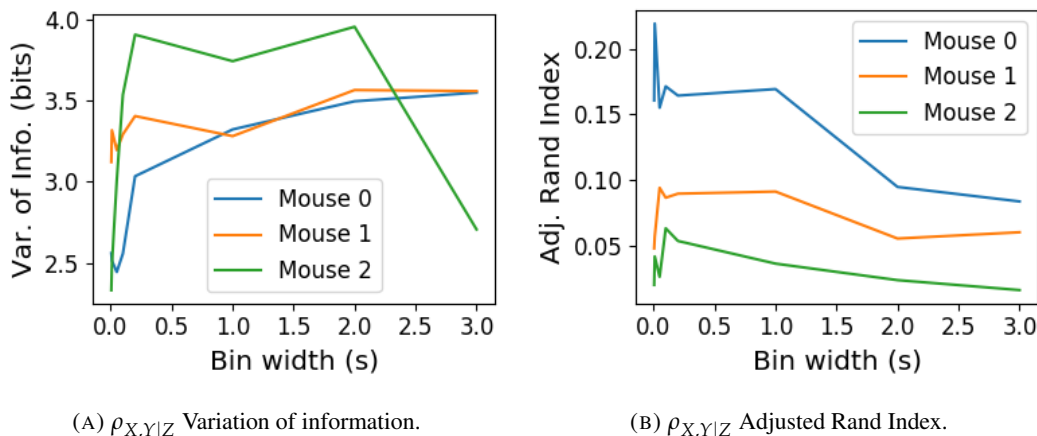


FIGURE 3.14: Distance and similarity measures between the anatomical division of the neurons, and the communities detected in the network based on the spike count correlations $\rho_{X,Y|Z}$. (A) The variation of information is a ‘distance’ measure between clusterings. The distance between the anatomical ‘clustering’ and the community clustering increases as the time bin width increases. (B) The adjusted Rand index is a similarity measure between clusterings. The detected communities become less similar to the anatomical division of the cells as the time bin width increases.

1837 When we applied the network noise rejection and community detection process to the
 1838 networks based on the signal correlations ρ_{signal} we found the number of communities we
 1839 detected reduced with increasing time bin width. But the number of communities detected
 1840 was less than that for the total correlations or the spike count correlations. The communi-
 1841 ties detected always tended to contain cells from multiple regions at both short and long
 1842 timescales (see figures 3.13c and 3.13d). The communities detected bore very little relation
 1843 to the anatomical division of the cells. The adjusted Rand index between the community
 1844 clustering and the anatomical ‘clustering’ is close to zero for every time bin width (see figure
 1845 3.15b). This indicates that the similarity between the clusterings is close to chance. We did
 1846 observe a slight downward trend in the variation of information with increasing bin width
 1847 (see figure 3.15a), but this is more likely due to a decrease in the number of communities

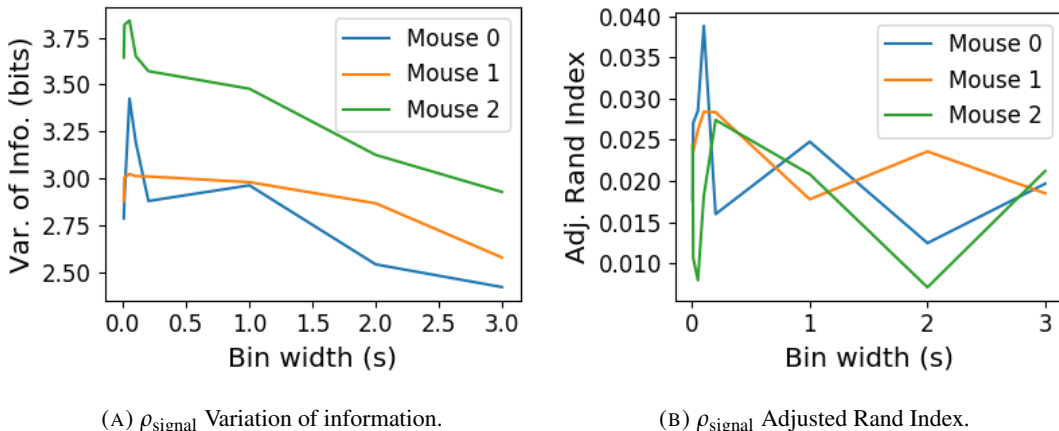
(A) ρ_{signal} Variation of information.(B) ρ_{signal} Adjusted Rand Index.

FIGURE 3.15: Distance and similarity measures between the anatomical division of the neurons, and the communities detected in the network based on the signal correlations ρ_{signal} . (A) The variation of information is a ‘distance’ measure between clusterings. The distance between the anatomical ‘clustering’ and the community clustering increases as the time bin width increases. (B) The adjusted Rand index is a similarity measure between clusterings. The detected communities become less similar to the anatomical division of the time bin width increases.

1848 detected rather than any relationship with anatomy.

1849 We also observed that the network noise rejection process rejected some of the cells
1850 when applied to the network based on the signal correlations. This means that those cells
1851 did not contribute to the additional structure of the network beyond that captured by the
1852 sparse weighted configuration model. This is why the matrices in figures 3.13c and 3.13d are
1853 smaller than their analogues in figures 3.13a and 3.13b.

1854 The communities detected in the signal correlation based networks indicate that there are
1855 groups of cells from different brain regions that react similarly to different activity states.
1856 These groups also exist at all timescales from milliseconds to seconds. This indicates that
1857 there are subsets of cells in each region that respond to activity states regardless of the
1858 timescale of these activities.

1859 3.4.8 Absolute correlations and negative rectified correlations

1860 At the moment, the network noise rejection protocol can only be applied to weighted undi-
1861 rected graphs with non-negative weights. This meant that we had to rectify our correlated
1862 networks before applying the network noise rejection and community detection process. We
1863 wanted to investigate what would happen if instead of rectifying the correlations, we used the
1864 absolute value, or reversed the signs of the correlations and then rectified.

3.4. Results

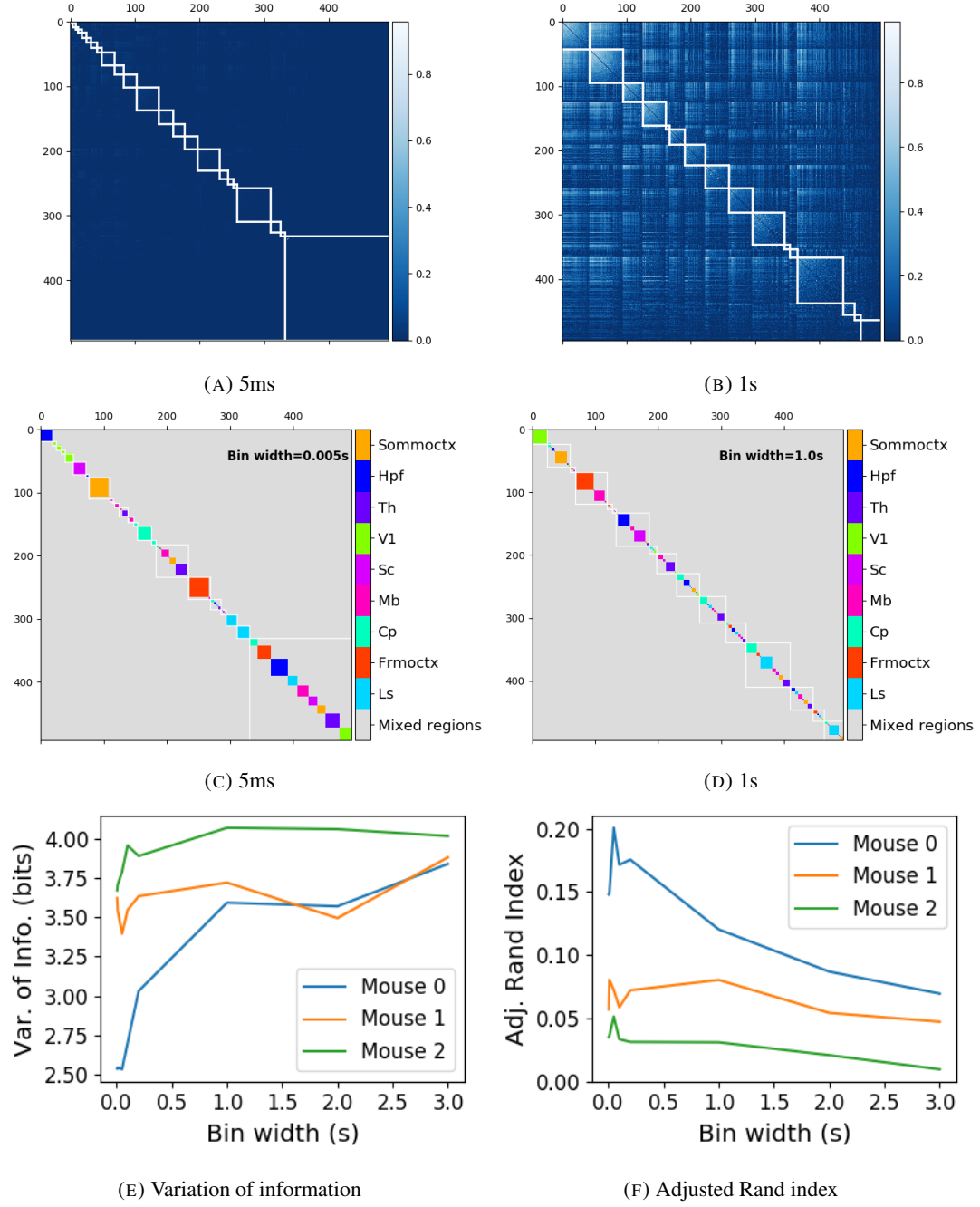


FIGURE 3.16: (A-B) Absolute correlation matrices with detected communities indicated by white lines. These communities are based on the absolute value of the total correlation between each pair of cells. Those entries within a white square indicate that both of those neurons are in the same community. Matrices shown are for 5ms and 1s time bin widths respectively. Main diagonal entries were set to 0. (C-D) Matrices showing the anatomical distribution of pairs along with their community membership. Regional membership is indicated by the colour bar. (E) Variation of information between the anatomical division of the cells, and the detected communities. (F) Adjusted Rand index between the anatomical division, and the detected communities.

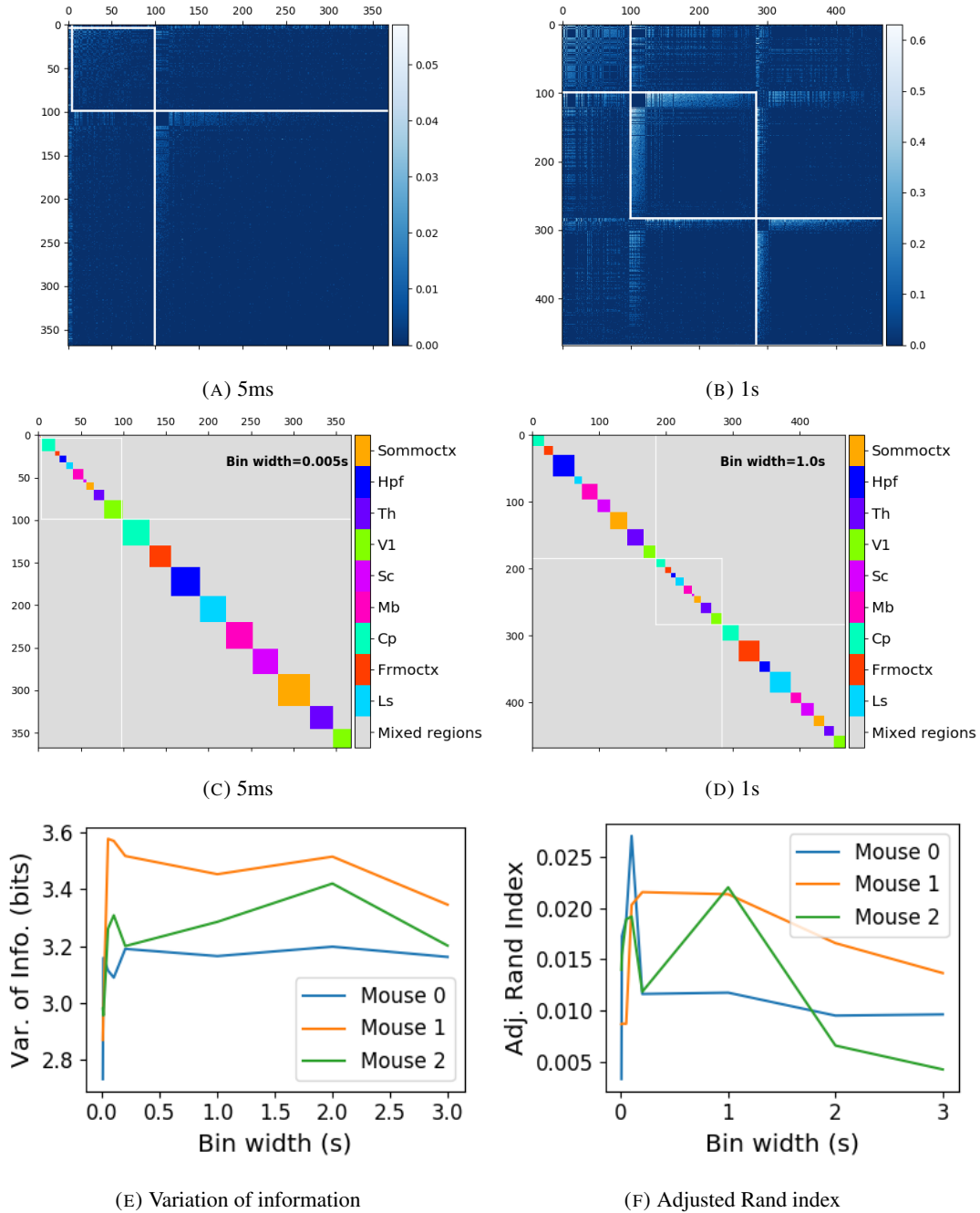


FIGURE 3.17: (A-B) Sign reversed rectified correlation matrices with detected communities indicated by white lines. Those entries within a white square indicate that both of those neurons are in the same community. Matrices shown are for 5ms and 1s time bin widths respectively. Main diagonal entries were set to 0. (C-D) Matrices showing the anatomical distribution of pairs along with their community membership. Regional membership is indicated by the colour bar. (E) Variation of information between the anatomical division of the cells, and the detected communities. (F) Adjusted Rand index between the anatomical division, and the detected communities.

3.5. Discussion

When we used the absolute value of the correlations, we found very similar results to those shown above for the rectified total correlations and the rectified spike count correlations. We detected more communities using shorter bin widths, and these communities were more similar to the brain's anatomy than those communities detected using a longer bin width (see figure 3.16). The only exception being that we detected more communities. This could indicate that we detected both positively and negatively correlated communities, but we haven't done any further investigation so we cannot say for sure.

When we used the sign reversed rectified correlated networks, we tended to find fewer communities. Each community contained cells from many different anatomical regions, at both long and short bin widths (see figures 3.17a, 3.17b, 3.17c, 3.17d). The communities bore little relation to the anatomical distribution of the cells, this can be seen in figure 3.17f, the values close to zero indicate that the similarity between the two clusterings are around chance level. This indicates that there was not much structure in the negatively correlated networks beyond that captured by the sparse weighted configuration model.

3.5 Discussion

It is well established that the brain uses correlated behaviour in neuronal ensembles to represent the information taken in through sensation (Cohen and Maunsell, 2009; Litwin-Kumar, Chacron, and Doiron, 2012; deCharms and Merzenich, 1996). However, most studies that examine the nature of these correlations in-vivo, study an ensemble of cells from only one or two brain regions (Cohen and Kohn, 2011; Wierzynski et al., 2009; Patterson et al., 2014; Girard, Hupé, and Bullier, 2001). Furthermore, recent results have shown that behaviour can drive correlated activity in multiple brain regions, including those not normally associated with motor control (Stringer et al., 2019; Gründemann et al., 2019; Allen et al., 2019). In this study, we utilised one of the newly recorded large datasets containing electrophysiological recordings from multiple brain regions simultaneously. We investigated correlated behaviour in these different brain regions and we investigated correlated behaviour between neurons in different regions, during spontaneous behaviour.

A number of studies have found that the timescale of correlated behaviour induced by a stimulus can be modulated by the stimulus structure and behavioural context. For example, the spike train correlations between cells in weakly electric fish are modulated by the spatial extent of the stimulus (Litwin-Kumar, Chacron, and Doiron, 2012), and neurons in the marmoset primary auditory cortex modulate their spike timing (and therefore correlation) in

1897 response to stimulus features without modulating their firing rate (deCharms and Merzenich,
1898 1996). Furthermore, the width of the time bins over which spike counts are measured has
1899 been shown to have an effect on the magnitude of those correlations (Cohen and Kohn, 2011).
1900 Despite this, very little research has been done comparing correlation measures from the same
1901 dataset at different timescales. We investigated this by varying the time bin width used to bin
1902 spike times into spike counts from as short as 5ms up to 3s.

1903 In order to further investigate the effect of these correlations at different timescales, we
1904 regarded our neuronal ensemble as a weighted undirected graph, where each neuron is rep-
1905 resented by a node, and the weight on each edge is the correlation between the neurons
1906 connected by that edge. We then applied a novel clustering method from network science
1907 (Humphries et al., 2019) to identify communities in these networks. Communities in a net-
1908 work graph refer to sets of nodes that are more strongly connected to each other than the
1909 nodes outside of their set. Another way to put this is to say that the nodes in a community
1910 are more strongly connected than *expected*. What connection strength might be expected is
1911 defined by a null network model. We chose a null network model that matched the sparsity
1912 and total strength of our correlation based data networks. So, if two cells were in the same
1913 community, those cells were more correlated than would be expected given the correlation
1914 strength of their ensemble.

1915 These networks, and the community detection process, were completely agnostic of the
1916 anatomical division of the cells in our ensemble. When we compared the detected commu-
1917 nities with the anatomical division of the cells using distance and similarity measures for
1918 clusterings, we found that the detected communities were more similar to the anatomical
1919 division at shorter timescales. That is, when we used a wider time bin to count spikes, and
1920 computed pairwise correlations with these spike counts, the correlated communities tended to
1921 exist within anatomical regions at shorter timescales, and tended to span anatomical regions
1922 at longer timescales. This could reflect localised functional correlations at short time scales
1923 rippling outwards across brain regions at longer timescales. The brain may be processing
1924 some information quickly locally, and carrying out further, perhaps more detailed, represen-
1925 tation over a longer timescale across many regions using the representations that were just
1926 built locally.

1927 These changes in communities across timescales could also be driven by the anatomy
1928 of the individual cells. For example, it may simply take longer to transmit action potentials
1929 over longer distances, hence correlated activity over longer timescales will exist between

3.5. Discussion

1930 anatomical regions, rather than within. However, the switch to almost exclusively multi-
1931 regional functional networks at 1s bin widths, rather than a mixture of multi-region, and
1932 single-region suggests that the inter-regional correlations either overpower, or inhibit the
1933 local correlations. So there may be more at play than just timescales.

1934 We acknowledged that the region spanning correlated communities that we detected at
1935 longer time scales could exist due to collating activity driven by distinct spontaneous activ-
1936 ities. In order to account for this, we modelled the spike counts as a linear function of the
1937 top 500 principal components of a video of the mouse’s face filmed simultaneously with the
1938 electrophysiological readings. We applied our network noise rejection and community de-
1939 tection process to the weighted undirected networks formed by the spike count correlations
1940 (or noise correlations) and the signal correlations that we calculated using our model. For the
1941 spike count correlation networks, we found much the same results as for the total correlations
1942 as described above. For the signal correlations, the communities detected in these networks
1943 bore little relation to the anatomical division of the cells. Recent findings have shown that
1944 behavioural data accounts for correlations in many brain regions that would otherwise be
1945 dismissed as noise (Stringer et al., 2019), our finding to shows that these correlations are still
1946 governed by the timescale division between local communication and across-region commu-
1947 nication.

1948 There is a lot of room for further investigation based on this research. For a start, the
1949 data that we used here were collected from nine different regions in the mouse brain, but
1950 none of these regions were part of the somatosensory cortex. Given that a mouse experiences
1951 so much of its environment through its sense of smell, some data from this region would be
1952 interesting to investigate. On the same theme, the mice in the experiment from which the
1953 data were collected were headfixed and placed on a rotating ball, but were otherwise behav-
1954 ing spontaneously. Had these mice been exposed to a visual, aural, or olfactory stimulus,
1955 we could have examined the responses of the cells in the brain regions corresponding to vi-
1956 sion, hearing, and olfaction, and compared these responses to the responses from the other
1957 brain regions. Furthermore, we could have investigated the interaction between the sets of
1958 responses.

1959 Another space for further investigation is the community detection. The algorithm that we
1960 used here never detects overlapping communities. But functional communities could indeed
1961 have overlaps. Clustering methods that detect overlapping clusters do exist (Baadel, Thabtah,
1962 and Lu, 2016). Applying one of those algorithms could yield some interesting results. Also,
1963 the community detection algorithm that we used here cannot process graphs with negative

1964 weights, this forced us to separate positive and negative correlations before applying our
1965 network noise rejection and community detections process, or use the absolute value of our
1966 correlations. A community detection algorithm that can work on weighted undirected graphs
1967 with negative weights could yield some interesting results here.

1968 **Chapter 4**

1969 **A simple two parameter distribution
for modelling neuronal activity and
capturing neuronal association**

1972 *Abstract*

1973 Recent developments in electrophysiological technology have lead to an increase in the size
1974 of electrophysiology datasets. Consequently, there is a requirement for new analysis tech-
1975 niques that can make use of these new datasets, while remaining easy to use in practice. In
1976 this work, we fit some one or two parameter probability distributions to spiking data collected
1977 from a mouse exposed to visual stimuli. We show that the Conway-Maxwell-binomial dis-
1978 tribution is a suitable model for the number of active neurons in a neuronal ensemble at any
1979 given moment. This distribution fits these data better than binomial or beta-binomial distribu-
1980 tions. It also captures the correlated activity in the primary visual cortex induced by stimulus
1981 onset more effectively than simply measuring the correlations, at short timescales (< 10ms).
1982 We also replicate the finding of Churchland et al (2010) relating to stimulus onset quenching
1983 neural variability in cortical areas, and we show a correspondence between this quenching
1984 and changes in one of the parameters of the fitted Conway-Maxwell-binomial distributions.

1985 **4.1 Introduction**

1986 Recent advances in electrophysiological technology, such as ‘Neuropixels’ probes (Jun et al.,
1987 2017) have allowed extracellular voltage measurements to be collected from larger numbers
1988 of cells than traditional methods, in multiple brain regions simultaneously, and routinely.
1989 These larger datasets require innovative methods to extract information from the data in a
1990 reasonable amount of time, ‘reasonable’ being subjective in this case.

1991 Theoretically, all the information at any given moment in an electrophysiological dataset
1992 with n neurons could be captured by calculating the probability distribution for every possi-
1993 ble spiking pattern. This would require defining a random variable with 2^n possible values, a
1994 task that quickly becomes impossible as n increases. Attempts at approximating this random
1995 variable often involve measuring pairwise or higher order correlations (Schneidman et al.,
1996 2006; Flach, 2013; Ganmor, Segev, and Schneidman, 2011). But pairwise correlations may
1997 not be enough to characterise instantaneous neural activity (Tkačik et al., 2014). Further-
1998 more, these kinds of models tend to ignore the temporal structure of neuronal data, in favour
1999 of smaller model size, and scalability.

2000 Higher order correlations would be helpful here, but defining and quantifying these cor-
2001 relations can be tricky (Staude, Grün, and Rotter, 2010). If we use the interaction parameters
2002 arising from the exponential family model as measures of higher order correlations, mea-
2003 suring these correlations becomes computationally impractical quite quickly (the number
2004 of ‘three neuron correlations’ to measure scales with $(^n_3)$). In this work, we dispense with
2005 measuring correlations directly, and we attempt to characterise correlated behaviour using a
2006 parameter in statistical model.

2007 In this work, we examined the ability of simple distributions to model the number of
2008 active (spiking) neurons in a neuronal ensemble at any given timepoint. We compared a
2009 little-known distribution named the Conway-Maxwell-binomial distribution to the binomial
2010 distribution and the beta-binomial distribution. The binomial distribution is a probability dis-
2011 tribution over the number of successes in a sequence of independent and identical Bernoulli
2012 trials. The beta-binomial distribution is similar, but allows for a bit more flexibility while still
2013 being a model for heterogeneity. Similar to the binomial and beta-binomial, the Conway-
2014 Maxwell-binomial distribution is a probability distribution over the number of successes in a
2015 series of Bernoulli trials, but allows over- and under-dispersion relative to the binomial dis-
2016 tribution. This distribution should therefore be a good candidate for our purposes. We found
2017 that Conway-Maxwell-binomial distribution was usually the best candidate of the three that

4.2. Data

2018 we examined.

2019 We also observed some interesting changes in the number of active neurons in the primary
2020 visual cortex and hippocampus at stimulus onset and some changes in this activity in the
2021 thalamus which were sustained for the full duration of the stimulus presentation. This let us
2022 know that there were some responses to model.

2023 We found that fitting a Conway-Maxwell-binomial distribution was a better method of
2024 capturing association between neurons than measuring the spike count correlation for the
2025 short time bins that we used (< 10ms).

2026 Finally, we also wanted to investigate parallels between the parameters of the Conway-
2027 Maxwell-binomial distribution and quantities that have been established as relevant to sen-
2028 sory processing. So, we replicated the findings made by Churchland et al. (2010) relating
2029 to a reduction in neural variability at stimulus onset in the macaque cortical regions, but for
2030 data taken from the mouse primary visual cortex. We compared these findings to the values
2031 of the fitted Conway-Maxwell-binomial distribution parameters.

2032 4.2 Data

2033 We used data collected by Nick Steinmetz and his lab ‘CortexLab at UCL’ (Steinmetz, Caran-
2034 dini, and Harris, 2019). The data can be found online ¹ and are free to use for research
2035 purposes.

2036 Two ‘Phase3’ Neuropixels (Jun et al., 2017) electrode arrays were inserted into the brain
2037 of an awake, head-fixed mouse for about an hour and a half. These electrode arrays recorded
2038 384 channels of neural data each at 30kHz and less than $7\mu\text{V}$ RMS noise levels. The sites
2039 are densely spaced in a ‘continuous tetrode’-like arrangement, and a whole array records
2040 from a 3.8mm span of the brain. One array recorded from visual cortex, hippocampus, and
2041 thalamus, the other array recorded from motor cortex and striatum. The data were spike-
2042 sorted automatically by Kilosort and manually by Nick Steinmetz using Phy. In total 831
2043 well-isolated individual neurons were identified.

2044 4.2.1 Experimental protocol

2045 The mouse was shown a visual stimulus on three monitors placed around the mouse at right
2046 angles to each other, covering about ± 135 degrees azimuth and ± 35 degrees elevation.

¹<http://data.cortexlab.net/dualPhase3/>

2047 The stimulus consisted of sine-wave modulated full-field drifting gratings of 16 drift di-
2048 rections ($0^\circ, 22.5^\circ, \dots, 337.5^\circ$) with 2Hz temporal frequency and 0.08 cycles/degree spatial
2049 frequency displayed for 2 seconds plus a blank condition. Each of these 17 conditions were
2050 presented 10 times in a random order across 170 different trials. There were therefore 160
2051 trials with a drifting-grating visual stimulus present, and 10 trials with a blank stimulus.

2052 **4.3 Methods**

2053 **4.3.1 Binning data**

2054 We converted the spike times for each cell into spike counts by putting the spike times into
2055 time bins of a given ‘width’ (in milliseconds). We used time bins of 1ms, 5ms, and 10ms.
2056 We used different time bin widths to assess the impact of choosing a bin width.

2057 **4.3.2 Number of *active* neurons**

2058 To count the number of active neurons in each neuronal ensemble, we split the time interval
2059 for each trial into bins of a given width. We counted the number of spikes fired by each cell
2060 in each bin. If a cell fired *at least* one spike in a given bin, we regarded that cell as active in
2061 that bin. We recorded the number of active cells in every bin, and for the purposes of further
2062 analysis, we recorded each cell’s individual spike counts.

2063 It should be noted that when we used a bin width of 1ms, the maximum number of
2064 spikes in any bin was 1. For the wider time bins, some bins had spike counts greater than
2065 1. Consequently when using a bin width of 1ms, the number of active neurons and the total
2066 spike count of a given bin were identical. But for wider bin widths, the total spike count was
2067 greater than the number of active neurons.

2068 So for the 1ms bin width, the activity of a neuron and the number of spikes fired by that
2069 neuron in any bin can be modelled as a Bernoulli variable. But for wider time bins, only the
2070 activity can be modelled in this way.

2071 **4.3.3 Moving windows for measurements**

2072 When taking measurements (e.g. moving average over the number of active neurons) or
2073 fitting distributions (eg. the beta binomial distribution) we slid a window containing a certain
2074 number of bins across the data, and made our measurements at each window position. For
2075 example, when analysing 1ms bin data, we used a window containing 100 bins, and we slid

4.3. Methods

Bin width (ms)	Window size (bins)	Window size (ms)	Windows per trial
1ms	100	100ms	296
5ms	40	200ms	286
10ms	40	400ms	266

TABLE 4.1: Details of the different bin width and analysis window sizes used when binning spike times, and analysing those data.

2076 the window across the time interval for each trial moving 10 bins at a time. So that for
2077 3060ms of data, we made 296 measurements.

2078 For the 5ms bin width data, we used windows containing 40 bins, and slid the window 2
2079 bins at a time when taking measurements.

2080 For the 10ms bin width data, we used windows containing 40 bins, and slid the window
2081 1 bin at a time when taking measurements (see table 4.1 for concise details).

2082 By continuing to use windows containing 40 bins, we retained statistical power but sac-
2083 rificed the number of measurements taken.

2084 There was an interval between each trial with a grey image in place of the moving bar
2085 stimulus. This interval varied in time. But we included some of this interval when recording
2086 the data for each trial. We started recording the number of active neurons, and the number
2087 of spikes from each neuron from 530ms before each trial until 1030ms after each trial. This
2088 way, we could see the change in our measurements at the onset of a stimulus and the end of
2089 stimulus presentation.

2090 As mentioned in section 4.3.2, we recorded the number of active neurons in each bin, and
2091 the spike count for each neuron in each bin. The measurements we took using these data in
2092 each window were as follows:

2093 **Moving average** The average number of active cells in each window.

2094 **Moving variance** The variance of the number of active cells in each window.

2095 **Average correlation** We measured the correlation between the spike counts of each pair of
2096 cells in the ensemble, and took the average of these measurements.

2097 **Binomial p** We fitted a binomial distribution to the data in each window and recorded the
2098 fitted probability of success, p in each case.

2099 **Beta-binomial α, β** We fitted a beta-binomial distribution to the data in each window, and
2100 recorded the values of the fitted shape parameters, α and β , of each distribution.

2101 **Conway-Maxwell-binomial distribution p, ν** We fitted a Conway-Maxwell-binomial dis-
2102 tribution to the data in each window, and recorded the fitted values of p and ν for each
2103 distribution.

2104 **Log-likelihoods** We also recorded the log-likelihood of each of the fitted distributions for
2105 each window.

2106 **4.3.4 Fano factor**

The *Fano factor* of a random variable is defined as the ratio of the variable's variance to its mean.

$$F = \frac{\sigma^2}{\mu} \quad (4.1)$$

2107 We measured the Fano factor of the spike count of a given cell by measuring the mean and
2108 variance of the spike count across trials, and taking the ratio of those two quantities. When
2109 calculated in this way the Fano factor can be used as a measure of neural variability that
2110 controls for changes in the firing rate. This is similar to the calculation used in (Churchland
2111 et al., 2010).

2112 **4.3.5 Probability Distributions suitable for modelling ensemble activity**

2113 We present here three different probability distributions that could be suitable to model the
2114 number of active neurons in an ensemble. Each distribution has the set $\{0, \dots, n\}$ as its sup-
2115 port, where n is the number of neurons in the ensemble. These are simple distributions with
2116 either two or three parameters each. However, we regard n as known when using these dis-
2117 tributions for modelling, so in effect each distribution has either one or two free parameters.

2118 **Association**

2119 *Association* between random variables is similar to the correlation between random variables
2120 but is more general in concept. The correlation coefficient is a measure of association; and
2121 association doesn't necessarily have a mathematical definition like correlation does. Essen-
2122 tially, an association between two random variables is a dependency of any kind. Positively
2123 associated variables tend to take the same value, and negatively associated variables tend to
2124 take different values. In this research, we work with probability distributions of the num-
2125 ber of successes in a set of Bernoulli trials. These Bernoulli variables may or may not be
2126 associated.

4.3. Methods

2127 A probability distribution over the number of successes in n Bernoulli trials, where the
2128 Bernoulli variables may be associated, could constitute a good model for the number of active
2129 neurons in an ensemble of n neurons. As long as the observation period is divided into time
2130 bins short enough so that any neuron is unlikely to fire more than spike in any time bin.

2131 **Binomial distribution**

The binomial distribution is a two parameter discrete probability distribution that can be thought of as a probability distribution the number of successes from n independent Bernoulli trials, each with the same probability of success. The parameters of the binomial distribution are n the number of trials, and $0 \leq p \leq 1$, the probability of success for each of these trials. A random variable with the binomial distribution can take values from $\{0, \dots, n\}$.

The probability mass function of the distribution is

$$P(k; n, p) = \binom{n}{k} p^k (1-p)^{n-k} \quad (4.2)$$

2132 As a model for the activity of a neuronal ensemble, the main problem with the binomial
2133 distribution is that it treats each neuron, represented as a Bernoulli trial, as independent. It is
2134 well known that neurons are not independent, and that correlated behaviour between neurons
2135 is vital for representing sensory information (Cohen and Maunsell, 2009). The binomial dis-
2136 tribution falls short in this regard, but it is useful as performance benchmark when assessing
2137 the performance of other models.

2138 **Beta-binomial distribution**

2139 The beta distribution is the conjugate distribution of the binomial distribution. The beta-
2140 binomial distribution is the combination of the beta distribution and the binomial distribution,
2141 in that the probability of success for the binomial distribution is sampled from the beta dis-
2142 tribution. This allows the beta-binomial distribution to capture some over dispersion relative
2143 to the binomial distribution.

The beta-binomial distribution is a three parameter distribution, n the number of Bernoulli trials, and $\alpha \in \mathbb{R}_{>0}$ and $\beta \in \mathbb{R}_{>0}$ the shape parameters of the beta distribution. The probability mass function for the beta-binomial distribution is

$$P(k; n, \alpha, \beta) = \binom{n}{k} \frac{B(k + \alpha, n - k + \beta)}{B(\alpha, \beta)} \quad (4.3)$$

2144 where $B(\alpha, \beta)$ is the beta function.

This probability distribution can be reparametrised in a number of ways. One of which defines new parameters π and ρ by

$$\pi = \frac{\alpha}{\alpha + \beta} \quad (4.4)$$

$$\rho = \frac{1}{\alpha + \beta + 1} \quad (4.5)$$

2145 This reparametrisation is useful because π acts as a location parameter analogous to the p
2146 parameter of a binomial distribution. A value of $\rho > 0$ indicates over-dispersion relative to a
2147 binomial distribution.

2148 As a model for the activity of a neuronal ensemble, the beta-binomial distribution is
2149 more suitable than a binomial distribution because the over-dispersion of the beta-binomial
2150 distribution can be used to model positive association between the neurons. An extreme
2151 example of this over-dispersion/positive association can be seen in figure 4.1b. In this figure,
2152 the neurons are positively associated and so tend to take the same value, consequently the
2153 probability mass of the beta-binomial distribution builds up close to $k = 0$ and $k = n$. It is
2154 worth noting that the location parameter for each distribution has the same value, $p = \pi =$
2155 0.5.

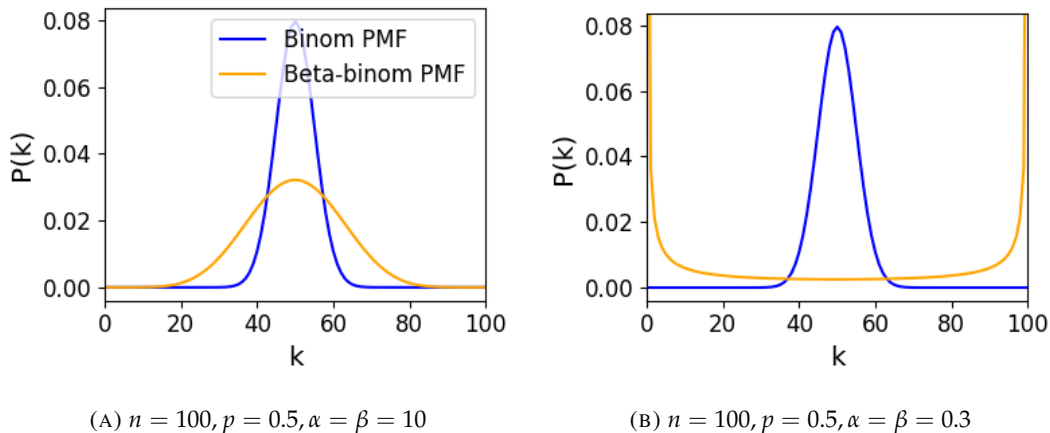


FIGURE 4.1: Figures showing the over-dispersion possible for a beta-binomial distribution relative to a binomial distribution. Parameters are shown in the captions.

2156 **Conway-Maxwell-binomial distribution**

2157 The Conway-Maxwell-binomial distribution (COMb distribution) is a three parameter generalisation of the binomial distribution that allows for over dispersion and under dispersion

4.3. Methods

relative to the binomial distribution. The parameters of the distribution are n the number of Bernoulli trials, and two shape parameters $0 \leq p \leq 1$, and $\nu \in \mathbb{R}$.

The probability mass function of the COMb distribution is

$$P(k; n, p, \nu) = \frac{1}{S(n, p, \nu)} \binom{n}{k}^{\nu} p^k (1-p)^{n-k} \quad (4.6)$$

where

$$S(n, p, \nu) = \sum_{j=0}^n \binom{n}{j}^{\nu} p^j (1-p)^{n-j} \quad (4.7)$$

The only difference between this PMF and the PMF for the standard binomial is the introduction of ν and the consequent introduction of the normalising function $S(n, p, \nu)$.

Indeed, if $\nu = 1$ the COMb distribution is identical to the binomial distribution with the same values for n and p . We can see in figure 4.2d that the KL-divergence $D_{KL}(P_{COMb}(n, p, \nu) || P_{Bin}(n, p)) = 0$ along the line where $\nu = 1$. The analytical expression for the divergence is

$$D_{KL}(P_{COMb}(k; n, p, \nu) || P_{Bin}(k; n, p)) = (\nu - 1) E_{P_{COMb}(k; n, p, \nu)} \left[\log \binom{n}{k} \right] \quad (4.8)$$

$$- \log S(n, p, \nu) \quad (4.9)$$

At $\nu = 1$, we have $S(n, p, 1)$ which is just the sum over the binomial PMF, so $S(n, p, 1) = 1$ and therefore $D_{KL}(P_{COMb}(n, p, \nu) || P_{Bin}(n, p)) = 0$.

If $\nu < 1$ the COMb distribution will exhibit over-dispersion relative to the binomial distribution. If $p = 0.5$ and $\nu = 0$ the COMb distribution is the discrete uniform distribution, and if $\nu < 0$ the mass of the COMb distribution will tend to build up near $k = 0$ and $k = n$. This over-dispersion represents positive association in the Bernoulli variables. An example of this over-dispersion can be seen in figure 4.2b.

If $\nu > 1$ the COMb distribution will exhibit under-dispersion relative to the binomial distribution. The larger the value of ν the more probability mass will build up at $n/2$ for even n , or at $\lfloor n/2 \rfloor$ and $\lceil n/2 \rceil$ for odd n . This under-dispersion represents negative association in the Bernoulli variables. An example of this under-dispersion can be seen in figure 4.2a.

It should be noted that the p parameter of the COMb distribution does not correspond to the mean of the distribution, as is the case for the binomial p parameter, and beta-binomial π parameter. That is, the COMb p parameter is not a location parameter. An illustration of this can be seen in figure 4.2c. This is because an interaction between the p and ν parameters skews the mean. There is no analytical expression for the mean of the COMb distribution.

ν	Relative dispersion	Association between neurons/variables
< 1	over	positive
1	none	none
> 1	under	negative

TABLE 4.2: Relative dispersion of the COMb distribution, and association between Bernoulli variables as represented by the value of the ν parameter.

2179 Since the COMb distribution has the potential to capture positive and negative associa-
2180 tions between the neurons/Bernoulli variables, it should be an excellent candidate for mod-
2181 elling the number of active neurons in a neuronal ensemble.

2182 We wrote a dedicated Python package to enable easy creation and fitting of COMb dis-
2183 tribution objects. The format of the package imitates the format of other distribution objects
2184 from the `scipy.stats` Python package. The COMb package can be found here:

2185 https://github.com/thomasjdelaney/Conway_Maxwell_Binomial_Distribution

2186 4.3.6 Fitting

2187 We fitted binomial, beta-binomial, and Conway-Maxwell-binomial (COMb) distributions to
2188 the neural activity in each of the overlapping windows covering each trial. To fit the distribu-
2189 tions we minimised the appropriate negative log likelihood function using the data from the
2190 window.

There is an analytical solution for maximum likelihood estimate of the binomial distribu-
tion's p parameter.

$$\hat{p} = \frac{1}{n} \sum_{i=1}^N k_i \quad (4.10)$$

2191 We minimised the negative log likelihood function of the beta-binomial distribution nu-
2192 merically. We calculated the negative log likelihood for a sample directly, by taking the sum
2193 of the log of the probability mass function for each value in the sample. We minimised the
2194 negation of that function using the `minimise` function of the `scipy.optimize` Python
2195 package.

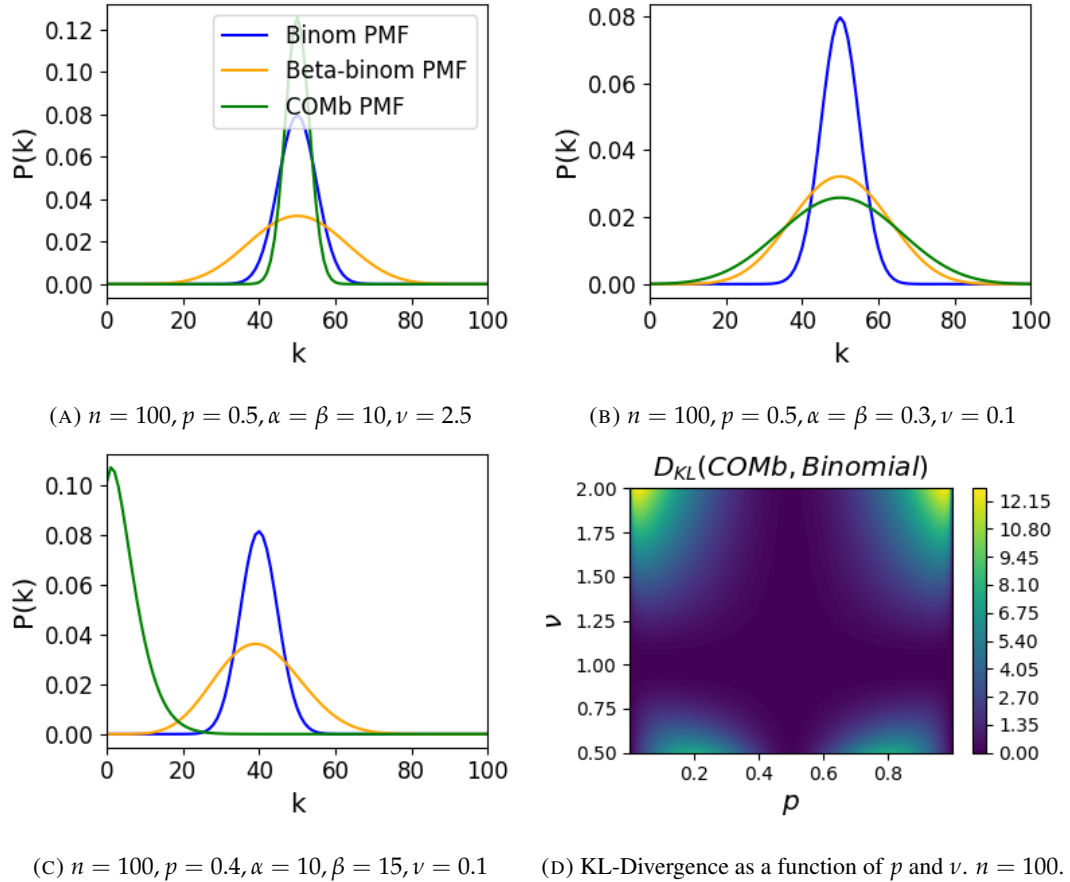


FIGURE 4.2: Figures showing (A) the under-dispersion and (B) over-dispersion permitted by the COMb distribution relative to a binomial distribution. (C) illustrates that the p parameter of the COMb distribution does not correspond to the mean of the distribution, as it does for the binomial and beta-binomial distributions. (D) shows a heatmap for the value of the Kullback-Liebler divergence between the COMb distribution and the standard binomial distribution with same value for n , as a function of p and ν . The point of this figure is to give the reader a sense of how the values of p and ν influence the difference between the COMb distribution and the binomial distribution. The divergence is smallest when $\nu \approx 1$, or when $p \approx 0.5$. When $\nu = 1$, the PMF for the COMb distribution is the same as the PMF for the binomial distribution. When $p = 0.5$ the mass of the distribution is centred around $n/2$ for both the COMb and the binomial distribution. The difference between the two distributions is controlled by the ν parameter. The further the p and ν parameters are from 0.5 and 1 respectively, the greater the difference between the COMb distribution and the binomial distribution. Parameters for all figures are shown in the captions.

The log likelihood function of the COMb distribution given some sample $\{k_1, \dots, k_N\}$ is

$$\ell(p, \nu | k_1, \dots, k_N) = N [n \log(1 - p) - \log S(n, p, \nu)] \quad (4.11)$$

$$+ \log \frac{p}{1 - p} \sum_{i=1}^N k_i \quad (4.12)$$

$$+ \nu \sum_{i=1}^N \log \binom{n}{k_i} \quad (4.13)$$

2196 We minimised the negation of this function using numerical methods. More specifically, we
2197 used the `minimise` function of the `scipy.optimize` Python package.

2198 **4.3.7 Goodness-of-fit**

2199 After fitting, we measured the goodness-of-fit of each model/distribution with their log like-
2200 lihood. We calculated this directly using the `logpmf` functions of the distribution objects in
2201 Python.

2202 **4.4 Results**

2203 We defined a neuron as *active* in a time bin if it fires at least one spike during the time interval
2204 covered by that bin. We measured the number of active neurons in the primary visual cortex
2205 of a mouse in 1ms bins across 160 trials of a moving bar visual stimulus. We then slid a
2206 100ms window across these 1ms bins taking measurements, and fitting distributions along
2207 the way. We did the same for neurons in the thalamus, hippocampus, striatum, and motor
2208 cortex. We repeated the analysis for 5ms time bins with 40 bin windows, and 10ms time bins
2209 with 40 bin windows.

2210 **4.4.1 Increases in mean number of active neurons and variance in number of
2211 active neurons at stimulus onset in some regions**

2212 We measured the average number of active neurons, and the variance of the number of active
2213 neurons in a 100ms sliding window starting 500ms before stimulus onset until 1000ms after
2214 stimulus onset. We found differences in the response across regions. There were no observed
2215 changes in response to the stimulus in the motor cortex or the striatum. The changes in the
2216 other regions are detailed below.

4.4. Results

2217 Primary visual cortex

2218 We found a transient increase in both the average and variance of the number of active neu-
2219 rons at stimulus onset, followed by a fall to pre-stimulus levels, followed by another transient
2220 increase (see figure 4.3). The oscillation in both of these measurements appear to reflect the
2221 frequency of the stimulus (see Data section 4.2.1), and it is known that stimulus structure can
2222 influence response structure(Litwin-Kumar, Chacron, and Doiron, 2012). We see a similar
2223 but lower amplitude oscillation at the end of the stimulus presentation.

2224 Hippocampus

2225 In the hippocampus we observed a transient increase in the average number of active neurons
2226 and in the variance of the number of active neurons at stimulus onset (see figure 4.4). The
2227 increase lasted about 125ms, and the subsequent fall to baseline took the a similar amount of
2228 time.

2229 Thalamus

2230 In the thalamus we observed a transient increase in the both the average and variance of
2231 the number of active neurons on stimulus onset, followed by a fall to pre-stimulus levels,
2232 followed by a sustained increase until the stimulus presentation ends.

2233 As one you might expect for a visual stimulus, the change in the average number of active
2234 neurons was greatest in the primary visual cortex. In this region, this quantity doubled on
2235 stimulus onset. In contrast, in the hippocampus and the thalamus, the average number of
2236 active neurons only increased by a fraction of the unstimulated baseline value. The duration
2237 of the response in V1 and the hippocampus at stimulus onset was 300 – 400ms, but the
2238 response in the thalamus appeared to last for the duration of stimulus presentation. The V1
2239 also showed a change in the average number of active neurons at stimulus end. The change
2240 was similar to that observed at stimulus onset, but smaller in magnitude (see figures 4.3, 4.4,
2241 and 4.5)

2242 4.4.2 Conway-Maxwell-binomial distribution is usually a better fit than bino- 2243 mial or beta-binomial

2244 Since the Conway-Maxwell-binomial distribution has not been fitted to neuronal data before,
2245 it is not clear that it would be a better fit than the binomial or beta-binomial distributions.
2246 In order to find out which parametric distribution was the best fit for the largest proportion

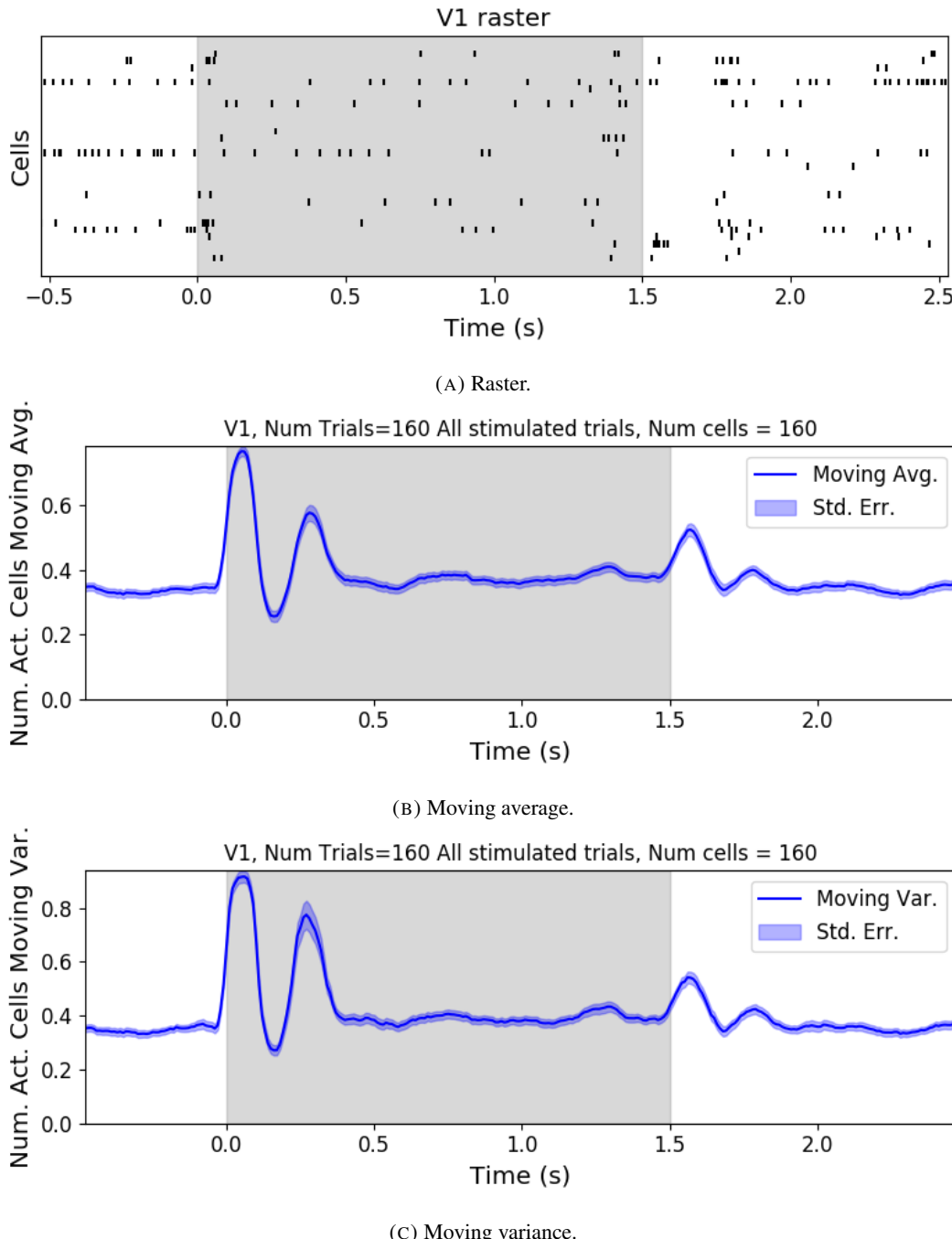


FIGURE 4.3: (A) Raster plot showing the spikes fired by 33 randomly chosen neurons in the primary visual cortex. (B-C) (B) average and (C) variance of the number of active neurons, measured using a sliding window 100ms wide, split into 100 bins. The midpoint of the time interval for each window is used as the timepoint (x-axis point) for the measurements using that window. The grey shaded area indicates the presence of a visual stimulus. The opaque line is an average across the 160 trials that included a visual stimulus of any kind. We can see a transient increase in the average number of active neurons and the variance of this number, followed by a fluctuation and another increase.

4.4. Results

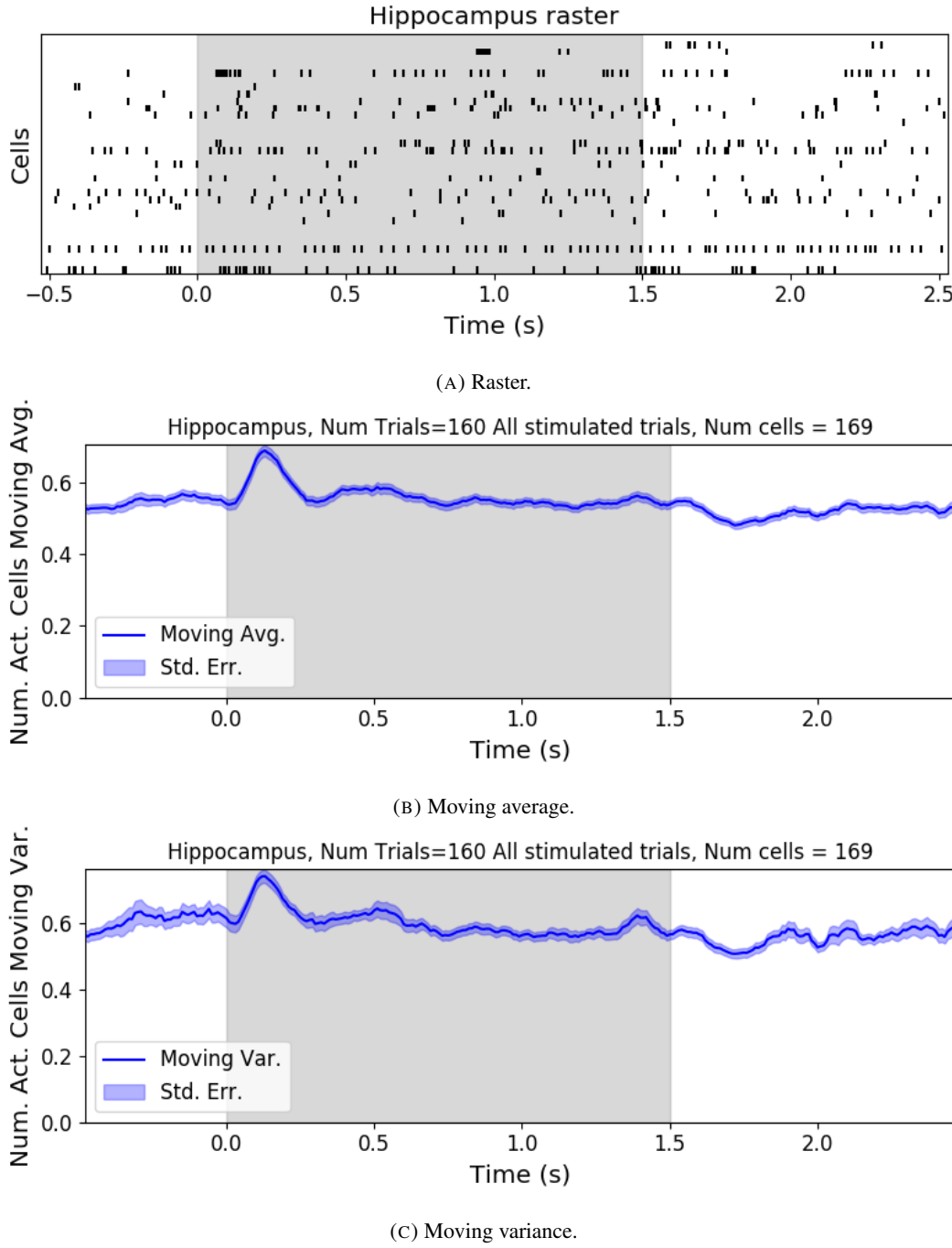


FIGURE 4.4: (A) Raster plot showing the spikes fired by 33 randomly chosen neurons in the hippocampus. (B-C) (B) average and (C) variance of the number of active neurons, measured using a sliding window 100ms wide, split into 100 bins. The midpoint of the time interval for each window is used as the timepoint (x-axis point) for the measurements using that window. The grey shaded area indicates the presence of a visual stimulus. The opaque line is an average across the 160 trials that included a visual stimulus of any kind. We can see a transient increase in the average number of active neurons and the variance of this number at stimulus onset.

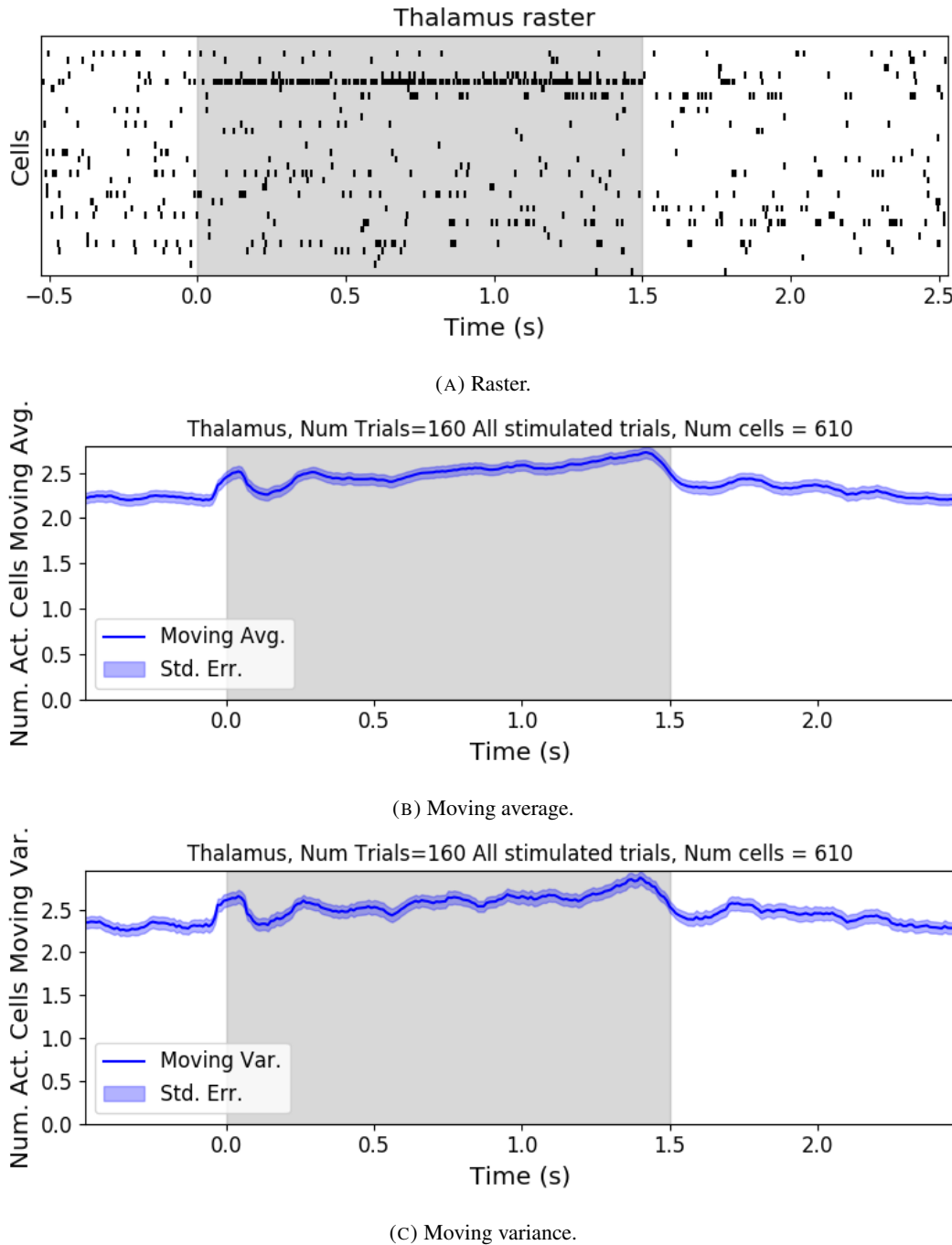
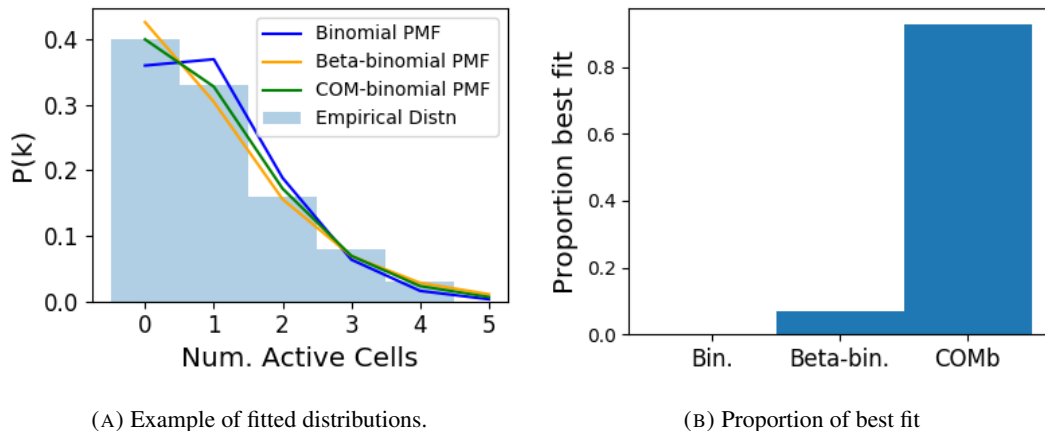


FIGURE 4.5: (A) Raster plot showing the spikes fired by 33 randomly chosen neurons in the thalamus. (B-C) (B) average and (C) variance of the number of active neurons, measured using a sliding window 100ms wide, split into 100 bins. The midpoint of the time interval for each window is used as the timepoint (x-axis point) for the measurements using that window. The grey shaded area indicates the presence of a visual stimulus. The opaque line is an average across the 160 trials that included a visual stimulus of any kind. We can see an immediate increase at stimulus onset, a subsequent fall, and another sustained increased until the stimulus presentation ends.

4.4. Results

of our data, we fit a binomial, a beta-binomial, and a Conway-Maxwell-binomial (COMb) distribution to each window for each bin width, and each region. Then we assessed the goodness-of-fit of each distribution by calculating the log-likelihood of each fitted distribution using the associated sample. We measured the proportion of samples for which each distribution was the best fit, for each bin width value and each region.

We found that the COMb distribution was the best fit for most of the samples regardless of bin width or region. The bin width had an effect on the number of samples for which the COMb distribution was the best fit. The results are summarised in table 4.3. For a bin width of 1ms, the COMb distribution was the best fit for over 90% of samples, the beta-binomial distribution was the best fit for less than 10% of samples, and the binomial distribution was the best fit for less than 1% of samples, across regions. For 5ms bins, the COMb distribution was the best fit for 70 – 80% of samples, the beta-binomial distribution was the best fit for 20 – 30% of the samples, and again the binomial distribution was the best fit for less than 1% of samples, across regions. Finally, for 10ms bins, the COMb distribution was the best fit for 53 – 80% of samples, the beta-binomial distribution was the best fit for 20 – 47% of the samples, and the binomial distribution was the best fit for less than 0.1% of samples, across regions.



(A) Example of fitted distributions.

(B) Proportion of best fit

FIGURE 4.6: (A) An example of the binomial, beta-binomial, and Conway-Maxwell-binomial distributions fitted to a sample of neural activity. The Conway-Maxwell-binomial distribution is the best fit in this case. The histogram shows the empirical distribution of the sample. The probability mass function of each distribution is indicated by a different coloured line. (B) Across all samples in all trials, the proportion of samples for which each fitted distribution was the best fit. The Conway-Maxwell-binomial distribution was the best fit for 93% of the samples taken from V1 using a bin width of 1ms.

Bin Width (ms)	Binomial	Beta-binomial	COMb
1ms	< 1%	< 10%	> 90%
5ms	< 0.1%	20 – 30%	70 – 80%
10ms	< 0.1%	20 – 47%	53 – 80%

TABLE 4.3: Proportion of samples for which each distribution was the best fit, grouped by bin width. The COMb distribution is the best fit most of the time.

2264 **4.4.3 Conway-Maxwell-binomial distribution captures changes in association
2265 at stimulus onset**

2266 We fit a Conway-Maxwell-binomial (COMb) distribution to the number of active neurons in
2267 the 1ms time bins in a 100ms sliding window. We also measured the correlation coefficient
2268 between the spike counts of all possible pairs of neurons, and took the average of these
2269 coefficients. We did this for all the trials with a visual stimulus. We observed a reduction in
2270 the COMb distribution's ν parameter at stimulus onset from around 1 to between 0 and 1 (see
2271 figure 4.7a). A value of ν less than 1 indicates positive association between the neurons (see
2272 section 4.3.5). We might expect to see this positive association reflected in the correlation
2273 coefficients, but this is not the case. We see no change in the time series of average correlation
2274 measures at stimulus onset.

2275 This may be due to the very short time bin we used in this case. We know that using small
2276 time bins can artificially reduce correlation measurements (Cohen and Kohn, 2011). In this
2277 case, fitting the COMb distribution may be a useful way to measure association in a neuronal
2278 ensemble over very short timescales (< 10ms).

2279 **4.4.4 Replicating stimulus related quenching of neural variability**

2280 Churchland et al. (2010) inspected the effect of a stimulus on neural variability. One of the
2281 measures of neural variability that they employed was the Fano factor of the spike counts of
2282 individual cells (see section 4.3.4). They found a reduction in neural variability as measured
2283 by the Fano factor in various cortical areas in a macaque at the onset of various visual stimuli,
2284 or a juice reward (Churchland et al., 2010).

2285 We measured the Fano factor of the spike count of each cell in each brain region, during
2286 each trial. We measured the mean and standard error of these Fano factors from 500ms
2287 before stimulus onset until 1000ms after stimulus end. For the primary visual cortex, we
2288 found a transient reduction in the Fano factor immediately after stimulus onset. We used
2289 a Mann-Whitney U test to check that the Fano factors measured in a window starting at

4.4. Results

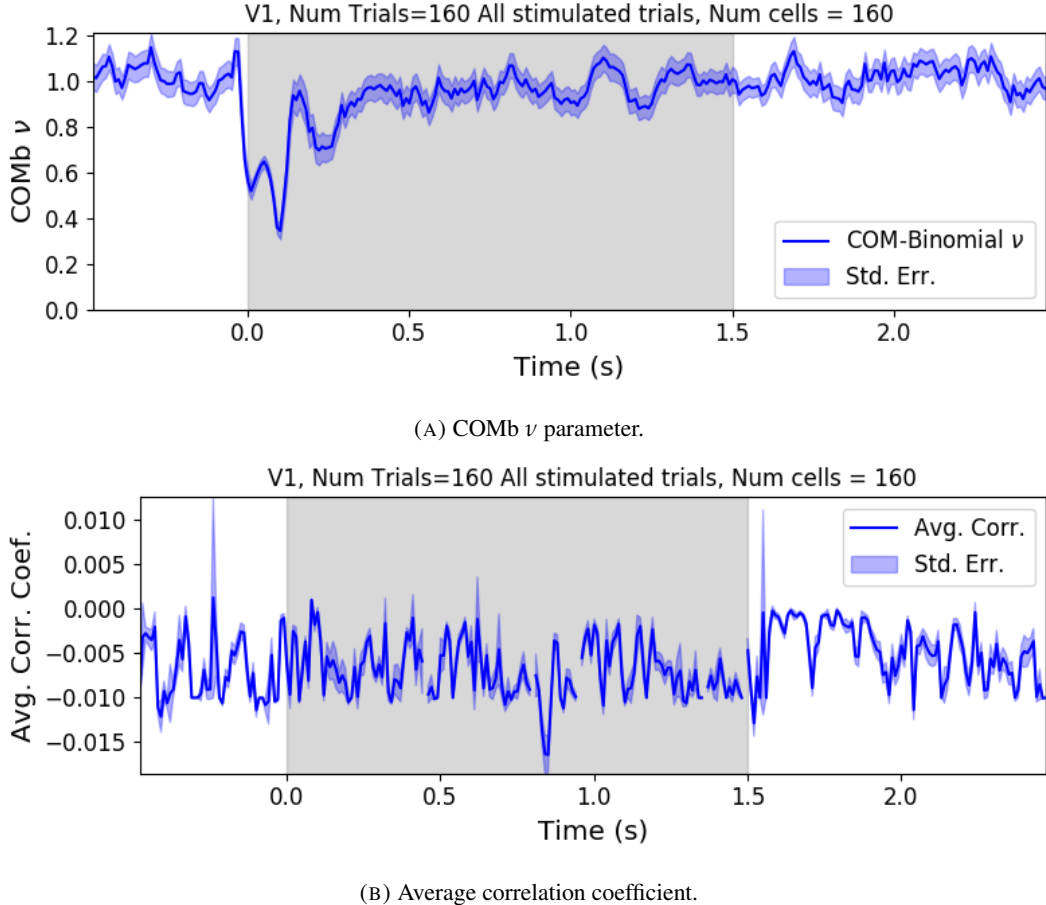


FIGURE 4.7: (A) We fit a Conway-Maxwell-binomial distribution to the number of active neurons in 1ms time bins of a 100ms sliding window. We did this for all trials with a visual stimulus and took the average across those trials. We see a transient drop in value for the distribution’s ν parameter at stimulus onset. This shows an increase in positive association between the neurons. (B) We measured the correlation coefficient between the spike counts of all possible pairs of neurons in the same sliding window. The took the average of those coefficients. We also did this for every visually stimulated trial, and took the average across trials. The increase in positive association is not reflected with an increase in average correlation.

stimulus onset and ending 100ms later were significantly lower than the factors measured in a window ending at stimulus onset ($p < 0.001$, see figure 4.8a). We did not get this statistically significant result in any other region.

Our findings agree with those of Churchland et al. for the primary visual cortex. However Churchland also found a reduction in the Fano factor in the dorsal premotor cortex (PMd) at stimulus onset. Our measurements from the mouse motor cortex show no change at stimulus onset (see figure 4.8b). This could indicate some difference in the functionality of the motor cortex in a macaque and the motor cortex of a mouse.

Similar to these findings in the Fano factor, we found a reduction in the ν parameter of the COMB distribution on stimulus onset in V1 (figure 4.7a) and in no other region from

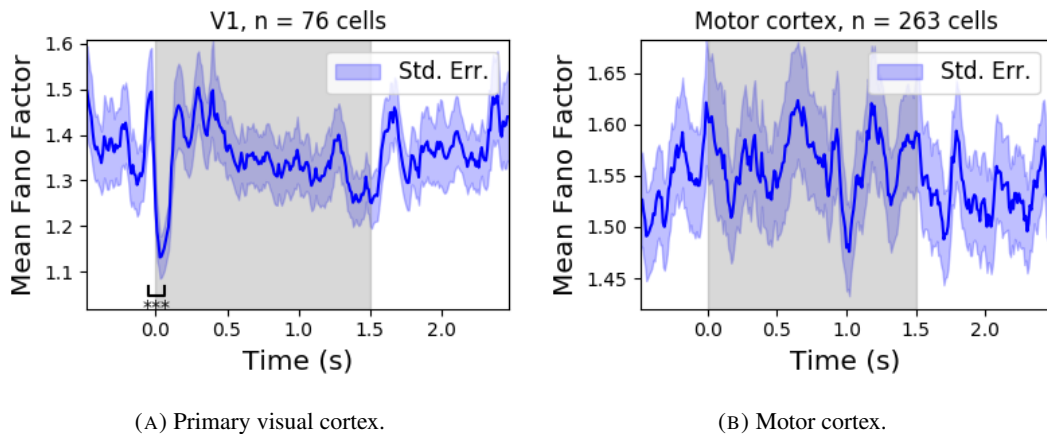


FIGURE 4.8: (A) The mean Fano factor of the spike counts of the cells in the primary visual cortex. Means were taken across cells first, then across trials. There was a significant decrease in the Fano factors immediately after stimulus onset. (B) The mean Fano factor of the spike counts of the cells in the motor cortex. No significant change in measurements at any point.

which we had data. Specifically, the ν parameter reduced from around 1, to between 1 and 0. This represents a change from no association between the neurons, to a positive association. It is possible that this positive association may be responsible for the reduction in the Fano factor.

4.4.5 Effects of wider bin sizes

Using a greater bin width (10ms) affected the scale and shape of the most of the measurements taken (described in section 4.3.3). The average correlation coefficient is the exception to this. The 10ms bin width is still so small that the average correlation coefficient was also small (similar scale as figure 4.7b).

Using the greater bin width acted as a low pass filter on the other measurements taken and the parameters of the fitted distributions. For example compare figure 4.7a to figure 4.9a. Note also that the ν parameter varies between 0.6 and 0.2 when using the 10ms bin width. This indicates some positive association between the neurons at all times, even when not stimulated or when adapted to the stimulus. This may be caused by the wider bin width resulting in more neurons classified as active. The change in association at stimulus onset is still captured by the change in the ν parameter.

The mean number of active neurons was about 10 times greater for a 10ms bin width compared to a 1ms bin width. The variance in the number of active neurons was also greater for the wider bin width. This caused a change in the scale of the Fano factor (see figure 4.9b compared to figure 4.8a). Also, the reduction in the mean Fano factor at stimulus onset is not

4.5. Discussion

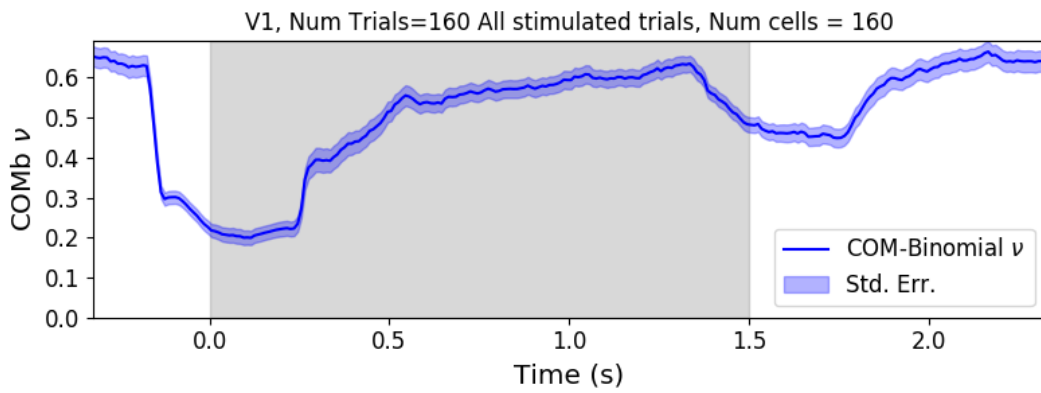
2320 significant when using the 10ms bin width (Mann-Whitney U test, $p = 0.07$). This is likely
2321 due to greater variance in the Fano factors of the individual cells. Bear in mind that we are
2322 using the activity in each bin (either 0 or 1) rather than the actual spike counts in each bin.
2323 When using a 1ms bin width, there is no difference between the spike count and the activity
2324 but when using a wider bin width, there may be more than one spike per bin.

2325 4.5 Discussion

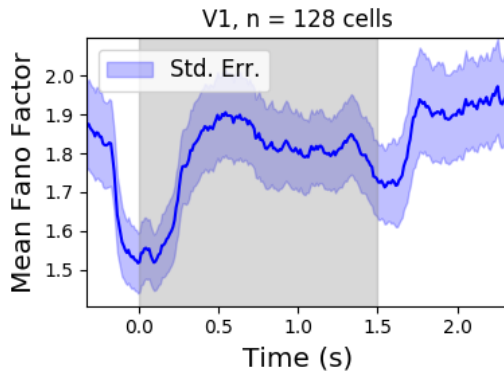
2326 Our aim in this research was to develop a new statistical method for analysing the activity
2327 of a neuronal ensemble at very short timescales. We wanted our method to use information
2328 taken from the whole ensemble, but we also wanted the method to be quick and easy to
2329 implement. It is likely that analysis methods with these characteristics will become valuable
2330 as electrophysiological datasets include readings from more cells over longer time periods. In
2331 this case, we used the number of active, or spiking, neurons in a very short time bin (< 10ms)
2332 as a measure of ensemble activity.

2333 First of all, we showed that there were changes in response that we could model at these
2334 very short time scales in some of the brain regions from which we had recordings. We ob-
2335 served changes in the average number of active neurons, and the variance of the number of
2336 active neurons in three different brain regions in response to visual stimuli. Since we know
2337 that correlated behaviour is associated with sensory perception (deCharms and Merzenich,
2338 1996), we might hope to measure the pairwise correlations within the neuronal population
2339 in order to further investigate these responses. But, using such short time bins can produce
2340 artificially small spike count correlation measurements (Cohen and Maunsell, 2009). Over-
2341 coming this limitation was one of our objectives for our new method. In order to do this, we
2342 abandoned the idea of measuring the correlations directly and embraced the concept of *asso-*
2343 *ciation*. In order to quantify the association between neurons, we used the Conway-Maxwell-
2344 binomial distribution to model the number of active (spiking) neurons in an ensemble as a
2345 sum of possibly associated Bernoulli random variables.

2346 We showed that the Conway-Maxwell-binomial distribution performed better than the
2347 more common options of the binomial and beta-binomial distributions. Furthermore, we
2348 showed that the positively associated behaviour between neurons in the primary visual cortex
2349 could be captured by fitting a Conway-Maxwell-binomial distribution, but was not captured
2350 by the more standard approach of measuring the spike count correlation. The associated



(A) Primary visual cortex ν parameter, bin width is 10ms.



(B) Primary visual cortex Fano factor, bin width is 10ms.

FIGURE 4.9: (A) The mean ν parameter of the COMb distribution fitted to activity in the primary visual cortex. Mean taken across all stimulated trials. A bin width of 10ms was used to classify cells as active or inactive. The change in association at stimulus onset is still captured. Some high frequency fluctuations are filtered out by using the wider bins (compare to figure 4.7a) (B) The mean Fano factor of the cells in the primary visual cortex. The change in the mean Fano factor at stimulus onset is not significant when using a bin width of 10ms.

4.5. Discussion

2351 behaviour could not be measured using spike count correlations, because of the very short
2352 bins required to capture short timescale behaviour.

2353 We replicated a famous result from Churchland et al (2010) relating to the quenching of
2354 neural variability in cortical areas at stimulus onset, and in doing so, we established a corre-
2355 spondence between the association quantifying parameter of the Conway-Maxwell-binomial
2356 (COMb) distribution and the neural variability as measured by the Fano factor. We found a
2357 reduction in the ν parameter of the COMB distribution at stimulus onset, indicating a change
2358 from no association to positive association between neurons in V1. We found a corresponding
2359 reduction in the Fano factor of the individual cells in V1. The positive association between
2360 neurons induced by the stimulus would constrain the neurons to fire at the same time. The
2361 stimulus also induced a larger number of neurons to spike. These two actions combined could
2362 cause an increase in the firing rate of individual cells that is greater in magnitude than the in-
2363 crease in firing rate variability. If this is indeed the case, then the association as captured by
2364 the COMB distribution could be regarded as one of the ‘natural parameters’ of the ensemble
2365 response for short timescales. That is, a quantity that directly measures some aspect of the
2366 behaviour of the ensemble. In this case, it the correlated behaviour of the individual neurons
2367 is captured.

2368 This work could be just a first step in creating analysis methods based on the Conway-
2369 Maxwell-binomial distribution, or similar statistical models. One way to extend the method
2370 would be to pair it up with the ‘Population Tracking model’ (O’Donnell et al., 2017). This
2371 model attempts to characterise the interaction between an ensemble and each member of the
2372 ensemble by quantifying the probability of spiking for a given a cell, given the number of
2373 active cells in the whole population. Combining this model with the COMB distribution
2374 would give us a model that could accurately fit the number of active neurons at any moment,
2375 and that gives a probability of firing for each cell, and therefore probabilities for full spiking
2376 patterns, without adding a huge number of parameters to fit.

2377 A more complex way to extend the model would be to fit a Conway-Maxwell-binomial
2378 distribution to data recorded from multiple brain regions simultaneously, with a different fit
2379 for each region, then to analyse the temporal relationship between the fitted parameters of
2380 each region. If we analysed the time series of the COMB distribution parameters from the
2381 different regions, looking at cross-correlations between regions, this may give some results
2382 relating to the timescales in which information is processed in different brain regions.

2383 **Chapter 5**

2384 **Studies with practical limitations &**
2385 **negative results**

2386 *Abstract*

2387 Here I will present some details on research topics that I started, but that unfortunately did not
2388 lead anywhere useful. There are two pieces of research, based on two papers. Each paper is
2389 related to the overall theme of my PhD of analysing and modelling behaviours of populations
2390 of neurons. The first part is based on a model of parallel spike trains including higher order
2391 interactions by Shimazaki et al (2012). The second part is based on a multiscale model for
2392 making inferences on hierarchical data.

2393 **5.1 Dynamic state space model of pairwise and higher order neu-**
2394 **ronal correlations**

2395 In their paper Shimazaki et al (2012) aimed to model spike trains from populations of neurons
2396 in parallel, with pairwise and higher order dynamic interactions between the trains. They
2397 modelled the spike trains as multi-variate binary processes using a log-linear model, and they
2398 extracted spike interaction parameters using a Bayesian filter/EM-algorithm. They developed
2399 a goodness-of-fit measure for the model to test if including these higher order correlations
2400 is necessary for an accurate model. Their measure was based on the Bayes factor but they
2401 also assessed the suitability of higher order models using the AIC and BIC. So the increase
2402 in the number of parameters associated with fitting higher order interactions was taken into
2403 account. They tested the performance of the model on synthetic data with known higher
2404 order correlations. They used the model to look for higher order correlations in data from
2405 awake behaving animals. They use the model to demonstrate dynamic appearance of higher
2406 order correlations in the monkey motor cortex (Shimazaki et al., 2012).

2407 We used the available Python repository to implement the model, and we successfully
2408 worked through the tutorial provided. But we found that the model did not scale well to
2409 larger populations. We attempted to fit the model to a population of 10 neurons and found we
2410 didn't manage to finish the process. Since, our goal was to find a model to scale to hundreds
2411 or thousands of neurons, we decided that this model was no longer worth pursuing.

2412 **5.2 A multiscale model for hierarchical data applied to**
2413 **neuronal data**

2414 In their paper Kolaczyk et al (2001) developed a framework for a modelling hierarchically
2415 aggregated data, and making inferences based on a model arising from this framework. They
2416 assumed that a hierarchical aggregation existed on the data in question, where each element at
2417 each level of the hierarchy had some associated measurements, an associated mean process,
2418 which was the expected value of these measurements. They also assumed that the measure-
2419 ments of each parent were equal to the sum of the measurements from all of its children.
2420 They showed that these assumptions gave rise to a relationship between parent and child
2421 measurements across all levels of the hierarchy, where the product of the likelihood of the
2422 parameters of the lowest level of the hierarchy can be expressed as products of conditional
2423 likelihoods of the elements of higher levels of the hierarchy (Kolaczyk and Huang, 2010).

5.2. A multiscale model for hierarchical data applied to neuronal data

2424 We hoped that the hierarchical structure of the brain (regions to subregions to cells) and a
2425 high level activity measure (fMRI or EEG) could be combined with this model to infer lower
2426 level activity from a high level measure.

2427 They gave examples of these expressions for measurements sampled from Gaussian dis-
2428 tributions, and Poisson distributions, and showed the definitions of the hierarchical param-
2429 eters which reparametrise the distribution of these data taking the hierarchy into account.
2430 They go on to suggest prior distributions for this multiscale model, and integrate these priors
2431 to give posterior distributions for the measurements from each element at each level in the hi-
2432 erarchy, and expressions for the MAP estimated parameters of each the associated processes
2433 (Kolaczyk and Huang, 2010).

2434 We implemented their model in Python by creating some synthetic data from Poisson
2435 distributions, and defining a hierarchy by agglomerating these data. We calculated the MAP
2436 estimates using our knowledge of the hierarchy, and using the expressions given in the paper.
2437 We found that the MAP estimates were far less accurate than would be achieved by simply
2438 ignoring the hierarchy during estimation, and using a maximum likelihood approach. After
2439 that, we decided to move on.

2440 **Chapter 6**

2441 **Discussion**

2442 In this project, we attempted to address some of the challenges in data collection from
2443 large neuronal ensembles (specifically with calcium imaging) and some of the problems in
2444 analysing the data collected from large neuronal ensembles.

2445 Firstly, we investigated the relationship between cell biochemistry, action potentials and
2446 the fluorescence traces produced by fluorescent calcium indicators. We did this by building
2447 a biophysical model that takes in a spike train and returns the fluorescence trace that that
2448 spike would induce. The model included mechanics for the binding of calcium to fluorescent
2449 and endogenous mobile and immobile buffers, and the consequent changes in concentration
2450 of free and bounded calcium. The model consisted of 17 parameters, 13 of which were
2451 set according to data from the literature, and 4 of which were free parameters. We trained
2452 the model using simultaneously collected spiking and calcium imaging data (Berens et al.,
2453 2018). We fitted the model by matching the $\Delta F/F_0$ in response to an action potential, and
2454 by matching the power spectrum of the actual fluorescence trace. This meant that our model
2455 would include the correct amount of noise as well as return the correct change in amplitude
2456 in response to an action potential.

2457 Since our model produced fluorescence traces, we could apply spike inference algorithms
2458 to the modelled fluorescence traces that our model produced after training, and compare the
2459 performance of the algorithms on the modelled traces to their performance on the real traces.
2460 We used three spike inference algorithms, two of which were based on modelling the cal-
2461 cium trace as an autoregression (Friedrich and Paninski, 2016; Pnevmatikakis et al., 2016),
2462 and another inference algorithm that was a little more biologically inspired, but amounted to
2463 a very similar algorithm (Deneux et al., 2016). We compared the performance of the algo-
2464 rithms by using them to infer spikes from 20 real and modelled fluorescence traces induced
2465 by 20 corresponding real spike trains. We then used several binary classification measures
2466 (true positive rate, accuracy etc.) to asses the quality of the spike inference for the real and

2467 modelled fluorescence traces. We found that the spike inference algorithms performed sim-
2468 ilarly on real and modelled traces, showing that our model is capturing at least some of the
2469 characteristics of the real fluorescence traces.

2470 In order to investigate the effect of indicator characteristics on the modelled fluorescence
2471 trace and spike inference quality, we perturbed the indicator's affinity and dissociation rate
2472 in parallel, keeping the ratio of the two the same for all perturbations. We measured the SNR
2473 of the trace, and the true positive rate of the spike inference algorithms at each perturbed
2474 value pair. We found that perturbing the values lower caused in decrease in SNR and spike
2475 inference quality. This shows that our model could be used to test theoretical fluorescent cal-
2476 cium indicators without having to actually manufacture them. Experimental neuroscientists
2477 could also use our model to judge which indicator characteristics are most influential in their
2478 experimental context.

2479 We then investigated the effect of perturbing buffer concentration, and indicator concen-
2480 tration, on the signal-to-noise ratio of the modelled fluorescence trace and spike inference
2481 quality. This was a worthwhile experiment because endogenous buffer concentrations vary
2482 from cell to cell (Bartol et al., 2015; Maravall et al., 2000; Neher and Augustine, 1992), as
2483 does indicator expression (Chen et al., 2013). We found that extreme perturbations away
2484 from the indicator concentration taken from the literature lowered the SNR of the trace, and
2485 the spike inference quality. We also found that increases in the concentration of endogenous
2486 buffer above the value taken from the literature caused a decrease in the SNR and spike infer-
2487 ence quality. This reiterates that the indicator and endogenous buffers compete to bind with
2488 free calcium molecules, and this has an effect on fluorescence and consequently on spike
2489 inference.

2490 We then created some synthetic spike trains with controlled mean firing rates sampled
2491 the rates from an Ornstein-Uhlenbeck process. We found that the higher the firing rate, the
2492 lower the accuracy of the spike inference algorithms. But the mean firing could perhaps be
2493 inferred from the amplitude of the fluorescence traces. The higher firing rate, the higher the
2494 amplitude. Calibrating the model to facilitate and accurate measurement would require some
2495 kind of ground truth, but relative comparisons could be made without any other knowledge
2496 of the underlying spiking process.

2497 One obvious limitation to our model is the lack of binding mechanics for both the indi-
2498 cator and endogenous buffers. Greenberg et al included these mechanics in their successful
2499 spike inference model. We felt that the timescale of these binding mechanics was so small in
2500 comparison to the fluorescence dynamics that omitting them would make no difference. But

2501 it is possible that their inclusion would improve our model.

2502 After investigating the difficulties with inferring spiking data from calcium imaging data,
2503 we moved from data collection to analysis and we decided to implement a new network anal-
2504 ysis method on data from a neuronal ensemble. Using an electrophysiological dataset with
2505 spike sorted data from 9 different brain regions in 3 mice (Steinmetz, Carandini, and Harris,
2506 2019), we binned the spike times for each cell into spike counts for each cell and measured
2507 the correlation coefficients between these spike counts for a selection of cells evenly dis-
2508 tributed across the 9 regions. We repeated these measurements for time bin widths ranging
2509 from 5ms to 3s. We rectified these measurements and, for a given time bin width, used them
2510 as weights for a weighted undirected graph where each node represents a neuron, and the
2511 weight of each edge is the correlation between the neurons represented by the nodes on that
2512 edge. We applied a novel spectral analysis and community detection method (Humphries
2513 et al., 2019) to this network. This clustered the nodes in our ensemble into communities
2514 whose behaviour was more correlated than expected. Our measure of 'expected correlation
2515 strength' were based on a random network that matched our data network's sparsity and total
2516 weight. We compared the detected communities to the anatomical division of our cells using
2517 clustering comparison measures. We then conditioned the binned spike counts on the be-
2518 haviour of the mouse using the principal components of a video of the mouses face recorded
2519 simultaneously with the electrophysiology. We broke the total covariance down into 'spike
2520 count covariance' and 'signal covariance' components conditioning on the behavioural data
2521 and using the law of total covariance. We then repeated our analysis for spike count corre-
2522 lations, and signal correlation. Finally, since our community detection method was only valid
2523 on graphs with non-negative weights, we used different methods for creating a non-negative
2524 graph from our total correlations, and we repeated our analysis on those graphs.

2525 Our first finding was that the time bin width used to bin spike times into spike counts had
2526 a effect on the mean magnitude of the correlations measured. The wider the bin, the higher
2527 the correlations. Not only that, we separated the pairs into positively and negative correlated
2528 pairs, and we found that positively correlated pairs have greater correlation coefficients when
2529 using a wider bin, and negatively correlated pairs have more negative correlation coefficients
2530 when using a wider bin. We also found that the width of the bin used had an effect on the
2531 distribution of the spike counts. For smaller bin widths, the distribution of spike counts was
2532 better represented by a skewed distribution like the Poisson distribution. For wider bins, the
2533 spike counts were better represented by a Gaussian distribution.

2534 Next we investigated the differences between correlations within regions and between

regions. When we divided the pairs according to those two groups, we found that the mean within-region correlations were higher at every bin width, and the difference between the two means grew with increasing bin width. When we split the pairs of cells according to their regions, we found that the mean within-region correlations in any given region were usually greater than the mean between-region correlations for any region pair involving that region. The difference between the mean within-region correlation and the highest between-region correlations involving that region grew smaller with increasing bin width. To investigate this further, we plotted these mean correlations in matrices. Although the mean within-region correlations were usually the highest value in their row or column, as the bin width increased, the mean between-region correlations grew in magnitude relative to the within-region figure.

Next we chose a null network model, and we used the ‘Network Noise Rejection’ process (Humphries et al., 2019) to check for additional structure in our correlation based data network that was not captured by the null model. We found additional structure for any bin width that we used. We also found that the dimensionality of the additional structure reduced as we increased the bin width. This could mean that the processes or representations that take place over longer timescales within the brain also take place in a lower dimensional space.

We applied a community detection method (Humphries, 2011) to the signal correlation networks arising from the network noise rejection. We found that the number of communities detected decreased with increasing bin width. We also noticed that at shorter bin widths, the detected communities were more likely to consist of cells from one brain region only. We investigated this further by using clustering comparison methods to compare the detected communities with the anatomical division of the cells. We found that for short timescales $< 50\text{ms}$ correlated communities tended to exist within anatomical regions, and for longer timescales $> 100\text{ms}$, the correlated communities tended to exist across anatomical regions. This is broadly in agreement with a similar finding for EEG data from humans performing semantic or memory tasks (Stein and Sarnthein, 2000). Von Stein et al. (2000) found that visual processing taking place locally in the visual system was captured in the gamma frequency range (25 – 70Hz), while semantic processing was captured in the beta range (12 – 18Hz), and tasks involving mental imagery and working memory retention were captured in the theta and alpha ranges (4 – 8Hz, and 8 – 12Hz respectively).

We then conditioned our correlation measures on the the mouse’s behaviour. This allowed us to create spike count correlation (or noise correlation) networks, and signal correlation networks (Cohen and Kohn, 2011). We applied our analysis to these networks. For the

2568 spike count correlation networks we found very similar results to the total correlation net-
2569 works. More communities at smaller bin widths, and communities resembled the anatomical
2570 division at smaller bin widths. Given that recent findings show that behaviour can account
2571 for correlated spiking in many areas of the brain (Stringer et al., 2019), these results for the
2572 spike count correlation show that this correlated behaviour is still processed locally at short
2573 timescales, while processes and representations that take more time make use of correlated
2574 activity across multiple regions.

2575 For the signal correlations, we still found additional structure in these networks. But we
2576 always detected a smaller number of communities. These communities also had no relation
2577 to the anatomical division of the cells. This result shows that there are groups of cells across
2578 multiple brain regions that are activated similarly by certain behaviours.

2579 All of the networks so far were based on rectified correlation measures, because the
2580 network noise rejection and community detection processing is (currently) only valid for
2581 networks with non-negative weights. For the final part of our analysis, we tried different
2582 ways of transforming our total correlations into non-negative quantities before applying our
2583 analysis. First of all we took the absolute value of our correlation measures. Our results were
2584 very similar to those for the rectified correlations with the exception that we detected more
2585 communities consistently. It is possible that using this method detects both positively and
2586 negatively correlated communities.

2587 We also tried reversing the sign of all the correlations, then rectifying the network. We
2588 hope that this would allow us to detect the negatively correlated communities. We did detect
2589 communities in these networks, but never more than three, and these communities bore no
2590 relationship with the anatomical distribution of the cells.

2591 There is a lot of potential for network science applications in computational neuroscience.
2592 For example, some pairwise measure other than correlation coefficients could be used as the
2593 weights of the graph. The synaptic connections between cells can be isolated in-vitro (Okun
2594 et al., 2015). A map of these synaptic connections could be used as the basis for directed
2595 graphs. The analysis methods applicable to directed graphs could give insights about the
2596 formation of synaptic connections, or the dynamic changes in these connections over time.
2597 Other methods of community detection could be used on directed or undirected graphs. We
2598 used a ‘hard’ clustering method in our research, that is, each neuron could be a member of
2599 one cluster/community only. ‘Fuzzy-clustering’ methods do exist, where each element of the
2600 set to be clustered could be a member of more than one cluster (Baadel, Thabtah, and Lu,
2601 2016).

Having spent much time investigating correlated behaviour using coefficients of spike counts, we decided to try another method for capturing correlated behaviour in neuronal ensembles. We used electrophysiological data taken from 5 brain regions of an awake mouse exposed to visual stimuli (Steinmetz et al., 2019). We modelled the number of active neurons in a given brain region as the number of successes in a collection of dependent Bernoulli random variables using the Conway-Maxwell-binomial distribution. To avoid violating the Bernoulli assumption, we binned the spike times using 1ms bins. The Conway-Maxwell-binomial distribution is a two parameter extension of the standard binomial distribution. The extra parameter allows the distribution to capture possible positive or negative association between the Bernoulli trials (Kadane, 2016). This means that we are assuming that all the neurons are dependent in the same way. This is not an accurate assumption, but it allows us model the data in a simple way.

First of all we established that there were changes in the number of active neurons in response to the visual stimuli. This was the case in the hippocampus, thalamus, and primary visual cortex. Each region had its own signature response. We measured the mean and variance of the number of active neurons in a sliding window starting before stimulus onset, and finishing after the end of stimulus presentation.

As well as the Conway-Maxwell-binomial distribution, we also fitted binomial, and beta-binomial distributions to the number of active neurons in a sliding window. We found that the Conway-Maxwell-binomial distribution was the best fit for over 90% of the samples. This means that the COMb distribution is capturing some dependency between the neurons, because the binomial distribution assumes independence. Also the COMb distribution captures this dependence more accurately than the beta-binomial distribution, which does have some capacity for over dispersion.

Next we showed that the Conway-Maxwell-binomial distribution captured the change in association at stimulus onset better than the correlation coefficient. The extremely small bin width artificially shrunk the correlation coefficient to the point where this measurement didn't detect any correlated activity. But the association parameter of the COMb distribution detected some positive association between the neurons at stimulus onset. So, for particularly short time bins, where neurons can be treated as Bernoulli random variables, the Conway-Maxwell-binomial distribution is a good way to capture correlated behaviour. There are other measurements for capturing association to which this distribution should be compared. Cross-correlograms could be used for some measure of synchrony, for example.

2635 Finally, we replicated a famous finding of Churchland et al. (2010) relating to the quenching
2636 of neural variability at stimulus onset, thereby finding a parallel between this reduction
2637 in the Fano factor and a reduction in the association parameter of the COMb distribution.

2638 We showed that computational neuroscientists can make progress by being inventive with
2639 their statistical models. A similar distribution to investigate would be the Conway-Maxwell-
2640 Poisson distribution. This is similar to the standard Poisson distribution, but with an addi-
2641 tional parameter that allows for over- or under- dispersion relative to a Poisson distribution.
2642 This might be ideal for modelling firing rates of individual neurons. Some interaction be-
2643 tween the fitted parameters could capture the association between neurons.

2644 There is one technology that has the potential to take over from both electrophysiology
2645 and calcium imaging. The technique of voltage imaging has become more useful in recent
2646 years. The aim for neuroscience would be to develop a voltage imaging dye or protein that
2647 images the membrane potential of a neuron with enough spatial and temporal resolution to de-
2648 tect action potentials. The voltage imaging dyes that have been developed so far do not have
2649 high enough spatial resolution to single out individual cells in-vivo using staining (Bando
2650 et al., 2019). But, genetically encoded voltage indicators have been developed that have high
2651 enough resolution to indicate individual spikes and subthreshold activity from small numbers
2652 of cells in the striatum, hippocampus, and cortex of awake behaving mice (Piatkevich et al.,
2653 2019). These indicators have the potential to take over from calcium imaging, and if imaging
2654 deep within the brain becomes possible, electrophysiology could also be replaced. This is
2655 speculation, but the potential is there.

2656 Bibliography

- 2657 Allen, William E. et al. (2019). “Thirst regulates motivated behavior through modulation of
2658 brainwide neural population dynamics”. In: *Science* 364.6437.
- 2659 Baadel, S., F. Thabtah, and J. Lu (2016). “Overlapping clustering: A review”. In: *2016 SAI
2660 Computing Conference (SAI)*, pp. 233–237.
- 2661 Baldassano, Christopher et al. (2017). “Discovering Event Structure in Continuous Narrative
2662 Perception and Memory”. In: *Neuron* 95.3, 709 –721.e5.
- 2663 Bando, Yuki et al. (2019). “Genetic voltage indicators”. In: *BMC Biology* 17.1, p. 71.
- 2664 Bartol, Thomas M. et al. (2015). “Computational reconstitution of spine calcium transients
2665 from individual proteins”. In: *Frontiers in Synaptic Neuroscience* 7, p. 17.
- 2666 Berens, Philipp et al. (May 2018). “Community-based benchmarking improves spike rate in-
2667 ference from two-photon calcium imaging data”. In: *PLOS Computational Biology* 14.5,
2668 pp. 1–13.
- 2669 Bezanson, Jeff et al. (Sept. 2012). “Julia: A Fast Dynamic Language for Technical Comput-
2670 ing”. In: *MIT*.
- 2671 Brini, Marisa et al. (2014). “Neuronal calcium signaling: function and dysfunction”. In: *Cel-
2672 lular and Molecular Life Sciences* 71.15, pp. 2787–2814.
- 2673 Buccino, Alessio P. et al. (2019). “SpikeInterface, a unified framework for spike sorting”. In:
2674 *bioRxiv*.
- 2675 Chen, Tsai-Wen et al. (July 2013). “Ultrasensitive fluorescent proteins for imaging neuronal
2676 activity”. In: *Nature* 499, 295–300.
- 2677 Churchland, Mark M. et al. (2010). “Stimulus onset quenches neural variability: a widespread
2678 cortical phenomenon”. eng. In: *Nature neuroscience* 13.3. 20173745[pmid], pp. 369–378.
- 2679 Cohen, Marlene R. and Adam Kohn (2011). “Measuring and interpreting neuronal corre-
2680 lations”. In: *Nature Neuroscience* 14.7, pp. 811–819.
- 2681 Cohen, Marlene R. and John H. R. Maunsell (2009). “Attention improves performance pri-
2682 marily by reducing interneuronal correlations”. eng. In: *Nature neuroscience* 12.12. 19915566[pmid],
2683 pp. 1594–1600.

- 2684 Dana, Hod et al. (Sept. 2014). “Thy1-GCaMP6 Transgenic Mice for Neuronal Population
2685 Imaging In Vivo”. In: *PloS one* 9, e108697.
- 2686 deCharms, R. Christopher and Michael M. Merzenich (1996). “Primary cortical represen-
2687 tation of sounds by the coordination of action-potential timing”. In: *Nature* 381.6583,
2688 pp. 610–613.
- 2689 Deneux, Thomas et al. (July 2016). “Accurate spike estimation from noisy calcium signals
2690 for ultrafast three-dimensional imaging of large neuronal populations in vivo”. In: *Nature*
2691 *Communications* 7.1.
- 2692 Dombeck, Daniel A. et al. (2010). “Functional imaging of hippocampal place cells at cellular
2693 resolution during virtual navigation”. In: *Nature Neuroscience* 13.11, pp. 1433–1440.
- 2694 Éltes, Tímea et al. (2019). “Improved spike inference accuracy by estimating the peak am-
2695 plitude of unitary [Ca₂₊] transients in weakly GCaMP6f-expressing hippocampal pyra-
2696 midal cells”. In: *The Journal of Physiology* 597.11, pp. 2925–2947.
- 2697 Faas, Guido C. et al. (2011). “Calmodulin as a direct detector of Ca₂₊ signals”. In: *Nature*
2698 *Neuroscience* 14.3, pp. 301–304.
- 2699 Fiala, John C. and Kristen M. Harris (1999). *Dendrite Structure*.
- 2700 Flach, Boris (Sept. 2013). “A Class of Random Fields on Complete Graphs with Tractable
2701 Partition Function”. In: *IEEE transactions on pattern analysis and machine intelligence*
2702 35, pp. 2304–6.
- 2703 Forney, G. D. (1973). “The viterbi algorithm”. In: *Proceedings of the IEEE* 61.3, pp. 268–
2704 278.
- 2705 Fosdick, Bailey et al. (Aug. 2016). “Configuring Random Graph Models with Fixed Degree
2706 Sequences”. In: *SIAM Review* 60.
- 2707 Friedrich, Johannes and Liam Paninski (2016). “Fast Active Set Methods for Online Spike In-
2708 ference from Calcium Imaging”. In: *Advances in Neural Information Processing Systems*
2709 29. Ed. by D. D. Lee et al. Curran Associates, Inc., pp. 1984–1992.
- 2710 Ganmor, Elad, Ronen Segev, and Elad Schneidman (2011). “Sparse low-order interaction
2711 network underlies a highly correlated and learnable neural population code”. In: *Pro-
2712 ceedings of the National Academy of Sciences* 108.23, pp. 9679–9684.
- 2713 Girard, P., J. M. Hupé, and J. Bullier (2001). “Feedforward and Feedback Connections Be-
2714 tween Areas V1 and V2 of the Monkey Have Similar Rapid Conduction Velocities”. In:
2715 *Journal of Neurophysiology* 85.3. PMID: 11248002, pp. 1328–1331.
- 2716 Greenberg, David et al. (Nov. 2018). “Accurate action potential inference from a calcium
2717 sensor protein through biophysical modeling:” in:

Bibliography

- 2718 Gründemann, Jan et al. (2019). “Amygdala ensembles encode behavioral states”. In: *Science*
2719 364.6437.
- 2720 Hodgkin, A. L. and A. F. Huxley (1939). “Action Potentials Recorded from Inside a Nerve
2721 Fibre”. In: *Nature* 144.3651, pp. 710–711.
- 2722 Humphries, Mark et al. (Jan. 2019). “Spectral rejection for testing hypotheses of structure in
2723 networks”. In:
- 2724 Humphries, Mark D. (2011). “Spike-Train Communities: Finding Groups of Similar Spike
2725 Trains”. In: *Journal of Neuroscience* 31.6, pp. 2321–2336.
- 2726 Jun, James J. et al. (2017). “Fully integrated silicon probes for high-density recording of
2727 neural activity”. In: *Nature* 551.7679, pp. 232–236.
- 2728 Kadane, Joseph B. (June 2016). “Sums of Possibly Associated Bernoulli Variables: The
2729 Conway–Maxwell-Binomial Distribution”. In: *Bayesian Anal.* 11.2, pp. 403–420.
- 2730 Kilhoffer, Marie-Claude et al. (Sept. 1992). “Use of Engineered Proteins With Internal Tryp-
2731 tophean Reporter Groups and Perturbation Techniques to Probe the Mechanism of Ligand-
2732 Protein Interactions: Investigation of the Mechanism of Calcium Binding to Calmodulin”.
2733 In: *Biochemistry* 31.34, pp. 8098–8106.
- 2734 Koch, Christoff (1999). *Biophysics of Computation: Information Processing in Single Neu-*
2735 *rons*. Oxford University Press.
- 2736 Kolaczyk, Eric and Haiying Huang (Sept. 2010). “Multiscale Statistical Models for Hierar-
2737 chical Spatial Aggregation”. In: *Geographical Analysis* 33, pp. 95 –118.
- 2738 Lee, Suk-HO et al. (July 2000). “Differences in Ca²⁺ buffering properties between excitatory
2739 and inhibitory hippocampal neurons from the rat”. In: *The Journal of Physiology* 525.
- 2740 Litwin-Kumar, Ashok, Maurice Chacron, and Brent Doiron (Sept. 2012). “The Spatial Struc-
2741 ture of Stimuli Shapes the Timescale of Correlations in Population Spiking Activity”. In:
2742 *PLoS computational biology* 8, e1002667.
- 2743 Maravall, M et al. (May 2000). “Estimating intracellular calcium concentrations and buffer-
2744 ing without wavelength ratioing”. In: *Biophysical Journal* 78.5, pp. 2655–2667.
- 2745 Maugis, Pa (Jan. 2014). “Event Conditional Correlation: Or How Non-Linear Linear Depen-
2746 dence Can Be”. In:
- 2747 Meilă, Marina (2007). “Comparing clusterings—an information based distance”. In: *Journal*
2748 *of Multivariate Analysis* 98.5, pp. 873 –895.
- 2749 Murray, John D. et al. (2014). “A hierarchy of intrinsic timescales across primate cortex”. In:
2750 *Nature Neuroscience* 17.12, pp. 1661–1663.

- 2751 Neher, E. and G. J. Augustine (1992). “Calcium gradients and buffers in bovine chromaffin
2752 cells”. eng. In: *The Journal of physiology* 450. 1331424[pmid], pp. 273–301.
- 2753 O’Donnell, Cian et al. (Jan. 2017). “The population tracking model: a simple, scalable statis-
2754 tical model for neural population data”. English. In: *Neural Computation* 29.1, pp. 50–
2755 93.
- 2756 Okun, Michael et al. (2015). “Diverse coupling of neurons to populations in sensory cortex”.
2757 In: *Nature* 521.7553, pp. 511–515.
- 2758 Ouzounov, Dimitre G. et al. (2017). “In vivo three-photon imaging of activity of GCaMP6-
2759 labeled neurons deep in intact mouse brain”. eng. In: *Nature methods* 14.4. 28218900[pmid],
2760 pp. 388–390.
- 2761 Patterson, Carlyn A. et al. (2014). “Similar adaptation effects in primary visual cortex and
2762 area MT of the macaque monkey under matched stimulus conditions”. In: *Journal of
2763 Neurophysiology* 111.6. PMID: 24371295, pp. 1203–1213.
- 2764 Peron, Simon P. et al. (2015). “A Cellular Resolution Map of Barrel Cortex Activity during
2765 Tactile Behavior”. In: *Neuron* 86.3, pp. 783–799.
- 2766 Piatkevich, Kiryl D. et al. (2019). “Population imaging of neural activity in awake behaving
2767 mice”. In: *Nature* 574.7778, pp. 413–417.
- 2768 Pnevmatikakis, E.A. et al. (Jan. 2016). “Simultaneous Denoising, Deconvolution, and Demix-
2769 ing of Calcium Imaging Data”. In: *Neuron* 89.2, pp. 285–299.
- 2770 Pnevmatikakis, Eftychios et al. (Nov. 2013). “Bayesian spike inference from calcium imaging
2771 data”. In: *Conference Record - Asilomar Conference on Signals, Systems and Computers*.
- 2772 Pnevmatikakis, Eftychios et al. (Sept. 2014). “A structured matrix factorization framework
2773 for large scale calcium imaging data analysis”. In:
- 2774 Schneidman, Elad et al. (2006). “Weak pairwise correlations imply strongly correlated net-
2775 work states in a neural population”. eng. In: *Nature* 440.7087. 16625187[pmid], pp. 1007–
2776 1012.
- 2777 Shannon, C. E. (1948). “A Mathematical Theory of Communication”. In: *Bell System Tech-
2778 nical Journal* 27.3, pp. 379–423.
- 2779 Shimazaki, Hideaki et al. (2012). “State-space analysis of time-varying higher-order spike
2780 correlation for multiple neural spike train data”. eng. In: *PLoS computational biology*
2781 8.3. 22412358[pmid], e1002385–e1002385.
- 2782 Staude, Benjamin, Sonja Grün, and Stefan Rotter (2010). “Higher-Order Correlations and
2783 Cumulants”. In: *Analysis of Parallel Spike Trains*. Ed. by Sonja Grün and Stefan Rotter.
2784 Boston, MA: Springer US, pp. 253–280.

Bibliography

- 2785 Stein, Astrid von and Johannes Sarnthein (2000). “Different frequencies for different scales
2786 of cortical integration: from local gamma to long range alpha/theta synchronization”. In:
2787 *International Journal of Psychophysiology* 38.3, pp. 301 –313.
- 2788 Steinmetz, Nick, Matteo Carandini, and Kenneth D. Harris (2019). ”*Single Phase3*” and
2789 ”*Dual Phase3*” *Neuropixels Datasets*.
- 2790 Steinmetz, Nick et al. (Mar. 2019). “Eight-probe Neuropixels recordings during spontaneous
2791 behaviors”. In:
- 2792 Stevenson, Ian H. and Konrad P. Kording (2011). “How advances in neural recording affect
2793 data analysis”. In: *Nature Neuroscience* 14.2, pp. 139–142.
- 2794 Stringer, Carsen et al. (2019). “Spontaneous behaviors drive multidimensional, brainwide
2795 activity”. In: *Science* 364.6437.
- 2796 Tada, Mayumi et al. (2014). “A highly sensitive fluorescent indicator dye for calcium imaging
2797 of neural activity in vitro and in vivo”. In: *European Journal of Neuroscience* 39.11,
2798 pp. 1720–1728.
- 2799 Tian, Lin et al. (2009). “Imaging neural activity in worms, flies and mice with improved
2800 GCaMP calcium indicators”. eng. In: *Nature methods* 6.12. 19898485[pmid], pp. 875–
2801 881.
- 2802 Tkačik, Gašper et al. (2014). “Searching for collective behavior in a large network of sen-
2803 sory neurons”. eng. In: *PLoS computational biology* 10.1. 24391485[pmid], e1003408–
2804 e1003408.
- 2805 Treves, Alessandro and Stefano Panzeri (1995). “The Upward Bias in Measures of Informa-
2806 tion Derived from Limited Data Samples”. In: *Neural Computation* 7.2, pp. 399–407.
- 2807 Vinh, Nguyen Xuan, Julien Epps, and James Bailey (Dec. 2010). “Information Theoretic
2808 Measures for Clusterings Comparison: Variants, Properties, Normalization and Correc-
2809 tion for Chance”. In: *J. Mach. Learn. Res.* 11, 2837–2854.
- 2810 Vogelstein, Joshua T. et al. (Oct. 2010). “Fast nonnegative deconvolution for spike train infer-
2811 ence from population calcium imaging”. In: *Journal of neurophysiology* 104.6, 295–300.
- 2812 Wierzyński, ”Casimir M. et al. (2009). ””State-Dependent Spike-Timing Relationships be-
2813 tween Hippocampal and Prefrontal Circuits during Sleep””. In: ”*Neuron*” ”61”. ”4”, ”587
2814 –596”.
- 2815 Zariwala, Hatim A. et al. (2012). “A Cre-dependent GCaMP3 reporter mouse for neuronal
2816 imaging in vivo”. eng. In: *The Journal of neuroscience : the official journal of the Society
2817 for Neuroscience* 32.9. 22378886[pmid], pp. 3131–3141.

- 2818 Zou, Hui and Trevor Hastie (2005). “Regularization and variable selection via the Elastic
2819 Net”. In: *Journal of the Royal Statistical Society, Series B* 67, pp. 301–320.